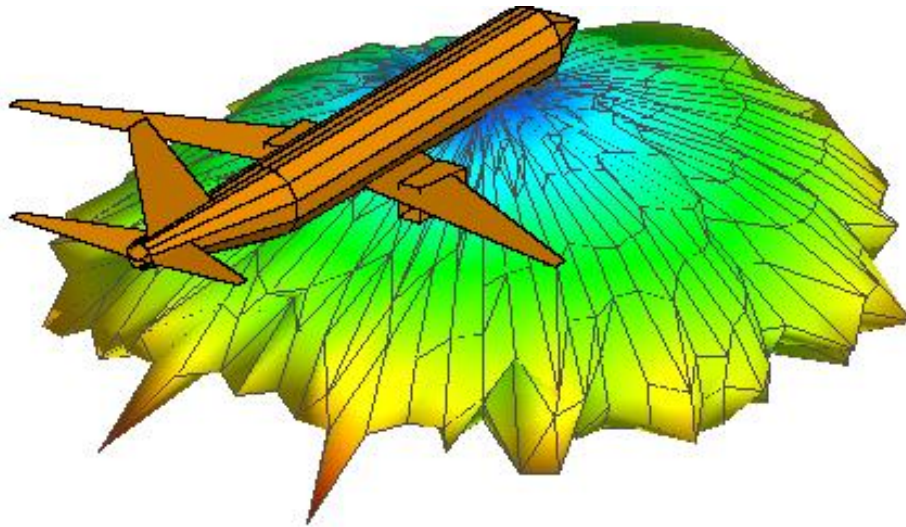


Optimization of the Antenna Placement on a Commercial Aircraft for Communication with Ground and Satellites

to obtain the degree of Master of Science
at the Delft University of Technology,
to be defended publicly on Monday May 6, 2019 at 12.30



Name: Elmira Kireeva
Student number: 4153324
Project duration: November 1, 2018 – May 6, 2019

Thesis committee: Prof. Dr. A. Yarovoy, TU Delft, supervisor
Dr. Oleg . A. Krasnov, TU Delft
Dr. P. Lopez Dekker, TU Delft
Dr. E. Rammos, SkyfloX

An electronic version of this thesis is available at <http://repository.tudelft.nl/>.

Abstract

Traditionally, a geographical area can be monitored via land based communication systems or spaceborne remote systems for disaster prevention. However both methods have their respective limitations in terms of resolution, accuracy and real time observation. A new suborbital constellation concept offers an independent unit device which will be attached to an aircraft and use commercial flights as means of monitoring forest fires or forecasting solar energy. The shape of the fuselage can be used to redirect the creeping wave generated from the antenna away from the aircraft's surface, towards the satellites for communication purposes. This research aims to determine an optimum antenna placement on the electrically large body in order to satisfy efficient communication with ground and satellites from the same location on the aircraft.

The quarter wavelength monopole operating at 1.575 GHz in L1 band for the GPS communication and a patch antenna with dielectric constant of 2.2 for the substrate operating at 800 MHz for the GSM communication are selected. Various algorithms and approaches are investigated to perform comparison of accuracy for results and computational resources between different simulation techniques namely Multi-Level Fast Multipole Method (MLFMM), Physical Optics (PO) and Uniform Theory of Diffraction (UTD) using a modern computational electromagnetic numerical platform FEKO. The simulation results show that the optimum antenna location on a Boeing 737 is found to be at the bottom of the aircraft in the conical section of the tail 30.95 m away from the tip of the nose in the longitudinal direction. In addition to that, this work provides a unique perspective to system engineering for using aircraft as a land monitoring station.

Table of Content

1. Introduction.....	1
1.1 Motivation.....	1
1.2 Novelty Contribution.....	2
1.3 State of the Art.....	2
1.4 Solution Approach.....	5
1.5 Thesis Outline.....	6
2. System Analysis.....	7
2.1 System Specifications.....	7
2.2 Coverage	10
2.3 Link Budget Analysis.....	16
2.4 Antenna Selection.....	18
2.5 Conclusion.....	25
3. Overview of CEM Simulation Methods.....	26
3.1 Method of Moments.....	26
3.2 MLFMM.....	28
3.3 Physical Optics.....	30
3.4 Uniform Theory of Diffraction.....	31
3.5 Conclusion.....	33
4. Feasibility Analysis.....	35
4.1 Square Plate.....	35
4.2 Cylinder.....	42
4.3 UTD Settings.....	49
4.4 Conclusion.....	51
5. Aircraft Geometry Approximation.....	53
5.1 Aircraft Selection.....	53
5.2 Aircraft Model Approximations.....	55
5.3 Conclusion.....	61
6. Results.....	63
6.1 Selection of the Antenna System Location.....	63
6.2 Radiation Patterns of the antenna for GPS Communication.....	64
6.3 Radiation Patterns of the antenna for GSM Communication.....	75
6.4 Verification.....	85
6.5 Conclusion.....	91
7. Conclusions.....	92
8. Recommendations.....	94
References.....	95

Chapter 1 Introduction

1.1 Motivation

Global warming is causing some irreversible changes to the planet every day. At every location some changes are constantly taking place. Human societies have fought with disasters and calamities for centuries and the present solution is to closely monitor state of the art and act upon the event in real life application.

One of the examples is devastating result of forest fire break-outs. Annually there are about 60,000 forest fires taking place creating huge devastation including human and property losses [1]. This accounts for burning of 340 million hectares of Earth's vegetated surface annually [2]. Another example includes damage that is inflicted due to flooding on the crops. 'Flooding depletes soils from oxygen and increases diseases infections and nitrogen losses' [3].

Traditionally, a geographical area can be monitored via land based communication systems or spaceborne remote systems. The land based observation systems include world meteorological weather radars, telecommunication network for cooperative detection systems specifically for forest fires are included but not limited to it. Alternatively, Low Earth orbit satellites and Geosynchronous Equatorial Orbit (GEO) satellites provide an opportunity for relatively medium temporal resolution ('i.e. two daily passes over a given area for each operating satellite, thus providing only two sets of data obtained per day' [4]). Both methods provide advantages and disadvantages in terms of budget, efficiency, performance, resolution, accuracy and real time observation. There is however an alternative method which uniquely solves the problem of real time monitoring and analysing the current state of affairs.

Considering the above mentioned monitoring methods along with their costs, limited coverage areas, fixed monitoring times per day and resulting longer reaction time; a new monitoring method using daily commercial flights is introduced by SkyfloX B.V. [5]. There are about 160,000 number of flights occurring daily worldwide covering large distances as well as remote places [6]. By attaching a monitoring device to an aircraft it would provide an opportunity of almost continuous monitoring and coverage of these regions. The average cruising altitude of 11,000 meters allows high resolution imaging. Mounting, maintenance, modifications or reparations can be easily implemented when the aircraft is on the ground.

Problem Statement

While individual antenna placements on the aircraft have been thoroughly studied, this project aims to optimize the position of a multiband antenna system such that it will provide a wireless link to communicate to multiple users at different locations (ground and space) from the same placement located on the aircraft. The fuselage could be used to re-direct the creeping wave generated by the antenna away from the Earth's surface, towards the satellites for navigational and communication purposes. The multiband antenna system, to be used in the attached units of the SkyfloX project should support Global System for Mobile communication (GSM) and Global Positioning System (GPS) link. This multiband antenna system should provide sufficient coverage (in order to realize Line of Sight link to GSM base stations and GPS satellites). Furthermore, it should possess antenna gain sufficient to realize wireless link budget within two types of links described above. The antenna gain

is estimated by simulating a radiation pattern. An appropriate simulation method is reviewed and selected among the possible options. The approximation of the aircraft model depends on the selected simulated method.

1.2 Novelty Contribution

An aircraft is a complex structure which acts as a scattering body that reflects electromagnetic waves emitted by antennas. The aircraft includes numerous antennas for many functionalities in the flight and on land. Figure 1.1 shows all the antennas placements on Boeing 787.

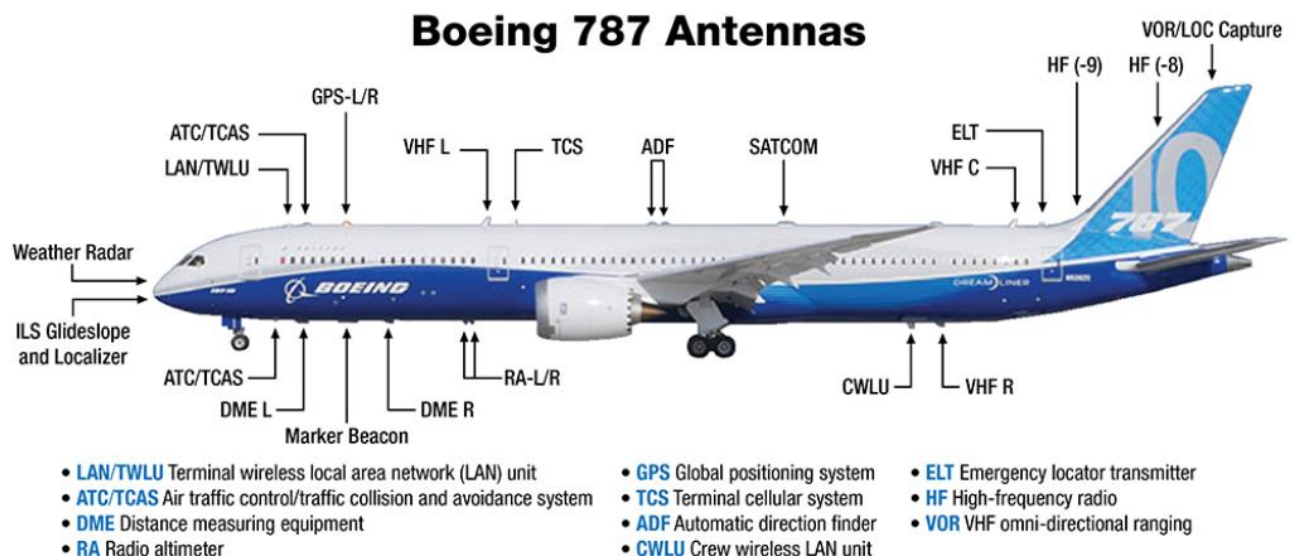


Figure 1.1 Antenna placements on the aircraft Boeing 787 [7]

In the current state-of-the art, every individual antenna placed on the aircraft operates at a single frequency [7, 8, 9, 10, 11, 12] while taking into account introduced interferences caused by multiple antennas in the close proximity range between each other. This research contrasts the state of the art by introducing an optimization problem of antenna placement such that it will operate at two different frequencies from the same location while using the fuselage of the aircraft to re-radiate the EM waves due to creeping effect.

1.3 State of the Art (Literature Review)

In order to determine the optimum position of the antenna on an aircraft, the radiation pattern of the antenna needs to be estimated. This can be done using several computational methods. This chapter introduces 4 main approaches and shows corresponding applicable computational electromagnetic tools for calculating electromagnetic fields.

Overview of Computational Methods

Computational Electromagnetics (CEM) models interaction of electromagnetic field with environment and physical objects. It typically involves solution and approximation of Maxwell's equations and is used to calculate radiation pattern, antenna performance, radar cross sections and other parameters.

All computational electromagnetic approaches and methods compromise between accuracy of approximations and computational costs. Approximations may be refined in order to increase accuracy which in turn approach results of an analytical solution. Computational costs are resources which are usually described by Central Processing Unit (CPU) time and memory.

Before determining the design of the antenna and measuring the particulars of the aircraft dimensions, it is important to have an overview of the overall approaches that are available in order to solve electrically large objects. The following section will describe 4 main approaches that are widely used in current state of the art.

The four approaches include:

- 1. Integral Equations
- 2. Volume Meshing Method
- 3. Differential Equations
- 4. Optical/Asymptotic Method

These four approaches further sub classify and include a large number of advanced computational tools and methods to perform electromagnetic analysis for a range of different problems. These problems include a study of Very High Frequency (VHF) antenna placement on a naval platform, computational modelling of a car with integrated windscreen antenna, human body interaction with mobile communication devices and many more [13]. Figure 1.2 shows suggested simulation approaches which is defined by the object's electrical size and complexity of the material.

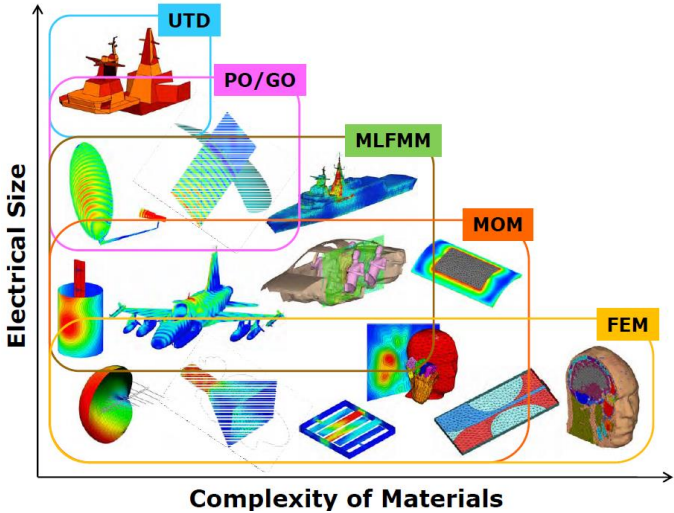


Figure 1.2 Electromagnetic simulation Map. CEM Methods presented in FEKO [13]

Figure 1.3 summarizes the general computational electromagnetic tools which show all the possible methods that are available in order to calculate a radiation pattern.

Computational Electromagnetics

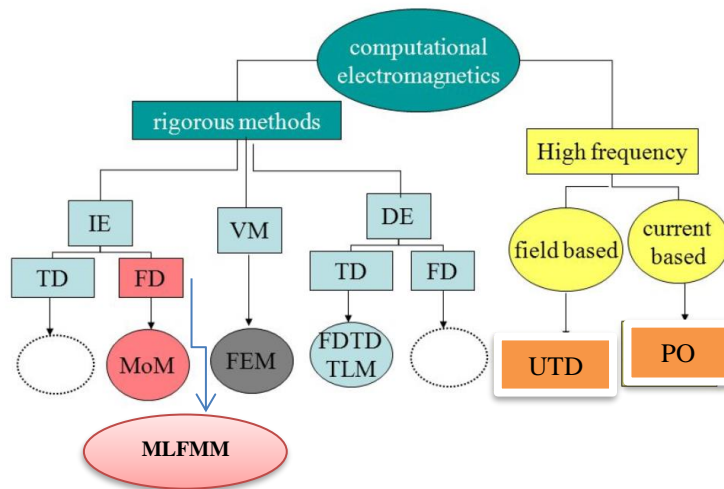


Figure 1.3 Summary of 4 approaches and related computational tools for Electromagnetic Analysis [14]

Brief description of the major computational EM Methods

The first method is the Method of Moments (MoM) which corresponds to the Integral Equations Approach. This method is considered to be applicable if number of unknowns does not exceed more than a couple of thousand triangles of the meshed electrical body. This is demonstrated in paper [15]. The aircraft is meshed using $\lambda/8$. The advantage of this method is an accurate radiation pattern however for an electrically large body, using conventional resources (e.g. PC with 2 cores), the CPU and memory often crash and the solution becomes unachievable.

The second method is Multi-Level Fast Multipole Method (MLFMM). The MLFMM differs from the MoM in that it groups basis functions together in a cluster and computes the interaction between groups of basis functions, rather than between individual basis functions. Radiation pattern of an electrically large object such as the aircraft is presented in papers [10, 11, 15, 16]. The literature suggests that MLFMM is one of the most widely used methods to estimate the radiation patterns because it gives the optimum performance at the trade-off between computational resources and the accuracy of the results while the accuracy is comparable to simulation results of MoM.

The Finite Element methods (FEM), Finite Difference Time Domain (FDTD) and Transmission Line methods are methods which are not suitable for estimation of radiation pattern for electrically large objects.

Asymptotic Method presents a drastically different approach [15, 16, 17, 18] than the rigorous approaches mentioned earlier. In field based solution where Uniform Theory of Diffraction (UTD) is an example of one of the solution methods, electromagnetic waves are treated as rays and are subjects to Snell's laws of reflection. The rays reflect from the plane surface and diffract at the edges; the creeping waves are generated around curved surfaces. In both cases the rays are assumed to be plane waves and thus the nearest interaction point from the source has to be in the far field of the antenna [12]. However UTD method, as any other method has its limitations. In this regards, the obstacle

model has to be several wavelengths away (about 10 to 12 wavelengths for aperture antennas). Also low frequencies cannot be used and small structural details cannot be modelled. The advantage of UTD method is that increasing the frequency does not have an impact on the CPU time.

Asymptotic method also includes high frequency current based solution for which Physical Optics (PO) is the main numerical solution method. The PO method assumes that the currents induced on a metallic structure by an incoming field are the same as those induced on an infinite plane locally tangential to the surface [10, 11]. Over the shadowed portion of the body the surface field is zero. These physical optics approximations are applied in the frequency domain with the inverse Fourier Transform. The accuracy of PO is significantly lower compared to MoM, however the results are simulated at considerably lower CPU time and memory.

Table 1.1 shows the comparison between different electromagnetic computational methods in terms of CPU time, memory and accuracy.

Table 1.1 The comparison of the radiation pattern for an aircraft between applicable simulated CEM methods and measured results

	CPU Time	Memory	Accuracy	Applicability to Electrically Large Body
Multi-Level Fast Multipole Method (MLFMM)	√	√	√√√	√√
Physical Optics (PO)	√√	√√	√√	√√√
Uniform Theory of Diffraction (UTD)	√√√	√√√	√√	√√√

√√√ - excellent performance, √√ - mediocre performance, √ - poor performance

From the above analysis it can be stated that the MoM method is not a feasible approach as it requires unacceptable amount of computational resources in terms of Memory and CPU time and can only be applied to smaller scale scattering objects. Secondly, MLFMM method outperforms MoM with improved computational performance in terms of required memory and CPU time. It is applicable for larger structures however it still requires long computational time.

Physical Optics is applicable to electrically large objects however the results are not accurate enough. Finally, the UTD method shows good performance in terms of accuracy for the radiation pattern and delivers results with the least CPU time.

1.4 Solution Approach

The purpose of this research is to investigate the optimum position for antenna system on a commercial aircraft such that it can provide a wireless communication link to multiple users at different frequencies. In order to do that the problem of the Thesis will be approached in the following manner.

1. Analyse wireless communication links for GPS and GSM systems
2. Derive requirements for the antenna system
3. Perform a Feasibility Analysis by comparing radiation patterns using MLFMM, PO and UTD methods
4. Use the selected method to optimize the position of a multiband antenna system by simulating the radiation patterns for each communication link and finding the antenna system position, which provides the best wireless links to visible base stations and satellites for both GSM and GPS respectively
5. Verify the selected set of radiation patterns at the optimal position with a full wave simulation method

1.5 Thesis Outline

The Thesis paper is organized in the following manner. Chapter 1 introduces problem statement. Chapter 2 describes the elements of the system and presents derivation of the key requirements by analysing the coverage and link budget analysis. Chapter 3 gives a detailed overview of the CEM methods. Chapter 4 presents a feasibility study where radiation patterns are simulated and compared for simple objects such as a square plate and a cylinder using MLFMM, PO and UTD methods. Chapter 5 describes the aircraft geometry approximations. Chapter 6 describes the position optimization for a multiband antenna system on the approximated model of the aircraft. It also presents the independent verification of the simulation results by using full-wave simulation technique. Chapters 7 and 8 present conclusions and recommendations respectively.

Chapter 2 Systems Analysis

The following chapter describes the elements of the system and presents derivation of the key requirements by analysing the coverage and link budget analysis as well as determining the performance of the selected antennas.

2.1 System Specifications

In this chapter wireless communication links for the SkyfloX system are considered. First of all it is important to analyse the elements of the system and find the corresponding ways that those elements interact with each other.

Figure 2.1 shows the schematic view of the overall system with following elements:

- 1) GPS Satellites
- 2) Iridium Satellites
- 3) Aircraft
- 4) Ground Base Station
- 5) Multiband Antenna System

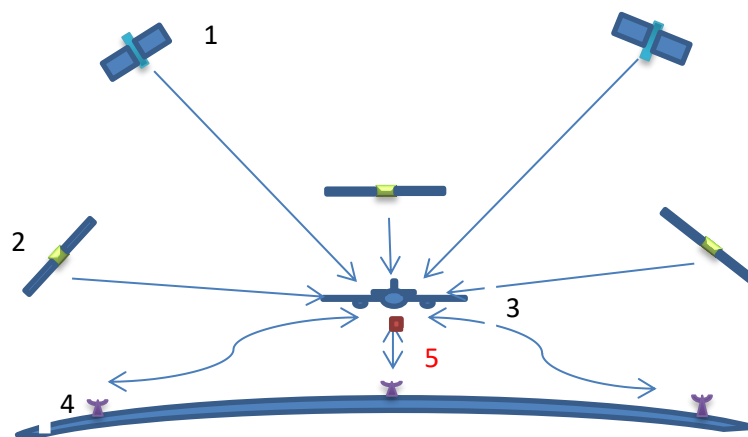


Figure 2.1 Schematic View of the Overall System

The numbers indicate the elements of the system, while the arrows show their perspective interaction which is performed through transmission of wireless electromagnetic waves. Single sided arrows indicate that communication is only working one sided, namely looking at antennas, indicated as the red box located at the bottom of the aircraft, the incoming waves from the satellites are seen as receiving downlink for the GPS communication. Double sided arrow indicates that communication happens both ways and that the antenna is acting as a transceiver. Note that both antennas for GPS and GSM are located at the same position as was stated in the Research Question in Chapter 1.

While the system includes two satellite elements: Iridium satellites and GPS satellites, in the scope of this research paper, only GPS satellite will be considered for further investigation.

Global Navigation Satellite Systems

Global Navigation Satellite System (GNSS) provides satellite navigation system with global coverage. Currently there are three main providers with GNSS systems, namely GPS, GLONASS and Galileo. Global coverage is achieved by a satellite constellation of 31 satellites spread between several orbital planes with varying inclinations at orbital height of approximately 20 200km [19, 20]. Schematic view of GNSS satellite orbits is shown in Figure 1.2.

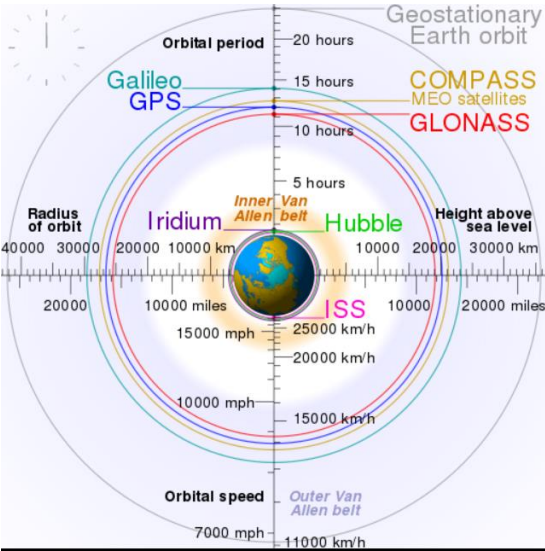


Figure 2.2 Schematic view of the GNSS Satellite positions with respect to Earth’s Orbit [21]

Table 2.1 summarizes parameters for the following GNSS systems: GPS, GLONASS and Galileo. Bold indicates authorization for civilian applications [21, 22].

Table 2.1 Performance Parameters for various GNSS systems

	Central frequency [MHz]		Bandwidth [MHz]	Polarization
GPS	L1	1 575	15	RHCP [5]
	L2	1 227.6	12	
	L5	1 176.45	12.5	
GLONASS	L1	1 609	7	RHCP
	L2	1 246	7.5	
Galileo	L6	1 542.5	17.5	RHCP
	L2	1 278.75	12	

For the further analysis L1 band with central frequency of 1.575 GHz for GPS communication is chosen.

Global System for Mobile Communication

Global System for Mobile communications (GSM) is a standard developed by the European Telecommunications Standards Institute to describe the protocols for digital cellular networks used by mobile devices [23]. A cellular network is a communication network distributed over land areas called cells, each served by at least one fixed-location transceiver, but more normally three cell sites or base transceiver stations. These base stations provide the cell with the network coverage which can be used for transmission of voice, data, and other types of content [23]. Figure 2.2 shows a typical cellular network with a Base Transceiver Station (BTS) in the center of each cell.

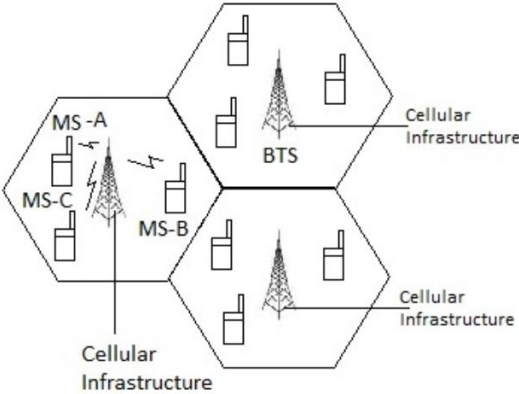


Figure 2.3 Cellular Network with a Base Transceiver Station (BTS) in the center of each cell and mobile devices[24]

There are numerous frequency bands available for GSM communication however most of them are not in operational use. Table 2.2 summarizes bands and respective bandwidths that are currently used in the global network and in Region 1 (corresponding to European mobile communication space). There are two modulating techniques: Time Division Duplexing (TDD) and Frequency Division Duplexing (FDD) and in the global roaming mostly FDD modulating technique is used [25].

Table 2.2 Most widely used Band frequencies for LTE; Bold indicates global roaming

	Multiplexing Mode	Frequency Bands [MHz]	Channel [MHz]	Bandwidth
B1	FDD	2100	5, 10, 15, 20	
B3	FDD	1800	1.4, 3, 5, 10, 15, 20	
B7	FDD	2600	5, 10, 15, 20	
B8	FDD	900	1.4, 3, 5, 10	
B20	FDD	800	5, 10, 15, 20	

For the further analysis central frequency of 800MHz for GSM communication is chosen. The polarization of the antennas is linear (vertical) or cross-polarized [25]. The cross polarization reduces interference between incoming and outgoing signals and allows employment of diversity techniques, however more hardware is necessary to accommodate the cross-polarization.

The majority of GSM base station parameters are confidential, thus Link budget analysis cannot be performed for ground connectivity with precise numerical values. Therefore approximated values will be taken for the estimation that is available in literature.

2.2 Coverage

GPS

The coverage for the GPS communication is characterized by the beam width angle which covers a certain section of the sky where at least a minimum number of GPS satellites is visible. The number of visible satellites can be estimated in the following way. First the 31 GPS satellites are equally distributed along 6 orbits which are equidistant around the Earth. From any point on the surface of the Earth a certain section of the sphere can be seen where the GPS satellites orbit. Figure 2.4 shows the graphical representation of the Earth and GPS satellites in scale.

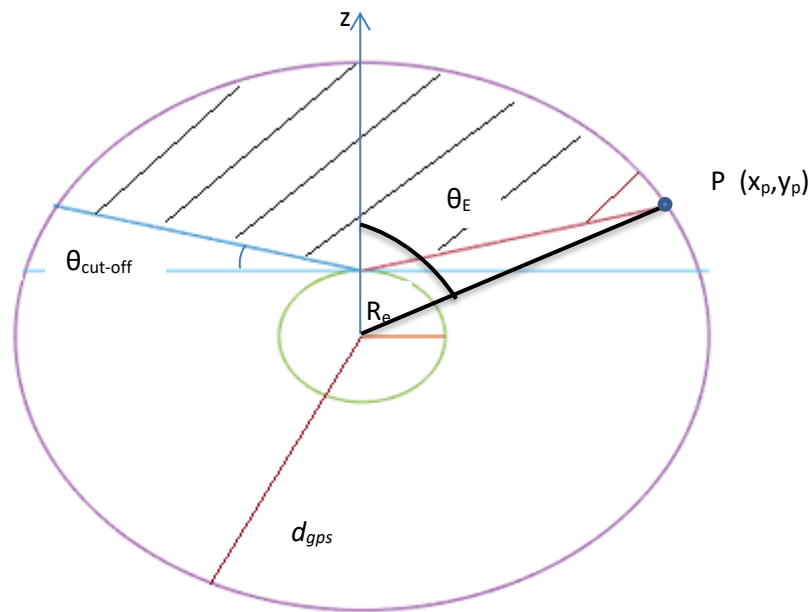


Figure 2.4 Schematic View of the Earth, GPS orbit and coverage area at 15° cut off angle; to scale

Note that the Earth is assumed to have a spherical shape with constant radius. The total surface area of a sphere at GPS altitude is calculated as follows:

$$A_{GPS\ Total} = 4\pi R^2$$

$$R = R_e + d_{gps}$$

Where R_e is the radius of the Earth and d_{gps} is the altitude of the GPS satellites from the Earth's surface. From the horizon of the observer on Earth the cut-off angle is set to 15°. Then the angle θ_E from the z-axis to the cut-off angle is calculated as follows:

$$y_1 = mx + c$$

$$y_2 = \sqrt{R^2 - x^2}$$

Where m is the gradient of the line from the Earth's observation point to the cut-off point at the GPS altitude at point $P(x_p, y_p)$ which equals to $\tan(15^\circ)$;

c is the Earth's radius, R_E . The origin of the axis is at the center of the Earth. Equating y_1 and y_2 gives x- and y-coordinates at point P. Then θ_E is straightforward to calculate:

$$\theta_E = 90^\circ - \arctan\left(\frac{y_p}{x_p}\right)$$

The area of the visible section of the sky where observer can see GPS satellites is:

$$A_{visible\ GPS} = \int_0^{2\pi} \int_0^{\theta_E} R^2 \sin \theta \, d\theta \, d\varphi = 2\pi R^2 [1 - \cos \theta_E]$$

The number of satellites that are visible from the observer's location, N_{GPS} at 15° cut off angle is calculated and rounded down:

$$N_{GPS} = \frac{A_{visible\ GPS}}{A_{GPS\ Total}} * N_{Total\ GPS}$$

Where $N_{Total\ GPS}$ is the total number of GPS satellites around the Earth. Table 2.3 shows all the input and output parameters:

Table 2.3 Input and Output parameters for estimating number of visible GPS satellites

Input Parameters		Output Parameters			
R_e	6371 km	R	26571 km	θ_E	61.6°
d_{gps}	20200 km	$A_{GPS\ Total}$	$8.872 \times 10^9 \text{ km}^2$	$A_{visible\ GPS}$	$2.326 \times 10^9 \text{ km}^2$
$\theta_{cut-off}$	15°	x_p	23 375 km	N_{GPS}	8 satellites
$N_{Total\ GPS}$	31 satellites	y_p	12 634 km		

This is verified with available literature data as shown in Figure 2.5.

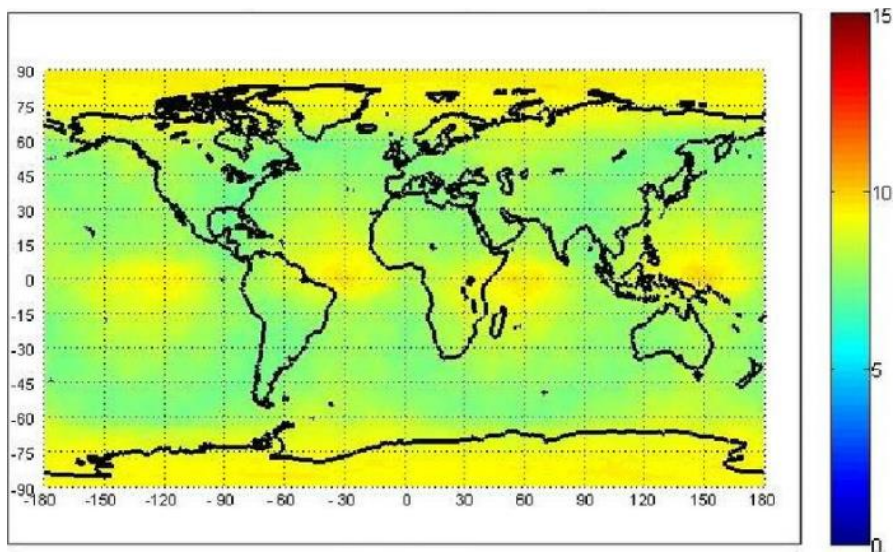


Figure 2.5 Average number of visible satellites (15 degrees elevation cut-off angle) of the 31 satellites GPS constellation on a worldwide basis over 24 hour period [26]

From Figure 2.5 it can be seen that from certain locations on Earth there are 9 and even 10 satellites are visible. But on average from majority of observation points on Earth there are at least 8 satellites that are visible.

Beam Width

Next step is to determine the coverage by calculating the amount of area that needs to be illuminated by the antenna in order to reach sufficient number of the GPS satellites. Since the aircraft is cruising at 11km altitude, there will be extra elevation angle that can reach satellites below the horizon with respect to the aircraft’s altitude. This is shown in Figure 2.6.

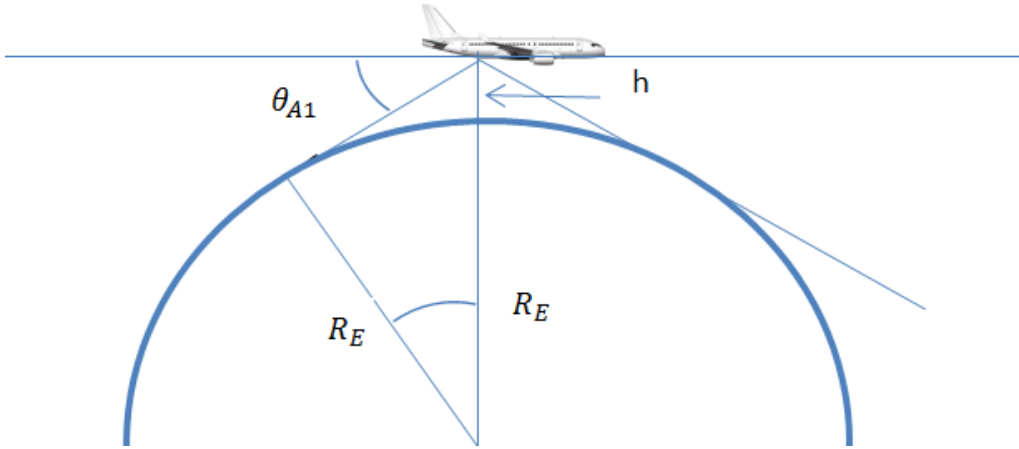


Figure 2.6 Schematic view of the aircraft flying at cruising altitude above the Earth; (not to scale)

The angle below the horizon where the aircraft can still reach the satellites is calculated as follows.

$$\theta_{A1} = 90^{\circ} - \arcsin \frac{R_E}{R_E + h} = 3.4^{\circ}$$

Where h is the aircraft’s cruising altitude 11km and R_E is the radius of the Earth 6371km. Figure 2.7 shows schematic view of the aircraft flying at cruising altitude above the Earth and the GPS satellite’s orbit to scale.

$$\theta_{E2} = \arccos \left[\cos \theta_{E1} + \frac{A_{visible\ GPS}}{2\pi R^2} \right]$$

Then finding the x- and y- coordinates at point P₂:

$$x_{P2} = R \sin \theta_{E2}$$

$$y_{P2} = R \cos \theta_{E2}$$

$$\theta_{A2} = \arctan \left(\frac{y_{P2} - c_A}{x_{P2}} \right)$$

Table 2.4 shows all the input and output parameters.

Table 2.4 Input and Output parameters for estimating number of visible GPS satellites and minimum Beam Width Angle

Input Parameters		Output Parameters			
R_e	6371 km	R	26571 km	θ_{E1}	79.5°
d_{gps}	20200 km	c_A	6382 km	θ_{E2}	63.9°
θ_{A1}	3.4°	x_{P1}	26 128.5 km	θ_{A2}	12.5°
$N_{Total\ GPS}$	31 satellites	y_{P1}	4 829.7 km	$A_{visible\ GPS}$	1.145 x 10 ⁹ km ²
$N_{GPS\ min}$	4 satellites	x_{P2}	23 861 km	m_1	tan(-3.4°)
h	11 km	y_{P2}	11 689 km	$\theta_{Coverage\ w.r.t\ A/C}$	15.9°
$A_{GPS\ Total}$	8.872 x 10 ⁹ km ²				

Therefore in order to reach at least 4 satellites the minimum coverage is 15.9° which starts 3.4° below the horizon at the cruising height with respect to the aircraft. All the power that is directed below 3.4° will be directed towards Earth and will not reach GPS satellites.

GSM

The maximum distance that the aircraft can reach is calculated by looking at Figure 2.4. This is the distance where the tangent touches the edge of the Earth's surface area where there is still a Line of Sight exists.

$$d_{a\ max} = \sqrt{(R_e + h)^2 - R_e^2} = 374.5\ km$$

However most cellular network sights do not provide signal in such large distances. For this measurement several radiation patterns of the ground base stations with GSM communication are analyzed. The GSM cell tower can reach maximum distance between 3.5km to 25 km in radius [27] however the gain is not isotropically distributed. Although some base station towers have a cell range that can reach as far as 75km, the maximum distance is taken as 14.25km by averaging the distances that GSM base station signal can reach with a typical ground base station [27]. For sufficient coverage an average value for half power beam width angles of an antenna is $\theta_{2d} = 79^\circ$.

Directivity

Directivity is determined based on Balanis for an omni-directional radiation pattern. This can be estimated as follows [28]:

$$D_{Omni-directional} = -172.4 + 191 \sqrt{0.818 + \frac{1}{HPBW(degrees)}}$$

For the antennas with a single major lobe and negligible minor lobes, the directivity is estimated in terms of the product of the half-power beamwidths in two perpendicular planes shown in Figure 2.4. This can be estimated as follows [28]:

$$D_{Major\ Lobe} = \frac{4\pi \left(\frac{180}{\pi}\right)^2}{\theta_{1d}\theta_{2d}}$$

Where θ_{1d} is the half power beamwidth in one plane measured in degrees, and θ_{2d} is the half power beam width in a plane at right angle to the other angle. This is illustrated in Figure 2.8. For sufficient coverage an average value for half power beam width angles of an antenna are $\theta_{1d} = 82^\circ$ and $\theta_{2d} = 79^\circ$.

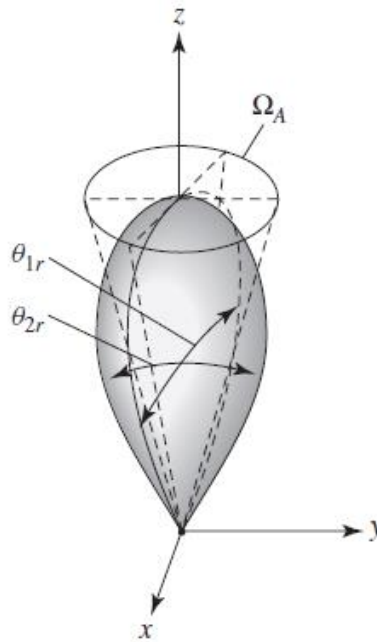


Figure 2.8 Beam Solid angle in terms of two perpendicular half power beamwidths for nonsymmetrical radiation pattern [28]

Substituting the values results in:

$$D_{GPS} = 6.86 = 8.36 \text{ dB}$$

$$D_{GSM} = 6.37 = 8.04 \text{ dB}$$

Gain

Gain of an antenna can be further derived from the directivity with a given antenna efficiency. The antenna efficiency indicates how much losses occur due to reflections based on mismatch between the transmission line and the antenna [28].

$$G = e_0 D$$

Where e_0 is the total antenna efficiency which includes the following factors:

$$e_0 = e_r e_c e_d$$

Where e_r is the reflection mismatch efficiency, e_c is the conduction efficiency and e_d is dielectric efficiency. Usually e_c and e_d are very difficult to compute and even by measurements they cannot be separated.

$$G_{GPS} = 0.9 * 6.86 \leq 7.90 \text{ dB}$$

$$G_{GSM} = 0.9 * 6.11 \leq 7.40 \text{ dB}$$

Therefore, in order to have sufficient coverage the gain for GPS should not exceed 7.90dB and for a GSM link 7.40 dB respectively.

2.3 Link Budget Analysis

GPS

In this section, using Friis formula, the link budget analysis will be determined [29]:

$$P_r = P_t + G_r + G_t + 20 \log_{10} \left(\frac{\lambda}{4\pi d} \right) - P.L.$$

Where

- P_r is the receiver power
- P_t is the power delivered to the terminals of an ideal isotropic transmit antenna
- G_r is the gain of the receiving antenna
- G_t is the gain of the transmitted antenna
- d is the distance between antennas (on aircraft and GPS satellite)
- λ is the wavelength
- $P.L.$ is the polarization losses of the antenna

The following assumptions are made

- $d \gg \lambda$, implying far field conditions
- Antennas are appropriately aligned and have the same polarization
- The multipath is neglected

Next, the equation for signal to noise ratio (SNR) is presented, where P_N is the noise power which indicates the minimum detectable signal of the receiver.

$$SNR_{min} = P_r - P_N$$

Table 2.5. summarizes the input and output values for the GPS link found in [19, 20].

Table 2.5 Input and Output parameters for the Link budget analysis for GPS link

Input Parameters				Output Parameters	
P_t	14.1dB	$d_{GPS\ min}$	20189 km	P_r	-158.4dB+ G_R
G_t	13 dBi	$SNR_{GPS\ min}$	20 dB	$G_{R\ min}$	-12.6dB
f	1.575 GHz	P.L.	3 dB		
λ	0.1905 m	P_N	-161dBm [30]		

Different Transmission Range Options

Two main options for transmission range are going to be considered for GPS power link budget analysis. Option 1 corresponds to the minimal distance between aircraft and the GPS satellites where the satellites is located right above the aircraft. Option 2 represents the furthest distance away from the aircraft where GPS satellite can be reached at point P₁ shown in Figure 2.7. Table 2.6 shows the resulting minimal gain that antenna should have in order to reach minimum signal to noise ratio.

Table 2.6 Different Transmission Range options and the required minimum receiver Gain

	Option 1	Option 2
Distance, d	20 189 km	26 081 km
$G_{R\ min}$	-12.6dB	-10.4 dB

Depending on the location of the GPS satellites with respect to the aircraft the resulting difference due to the path loss is 2.2dB. The minimum gain of the receive antenna on the aircraft should be not smaller than -10.4dB.

GSM

For the GSM wireless communication link the Friis equation is used and the same approach is applied. The range of distances can be calculated by first considering the radiation pattern of the GSM base station.

$$P_N = 10 \log_{10}(kTB) + N.F.$$

Where

- k is the Boltzmann constant,
- T is the Temperature at the cruise altitude
- B is the bandwidth
- $N.F.$ is the noise figure of the receiver

Table 2.7 summarizes the values for the GSM wireless link found in [25, 27].

Table 2.7 Input and Output parameters for the Link budget analysis for GSM link

Input Parameters				Output Parameters	
P_t	19dB	$d_{GSM\ min}$	11 km	P_N	-133.1dB
G_t	-10 dBi	$SNR_{GSM\ min}$	20 dB	P_r	-102.3dB+ G_R
f	800 MHz	B	10MHz	$G_{R\ min}$	-10.8dB
λ	0.375 m	<i>N.F.</i>	2 dB		
k	$1.38 * 10^{-23}$ $m^2 kgs^{-2} K^{-1}$	T	223 K [31]		

Different Transmission Range Options

Similarly to the GPS communication link, two main options for transmission range are going to be considered for GSM power link budget analysis. Option 1 corresponds to the minimal distance between aircraft and the ground base station where the GSM tower is located right below the aircraft. Option 2 represents the furthest distance away from the aircraft where signal can reach the ground base station. This is determined by the coverage and the field of view determined in previous section. The maximum distance for the GSM antenna is 14.25km.

Table 2.8 shows the resulting minimal gain that antenna should have in order to reach minimum signal to noise ratio.

Table 2.8 Different Transmission Range options and the required minimum receiver Gain for GSM link

	Option 1	Option 2
Distance, d	11 km	14.25 km
$G_{R\ min}$	-10.8 dB	-8.5dB

Depending on the location of the GPS satellites with respect to the aircraft the resulting difference due to the maximum path loss is 2.3dB. The minimum gain of the receive antenna on the aircraft for GSM communication should not be smaller than -8.5dB.

2.4 Antennas Selection

The two antenna types are selected as a preliminary representative prototypes: monopole for the GPS communication link and a patch microstrip antenna for the GSM communication link. For the communication with the ground, the selected antenna shall have a hemispherical radiation pattern. And for the communication with the GPS satellites, a monopole antenna is chosen because it has a toroidal, donut shape radiation pattern which can reach the satellites.

Monopole

The monopole antenna is designed to operate at a resonant frequency of 1.575GHz for the GPS communication link. The monopole is meshed using a thin wire approximation. The segment length is set to standard mesh size equivalent to $\lambda/12$. All the major approximations and design parameters for initial calculations are summarized as follows:

- Quarter wavelength monopole at 1.575 GHz resonant frequency
- The voltage source placed on the starting segment
- Starting segment is in direct contact with the flat plate
- Source Magnitude 1 Volt and phase 0°
- Antenna is meshed using Thin Wire approximation
- Segment size in radial direction is $\lambda/1000$
- Segment size along antenna's length is $\lambda/12 \rightarrow 4$ segments
- Antenna is placed along the positive Z-axis
- Size of the square edged plate is 1.5 wavelength centred at the origin of the main axis

After plotting and analysing the S-parameters of the initial design of the monopole antenna, it was evident that further optimization was necessary because the resonant frequency was not achieved at 1.575GHz, instead the minimum reflection occurred at 1.532 GHz. In order to match the resonant frequency, the length of the monopole antenna is varied. The resonant frequency is matched when the length of the monopole antenna is decreased by 1.29 mm. Figure 2.9 shows the S-parameters and Figure 2.10 shows the radiation pattern at the resonant frequency of the optimized monopole antenna.

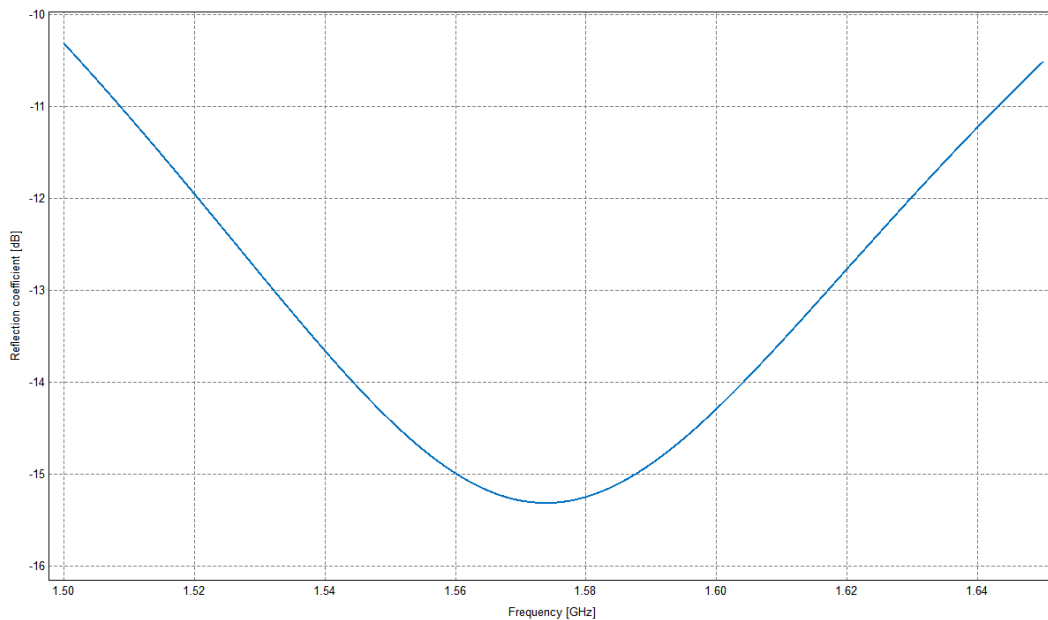


Figure 2.9 S-parameter for the optimized monopole antenna for GPS communication at 1.575GHz

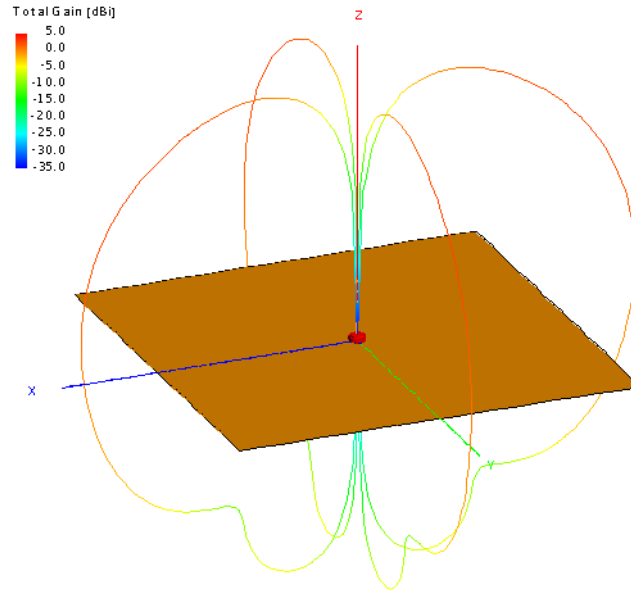


Figure 2.10 Radiation pattern for the optimized monopole antenna on a square plate at 1.575GHz for the GPS communication; dB Scale

Patch

Microstrip Patch antennas offer many advantages compared to many other antenna configurations. The advantages include low fabrication costs, lightweight, robustness when mounted on rigid surfaces and others. Therefore microstrip patch antenna is chosen as the radiating antenna for GSM communication link.

A coaxial feed rectangular microstrip antenna is designed to operate at resonance frequency of 800 GSM band. The height of the substrate is taken to be 2.54mm (as one of standard heights for RT/Duroid substrate readily available in market) with dielectric constant $\epsilon_r=2.2$. Various steps are involved in designing and optimizing a properly operating patch antenna. Patch dimensions and feed location have a strong effect on the performance [32].

Initial design antenna dimensions are calculated using the following equations [32, 33]:

$$W = \frac{c}{2f_0 \sqrt{\frac{\epsilon_r + 1}{2}}}$$

$$L = \frac{c}{2f_0 \sqrt{\epsilon_{eff}}} - 0.824h \frac{(\epsilon_{eff} + 0.3) \left(\frac{W}{h} + 0.264\right)}{(\epsilon_{eff} - 0.258) \left(\frac{W}{h} + 0.8\right)}$$

$$\epsilon_{eff} = \frac{\epsilon_r + 1}{2} + \frac{\epsilon_r - 1}{2} \left[\frac{1}{\sqrt{1 + 12 \frac{h}{W}}} \right]$$

$$L_g = 6h + L$$

$$W_g = 6h + W$$

Where c , is the speed of light and is equal to $3 \cdot 10^8$ m/s,
 f_0 is the resonance frequency of 800MHz,
 ϵ_r is the dielectric constant which equals to 2.2,
 W is the width of the patch antenna,
 ϵ_{eff} is the effective dielectric constant,
 h is the height of the substrate which equals to 2.54 mm,
 L is the length of the patch antenna,
 L_g is the length of the ground plane,
 W_g is the width of the ground plane

Table 2.9 shows the initial estimation of the patch antenna dimensions for GSM communication at 800MHz.

Table 2.9 Geometrical Parameters for Patch Antenna with Initial calculation

Dimension	Value
ϵ_r	2.2 [-]
L_g	140 [mm]
W_g	163 [mm]
h	2.54 [mm]
L	125 [mm]
W	148 [mm]
$X_{feeding}$	8 [mm]
$Y_{feeding}$	74 [mm]
Frequency	800 [MHz]

After plotting and analysing the S-parameters of the initial design of the patch antenna, it was evident that further optimization was necessary because the resonant frequency was not achieved at 800 MHz. In order to match the resonant frequency, the length of the patch antenna is varied. Decreasing the length resulted in shifting the resonant frequency to the right. The optimum value is achieved when length is decreased to 123.5mm. Variation of width did not influence the resonant frequency.

The next step in optimization is to find the feed point location such that the input impedance is 50 Ohms for the specified resonant frequency [33]. Increasing the offset along the width results in less variation of the reflection coefficient therefore the Y-coordinate of the pin is set along the middle line of the width [32]. The FEKO 2017 is used in order to perform the optimization of the feeding pin location. After numerous iterations the X-coordinate of the feeding point is found at 18.6 mm with respect to the center of the patch. The width has also an influence on the reflection coefficient therefore with trial and error technique the -10dB reflection coefficient bandwidth is found to be maximum when width is set to 160 mm.

Table 2.10 summarizes the final patch antenna dimensions that were optimized.

Table 2.10 Optimized Patch antenna dimensions

Dimension	Value
L_g	139 [mm]
W_g	175 [mm]
h	2.54 [mm]
L	123.5 [mm]
W	160 [mm]
$X_{feeding}$	18.6 [mm]
$Y_{feeding}$	80 [mm]
Frequency	800 [MHz]

Figure 2.11 shows the S-parameters and Figure 2.12 shows the radiation pattern at the resonant frequency of the optimized patch antenna.

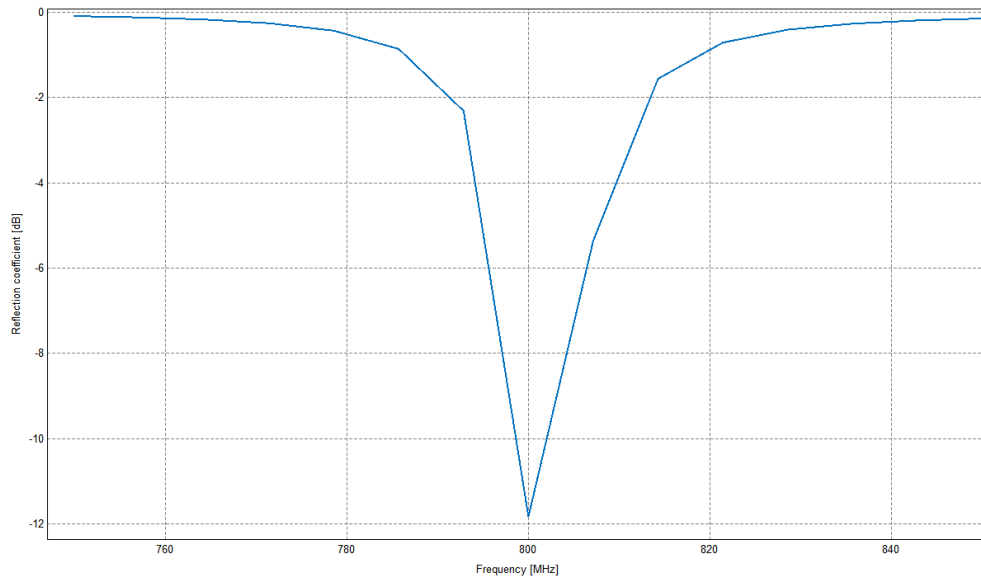


Figure 2.11 S-parameter for optimized microstrip patch antenna for GSM communication

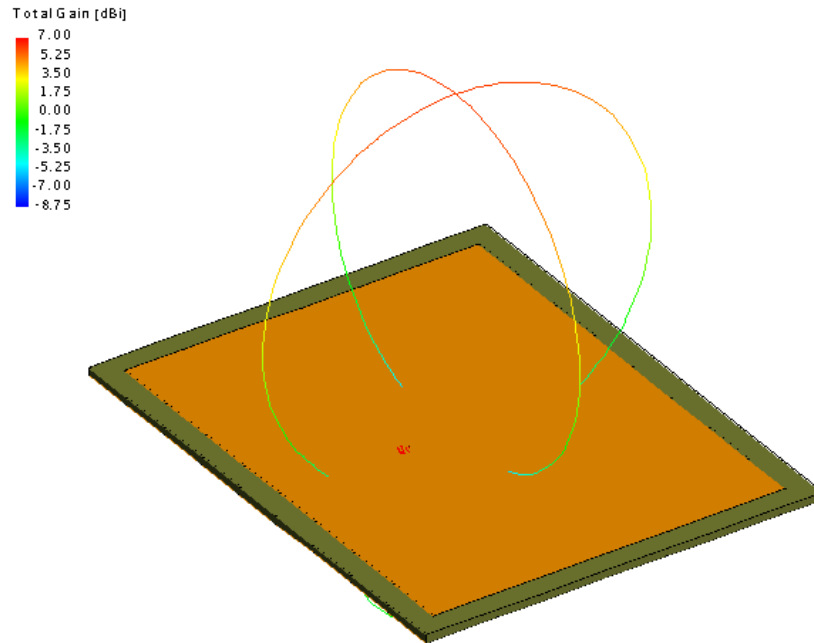


Figure 2.12 Radiation pattern for optimized microstrip patch antenna at 800MHz for GSM communication; dB Scale

From Figure 2.12 it can be seen, that the simulation results in a classical hemispherical radiation pattern of a patch antenna. The maximum Gain value is 7dBi at theta=0.

Coupling Effect

Since the monopole and the patch are going to be located in the close proximity next to each other, it is important to investigate the effect of coupling and measure the S_{21} and S_{12} parameters. The distance between the patch and monopole is two wavelengths with respect to the GPS frequency away from each other. Figure 2.13 shows the geometrical illustration of the two antennas, where the ground plane is shared between the two of them.

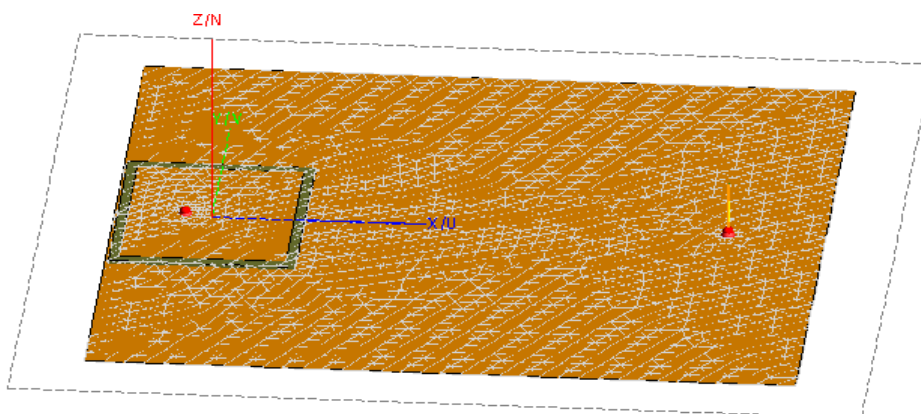


Figure 2.13 Geometrical distance between monopole and patch antennas to take into account the coupling effect

The S_{11} , S_{22} and S_{21} parameters are shown in Figures 2.14, 2.15 and 2.16 respectively.

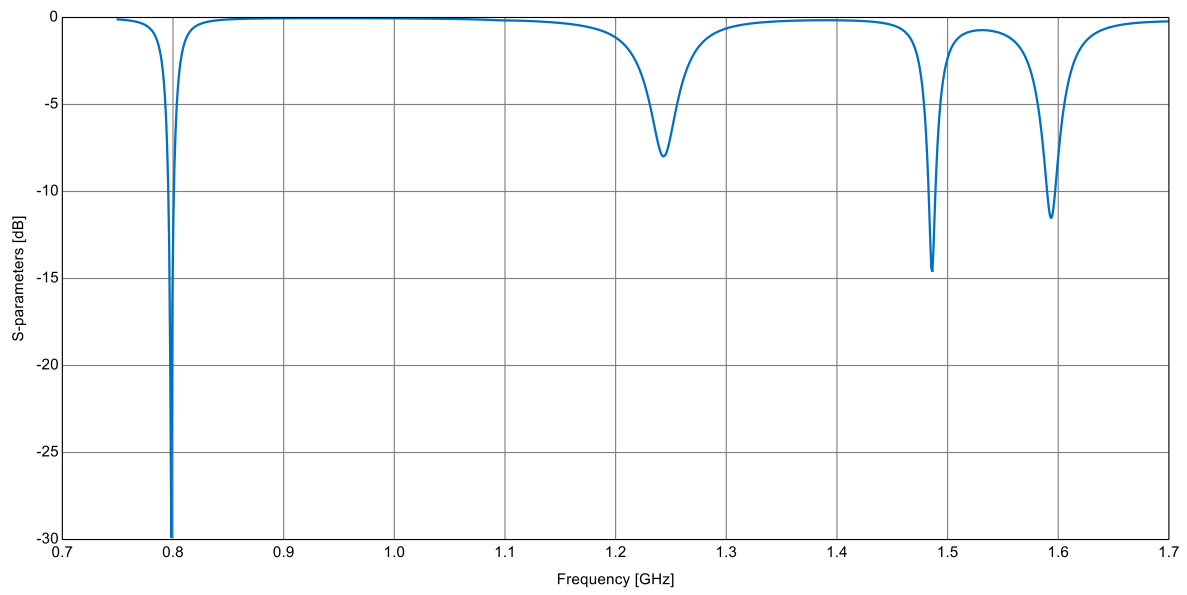


Figure 2.14 S_{11} parameter representing the patch antenna

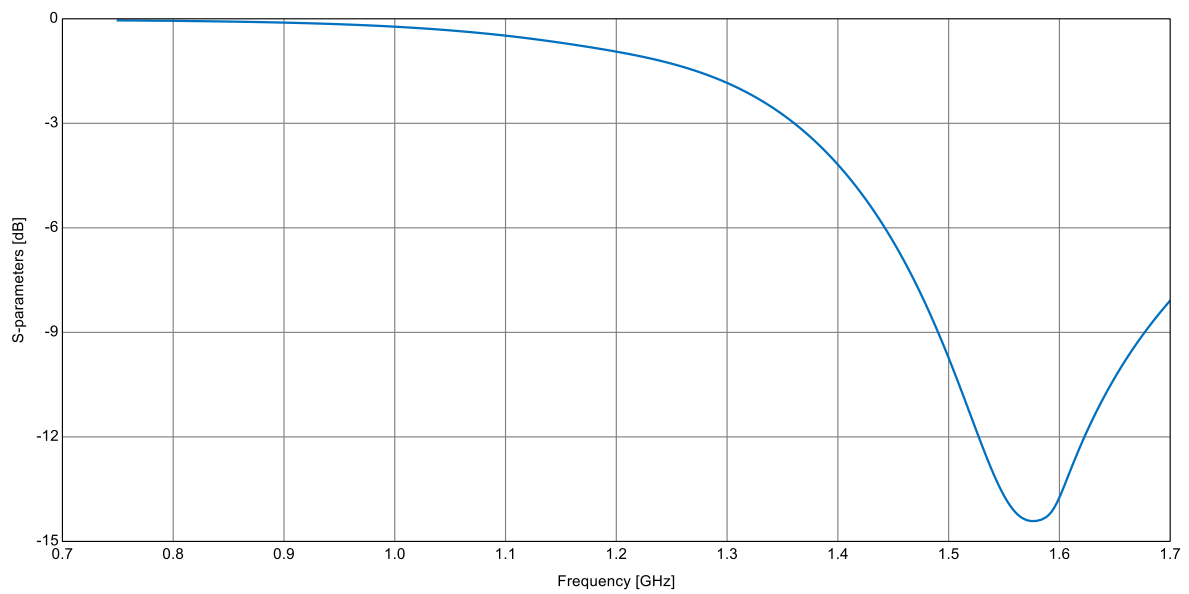


Figure 2.15 S_{22} parameter representing the monopole antenna

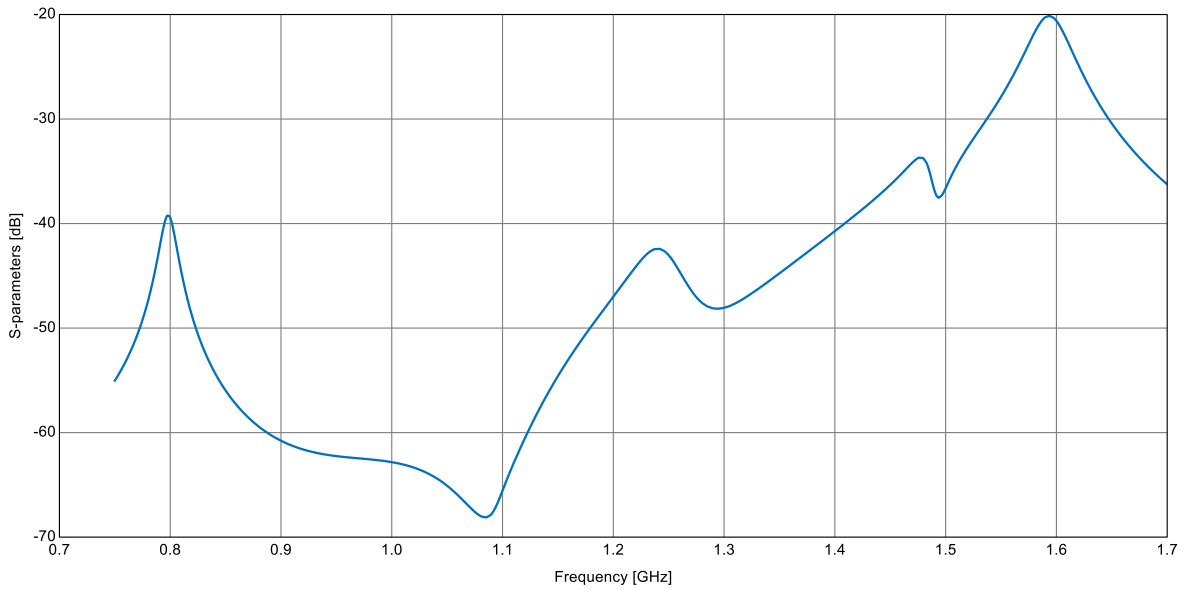


Figure 2.16 S_{21} parameter representing transferred power from patch to the monopole antenna

The presence of the monopole antenna resulted in a shift of the resonant frequency of the patch antenna. Therefore it had to be further optimized in terms of the length in order to match the resonant frequency. From Figure 2.14 it can be seen that the S_{11} parameter of the patch antenna has some peaks near the resonant frequency for the monopole. This can also be observed in Figure 2.16 with the S_{21} parameter. At the frequency of 800 MHz the S_{21} is -40dB and at the frequency of 1.575GHz the S_{21} is -22.9 dB. The S_{22} parameter is hardly effected. This can be seen in Figure 2.15. The reflection coefficient of the monopole is not noticeably influenced by the presence of the patch antenna.

2.5 Conclusion

In this chapter the key requirements are identified and the system elements are analysed. The antenna system is chosen which consists of 2 individual antennas. The quarter wavelength monopole operating at 1.575 GHz in L1 band for the GPS communication and a patch antenna with dielectric constant of 2.2 for the substrate operating at 800 MHz for the GSM communication. In order for the monopole and patch antennas operate in their respective resonant frequencies, the dimensions are optimized. At the frequency of 800 MHz the S_{21} parameter is -40dB and at the frequency of 1.575GHz the S_{21} parameter is -22.9dB. Optimizing the dimensions of the monopole has a strong effect on the reflection coefficient S_{11} parameter for the patch antenna. However changing and optimizing the dimensions of the patch antenna does not have a strong influence on the S_{22} parameter of the monopole.

In order to satisfy the coverage and link budget analysis the required operational gain range for the GPS link should be between -10.4dB to 7.9dB; and for the GSM link the minimum gain of the receive antenna on the aircraft should not be smaller than -8.5dB and should not exceed 7.4dB.

Chapter 3 Overview of CEM Simulation Methods

In this Chapter the theory about the computational EM methods are described. The following simulation methods which are available in FEKO 2017 will be considered: Method of Moments (MoM), Multi-level Fast Multipole Method (MLFMM), Physical Optics (PO) and Uniform Theory of Diffraction (UTD).

Comparison of Simulation Methods in FEKO 2017

In order to answer the research question, the main simulation platform that will be used for estimating the radiation pattern is FEKO 2017. There are two sub-programs where the modelling and implementation can be performed: EDITFEKO and CADFEKO. The advantage of using CADFEKO is that it provides a visual overview of every newly constructed element. So in case a dimension error has been made, it becomes immediately visible and therefore it is easier to verify and correct the model. Another important advantage is that CADFEKO includes all the output parameters for the radiation pattern in different parameters such as electric field, directivity and gain. In EDITFEKO a programming language is used where every scripted line has to be specified and every output parameter has to be requested separately. Therefore the main simulations are performed in CADFEKO.

3.1 Method of Moments

Description of the Method

The core solution of the program FEKO is based on the Method of Moments (MoM). The MoM is a full wave solution of Maxwell's integral equations in the frequency domain. In the MoM mode the classical Gaussian elimination process is used to solve the matrix system. An advantage of the MoM is that it is a "source method" meaning that only the structure in question is discretised, not free space as with "field methods". The MoM treats each of N basis functions in isolation, thus resulting in an N^2 scaling of memory requirements (to store the impedance matrix) and N^3 in CPU-time (to solve the linear set of equations) [34].

'The Surface Equivalence Principle SEP introduces equivalent electric and magnetic currents on the surface of a closed dielectric body. The currents are calculated using a linear combination of basis functions, where the coefficients are obtained by solving a system of linear equations' [34]. Once the current distribution is known, further parameters can be obtained such as the near field, the far field, radar cross sections, directivity, gain or the input impedance of antennas.

Solver features

Material and Boundary conditions

‘The FEKO solver can handle lossy and loss free dielectrics and magnetic materials, perfect electric and magnetic conductors as well as imperfectly conducting conductors’ [34]. Boundary conditions do not have to be set and memory requirements scale proportional to the geometry in question and the required solution frequency.

Thin Wires

The FEKO solvers incorporate a wire method that stays stable even for small wire segment discretization. However it is important to set the appropriate ratio of the segment radius to the segment length. Surface-wire junctions as well as wire-wire junctions can be handled. This will be applicable for the monopole antenna system.

Applicability

The advantage of this method is high accuracy at moderate computational complexity, given an adequate choice of the segmentation size. However method of moments is restricted to the analysis of electromagnetic radiating structures which are small in terms of the wavelength [34,35].

Typically structures of the size up to five or ten wavelengths can be treated. Typical applications include antenna and waveguide designs. Figure 3.1 demonstrates the radiation pattern of a horn antenna calculated using MoM.

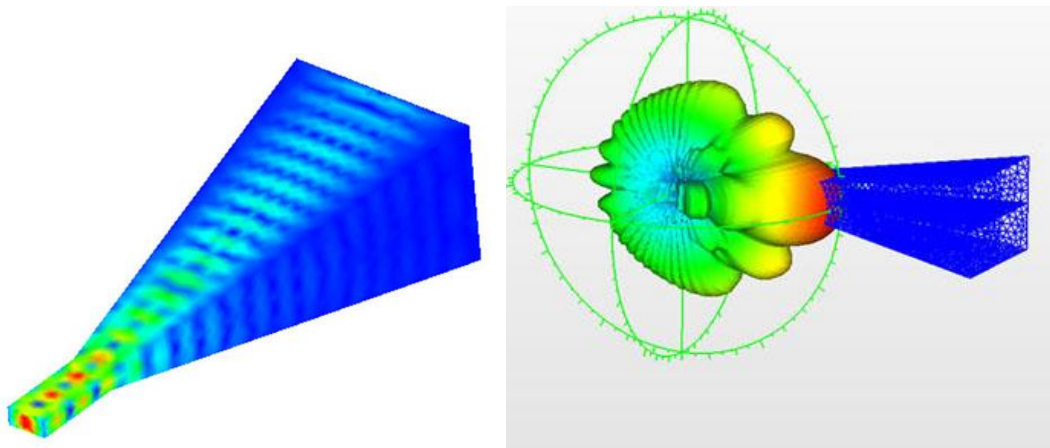


Figure 3.1 Example of a Standard gain horn antenna computed with MoM [35]

3.2 MLFMM

The MLFMM is an alternative formulation of the technology behind the MoM and is applicable to much larger structures than the MoM, making full-wave current-based solutions of electrically large structures possible. This fact implies that it can be applied to most large models that were previously treated with the MoM without having to change the mesh.

Description of method

‘The agreement between the MoM and MLFMM is that basis functions model the interaction between all triangles. The MLFMM differs from the MoM in that it groups basis functions and computes the interaction between groups of basis functions, rather than between individual basis functions’ [34]. FEKO employs a boxing algorithm that encloses the entire computational space in a single box at the highest level, dividing this box in three dimensions into a maximum of eight child cubes and repeating the process iteratively until the side length of each child cube is approximately a quarter wavelength at the lowest level [34, 35]. Only populated cubes are stored at each level, forming an efficient tree-like data structure, whereas empty boxes are discarded. ‘In the MoM framework the MLFMM is implemented through a process of aggregation, translation and disaggregation of the different levels’ [34]. Using the MLFMM the complexity in the matrix-vector multiplication is reduced significantly compared with MoM as is illustrated in Figures 3.2 and 3.3 respectively.

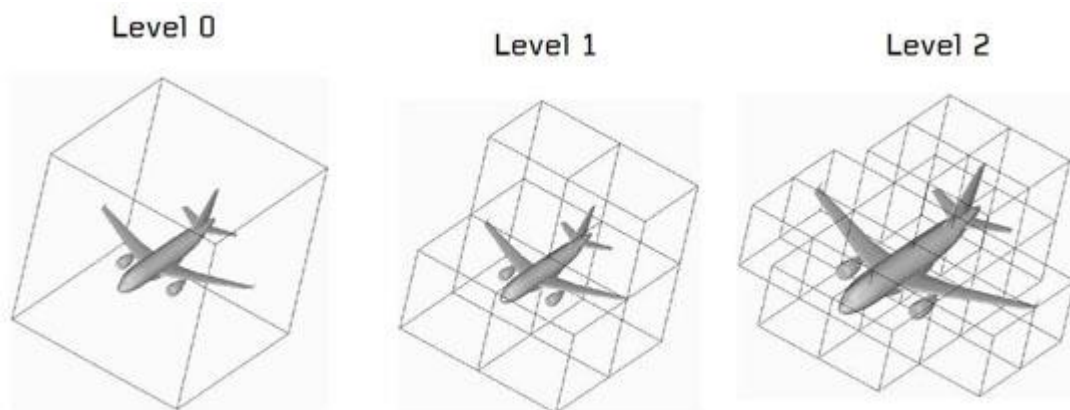


Figure 3.2 MLFMM partitioning at different levels using boxing partitioning algorithm [35]

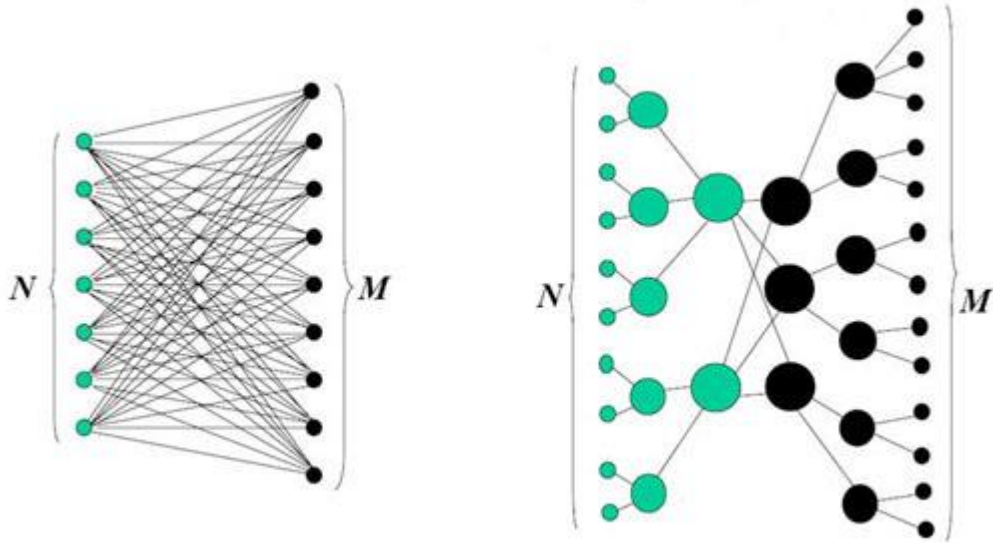


Figure 3.3 MoM (left) and two level MLFMM complexity (right) [35]

It is thus clear that processing requirements for MoM solutions scale rapidly with increasing problem size. The MLFMM formulation's more efficient treatment of the same problem as MoM method, results in $N \cdot \log(N)$ scaling in memory and $N \cdot [\log(N)]^2$ in CPU time. In real applications this reduction in solution requirements can range to orders of magnitude [34]. After Fourier Transform on the basis functions is performed, the solution of the linear set of equations is achieved when the residuum offset error becomes smaller than 0.003 or after 500 iterations.

Solver features

Material and Boundary conditions

Similarly to MoM, the MLFMM solver can handle lossy and loss free dielectrics and magnetic materials, perfect electric and magnetic conductors as well as imperfectly conducting conductors. Boundary conditions do not have to be set.

Minimal Residual Interpolation

The MLFMM solver use the MRI (Minimal Residual Interpolation) method that reduces the number of iterations in the iterative MLFMM solver for multiple right hand sides such as in case of estimating monostatic RCS computations. The MRI method computes an optimal initial guess of the solution of a particular right hand side used by the iterative solver. The initial guess is based on previously computed solutions and is optimal in the sense that the residual of the initial guess is minimized. Given an optimal initial guess the number of iterations in the iterative MLFMM solver is drastically reduced with great savings in solution time. After a certain number of solutions have been computed the remaining solutions can be computed by pure interpolation.

Applicability

The MLFMM solver is suitable for analysis of very large problems where standard MoM is no longer applicable. Typical applications include finite size antenna array, antenna integration on large structures, radar cross section (RCS) analysis and reflector antenna designs. Table 3.1 summarizes estimated memory requirements for the MLFMM and MoM for some typical applications such as antenna installation and estimating RCS for a military aircraft.

Table 3.1 Estimated memory requirement for the MLFMM and MoM for some typical applications [35]

Application and Frequency	Number of unknowns	MoM	MLFMM
Satellite 1.5-2GHz	100000	150 Gb	1 Gb
Antenna installation at 1GHz	400000	2,4 Tb	4,5 Gb
RCS of military aircraft at 3 GHz	1 500 000	33,5 Tb	18 b

3.3 Physical Optics

Description of the method

‘PO is a high frequency approximation (short-wavelength approximation) that is an intermediate method between geometric optics, which ignores wave effects, and full wave methods such as MoM or MLFMM. The geometrical optics current is used over the illuminated portions of the target surface, while zero current is assumed over the shadowed portions. The current is then used in the radiation integrals to compute the scattered far field from the target. PO gives best results for electrically large bodies and is most accurate in the specular directions’ [35].

Solver features

‘The PO solver is based on a triangular surface mesh such as MoM or MLFMM but also on a Non-uniform Rational Basis Spline (NURBS) geometry representation’ [35]. Non-uniform rational basis spline (NURBS) is a mathematical model used for generating and representing curves and surfaces. ‘The NURBS is used to determine which parts that are illuminated or not. Approximate shadow regions are obtained efficiently on the NURBS surfaces using raytracing techniques [35].

Applicability

'The PO solver is suitable for analysis of very large problems where the electrical size of the problem is too large for MLFMM. Typical applications include antenna integration on large structures and radar cross section analysis' [35]. Figure 3.4 illustrates comparison between computed directivity in H-field of a large electric body using MLFMM and Hybrid PO solvers.

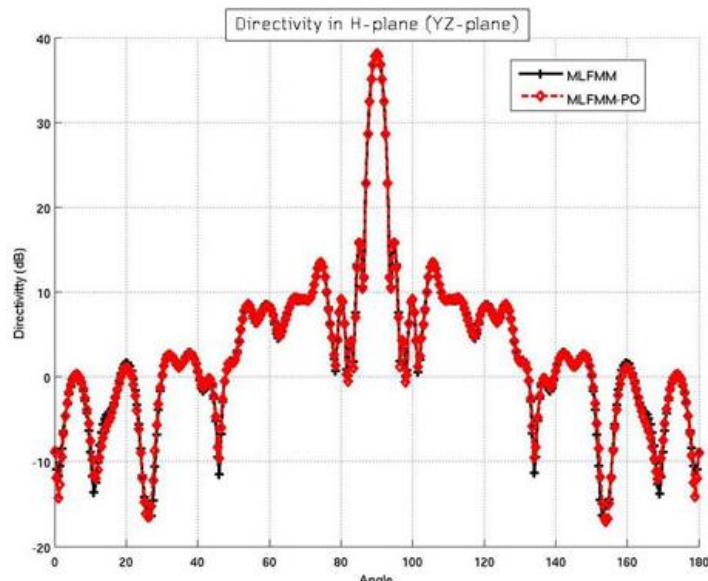


Figure 3.4 Directivity of a large electric body computed with MLFMM and PO [35]

3.4 Uniform Theory of Diffraction

Description of the method

FEKO hybridises the current based accurate MoM results with the UTD by means of the coupling, i.e. modification of the interaction matrix, ensuring accuracy. Frequency does not influence the memory resources required for UTD treatment of a structure as only points of reflection from surfaces and diffraction from edges or corners are considered without meshing the structure [34, 37]. Edge and corner diffraction, double diffraction and creeping waves are taken into account. Currently the numerical formulation of the UTD only allows it to be applied to flat polygonal plates with minimum edge length in the order of a wavelength or to single cylinders. Combination of cylinders and plates for a single object is not supported in FEKO. The UTD is thus quite well suited to the analysis of ships at radar or electronic wave frequencies, but not well suited to the analysis of complex objects with curved surfaces, e.g. auto mobiles. However approximating the geometry with simplified polygonal plates can provide first order estimations of the far field.

Furthermore, the UTD solver does not require any integration over the surface currents on an object that is excited by an external source, while the wave-optical Physical Optics (PO) method requires such integration' [12, 36].

Solver features

The UTD solution method has to be specified for every polygonal surface individually. This high frequency solution method provides several solver settings. Maximum number of ray interactions can be specified (i.e. reflection and diffraction combined). Also the ray contributions can be selected to be included or excluded in the analysis. Those ray contributions can take into account direct and reflected rays, edge and wedge diffractions, corner diffractions, double diffraction, creeping waves and the cone tip diffraction. These parameters should be specified depending on the geometry of the object.

Applicability

Similarly to the PO solver, the UTD solver is suitable for analysis of very large problems where the electrical size of the problem is too large even for the PO method to solve. Typical applications include antenna integration on large structures and the far field analysis. Figure 3.5 illustrates radiation pattern of a mobile communication antenna on the roof of a building computed using UTD solver [24, 37].

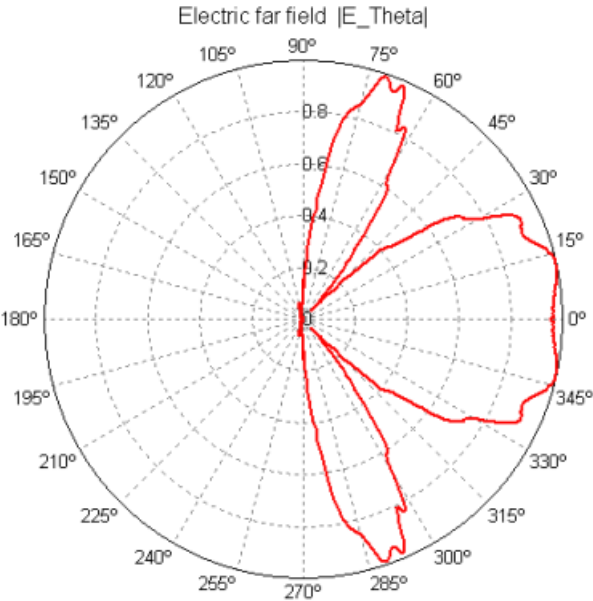


Figure 3.5 Radiation pattern of a mobile communication antenna on the roof of a building at frequency 900 MHz [34]

The UTD solver also allows to export an optional output file that includes the ray tracing technique. This option visually demonstrates the path of each illuminated ray travelling from the source and analysed at every angle. This is shown in Figure 3.6.

Ray type
■ Transmission and reflection
■ Diffraction

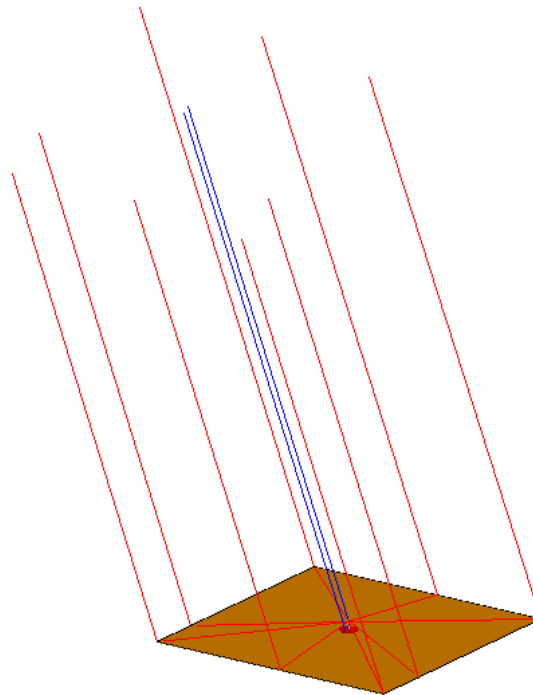


Figure 3.6 Visual representation of the ray tracing technique of a monopole on a PEC rectangular plate used in the UTD solver

3.5 Conclusion

The main simulation platform that will be used for estimating the radiation pattern is FEKO 2017. FEKO contains several solver options that can be used in order to perform a far field analysis. Each solver method has its own individual characteristics in terms of solution method, solver features and applicability.

The method of moments (MoM) technique forms the basis of the FEKO solver. The advantage of this method is high accuracy, given an adequate choice of the segmentation size. However method of moments is restricted to the analysis of electromagnetic radiating structures which are small in terms of the wavelength [34]. The MoM treats each of N basis functions in isolation, thus resulting in an N^2 scaling of memory requirements (to store the impedance matrix) and N^3 in CPU-time (to solve the linear set of equations).

The MLFMM is an alternative formulation of the technology behind the MoM and is applicable to much larger structures than the MoM. The MLFMM's formulation is a more efficient treatment of the same problem results in $N * \log(N)$ scaling in memory and $N * \log(N)^2$ in CPU time. MLFMM solver groups basis functions and computes the interaction between groups of basis functions, rather than between individual basis functions. It employs a boxing algorithm to divide and solve the set of linear equations using a fixed number of iterations or until a certain residuum value is reached.

The Physical Optics is a high frequency approximation solver used for estimating radar cross sections or radiation patterns for electrically large structures. It is based on a triangular surface mesh similarly to MoM or MLFMM.

The UTD solver is a perfect tool for estimating the far fields of electrically very large structures. Frequency does not influence the memory resources required for UTD treatment of a structure as only

points of reflection from surfaces and diffraction from edges or corners are considered without meshing the structure. Edge and corner diffraction, double diffraction and creeping waves are taken into account. The main limitation is that the geometry has to be modelled as a set of flat metallic polygons with edge length not smaller than a wavelength.

Chapter 4 Feasibility Analysis

In this chapter the radiation patterns are computed by different CEM methods and in order to check the accuracy of the methods, the radiation patterns are compared in 3D and 2D plots. Two simple electrically large scattering bodies are chosen for analysis: a square plate and a cylinder. The radiation pattern of the selected antennas placed on the aircraft will be presented in Chapter 6.

The simulations are conducted using TU Delft Computer with the following specifications:

Rad Computer: PC WIN64 EM64T MKL IMPI -- TUD206016
Intel(R) Core(TM) i5-4670 CPU @ 3.40GHz
1 physical CPU with a total of 4 processors
RAM 8 GB

The simulation numerical platform is FEKO 2017 and CADFEKO as the main simulating sub-program.

4.1 Square Plate

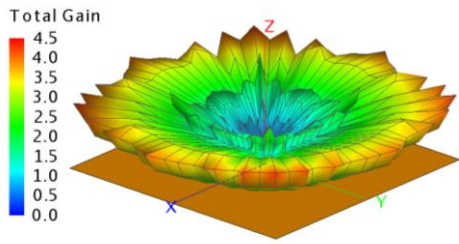
The square plates are considered in three different geometries: the edge length is taken as 10λ , 20λ and 30λ .

The radiating antenna is a quarter wave length monopole connected at the surface along z-direction. The frequency set to determine the radiation pattern is 800 MHz. The voltage source is added to the starting segment of the wire located between the monopole and the plate. The source magnitude is 1V and phase 0° . Table 4.1 summarizes all the parameters of the simulation.

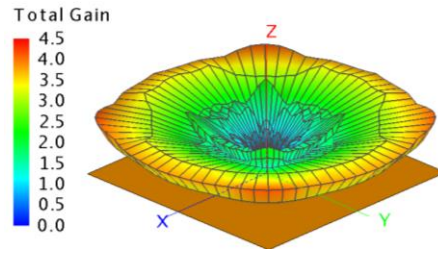
Table 4.1 Constant Parameters for all simulations for the square plate geometries

Frequency	800 MHZ
Antenna Mesh Size Radius	$\lambda/1000$
Antenna Mesh Size: Length	Standard Mesh Size: $\lambda/12$
Antenna Type	Monopole
Antenna Length	$\lambda/4$
Antenna Orientation	+ Z-axis

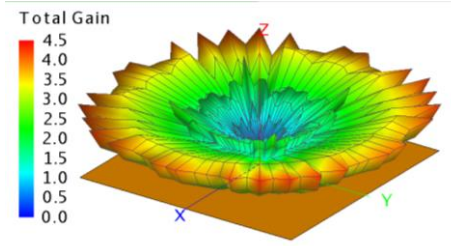
Figure 4.1 illustrates 3D radiation patterns computed with MLFMM, PO and UTD for a monopole on a square plate with edge of 10λ . Figures 4.2 and 4.3 show 2D radiation patterns corresponding to plots found in Figure 4.1 at the cut $\phi=0$ in decibels and linear scales respectively.



MLFMM: 10 iterations



PO: Full Ray Tracing



UTD: Direct and reflected rays,
edge and wedge diffraction,
creeping wave, double diffraction

Figure 4.1 3D Radiation Pattern of a monopole on a $10\lambda \times 10\lambda$ square plate; linear scale

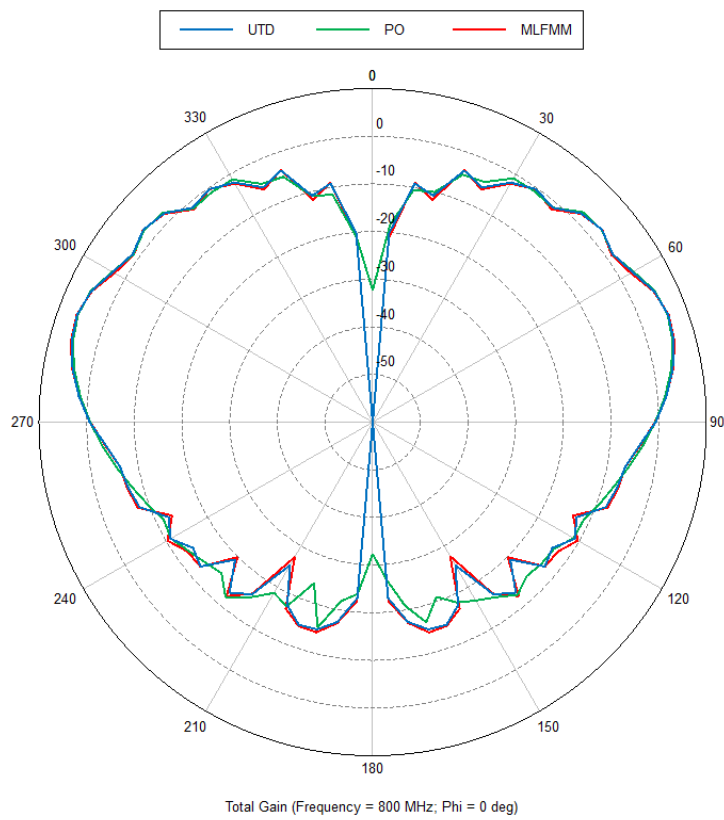


Figure 4.2 Comparison of radiation patterns in the far field at $\phi=0^\circ$ between MLFMM, PO and UTD for a monopole on a square plate $10\lambda \times 10\lambda$ at 800 MHz; dB scale

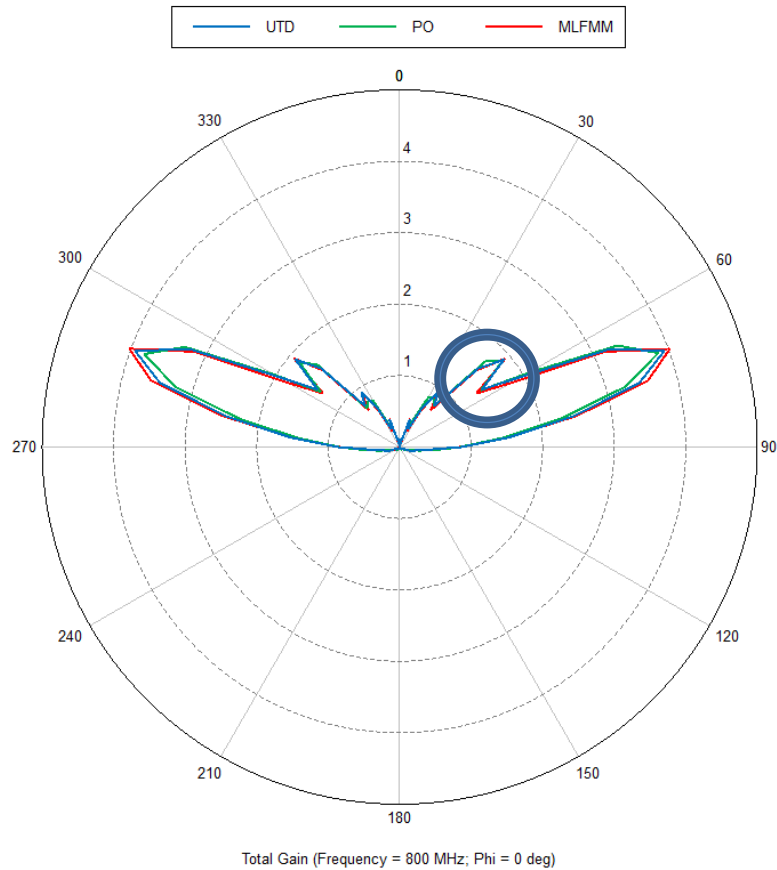


Figure 4.3 Comparison of radiation patterns in the far field at $\phi=0^\circ$ between MLFMM, PO and UTD for a monopole on a square plate $10\lambda \times 10\lambda$ at 800 MHz; linear scale

From Figures 4.1 to 4.3, an excellent agreement between MLFMM and UTD can be seen. For the UTD simulation settings all the options have been taken into account such as direct and reflected rays, edge and wedge diffraction, creeping wave and double diffraction. The PO also shows similar pattern however the radiation peaks are smoothed out. The difference at $\theta=270$ is about 7.5 dB as compared to UTD and MLFMM.

The spike at $\theta=50^\circ$ that is circled in Figure 4.3, can be explained by the fact that the edges of the plate reflect and scatter the EM waves and act as a secondary reflecting antenna, creating effect of a virtual antenna array. Due to symmetry, the same spikes are found in 3D model as can be seen in Figure 4.1.

Figure 4.4 illustrates 3D radiation patterns computed with MLFMM, PO and UTD for a monopole on a square plate with edge of 20λ . Figures 4.5 and 4.6 show 2D radiation patterns corresponding to plots found in Figure 4.4 at the cut $\phi=0$ in linear and decibels scales respectively.

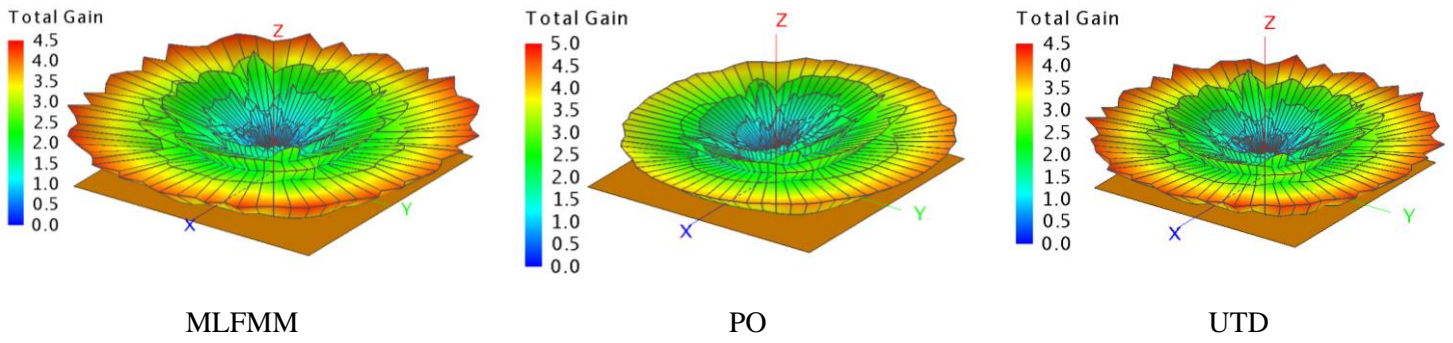


Figure 4.4 3D Radiation Pattern of a monopole on a $20\lambda \times 20\lambda$ square plate; linear scale

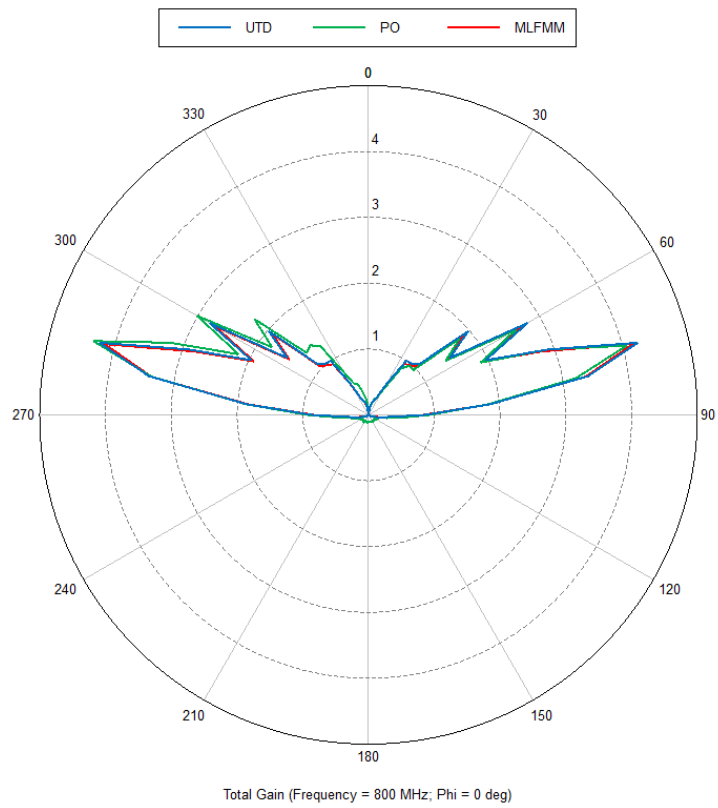


Figure 4.5 Comparison of radiation patterns in the far field at $\phi=0^\circ$ between MLFMM, PO and UTD for a monopole on a square plate $20\lambda \times 20\lambda$ at 800 MHz; linear scale

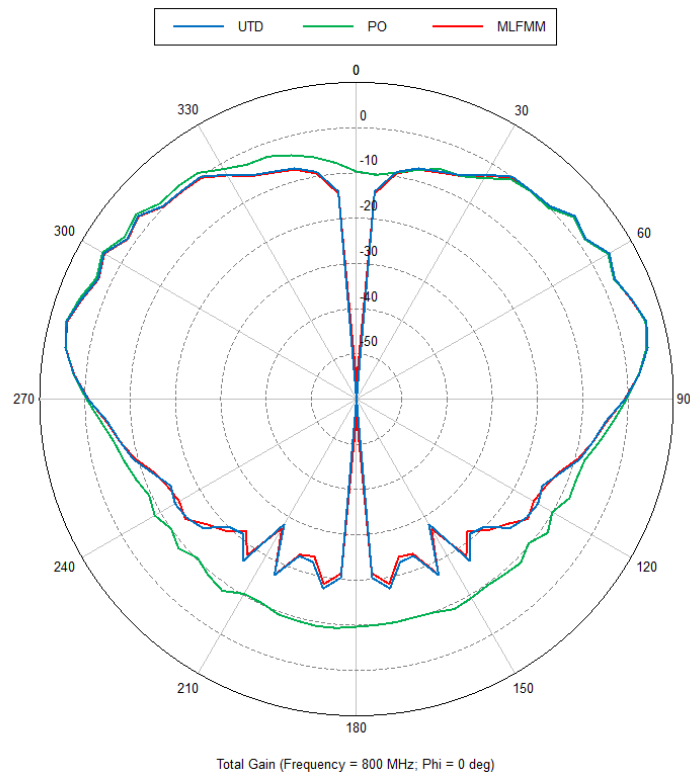


Figure 4.6 Comparison of radiation patterns in the far field at $\phi=0^\circ$ between MLFMM, PO and UTD for a monopole on a square plate $20\lambda \times 20\lambda$ at 800 MHz; dB scale

Similarly, from Figures 4.4 to 4.6, an excellent agreement between MLFMM and UTD can be seen with less than 0.2dB difference. For the UTD simulation settings all the options have been taken into account. The PO also shows worse performance as compared to MLFMM and UTD. The maximum difference reaches 16.5dB at $\theta=210$. In Figure 4.4, the 3D radiation pattern simulated with PO is tilted and not symmetrical. This should not be the case since the geometry of the antenna and the plate are symmetric.

The spikes in Figure 4.5 are more defined, sharper and rotated by about 10° . The most power is distributed closer the horizontal surface of the square plate compared to field distribution found in Figure 4.3.

Figures 4.7 illustrates 3D radiation patterns computed with MLFMM, PO and UTD for a square plate with edge of 20λ . Figures 4.8 and 4.9 show 2D radiation patterns corresponding to plots found in Figure 4.7 at the cut $\phi=0$ in linear and decibels scales respectively.

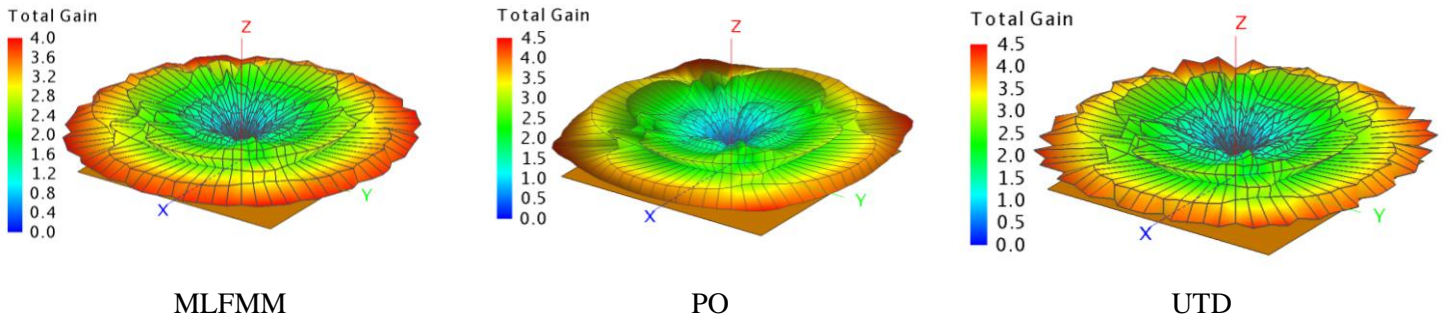


Figure 4.7 3D Radiation Pattern of a monopole on a $30\lambda \times 30\lambda$ square plate; linear scale

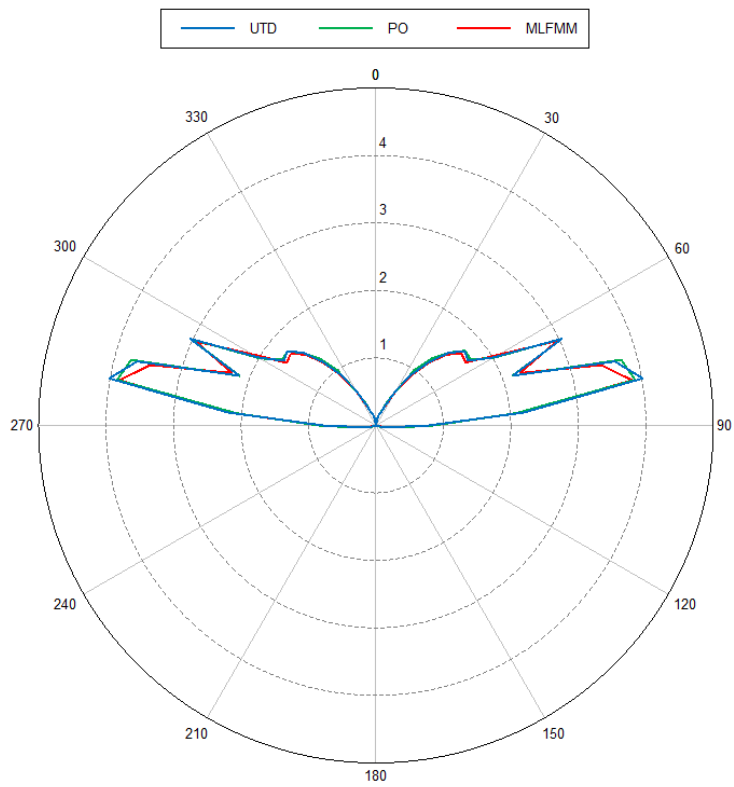


Figure 4.8 Comparison of radiation patterns in the far field at $\phi=0^\circ$ between MLFMM, PO and UTD for a monopole on a square plate $30\lambda \times 30\lambda$ at 800 MHz; linear scale

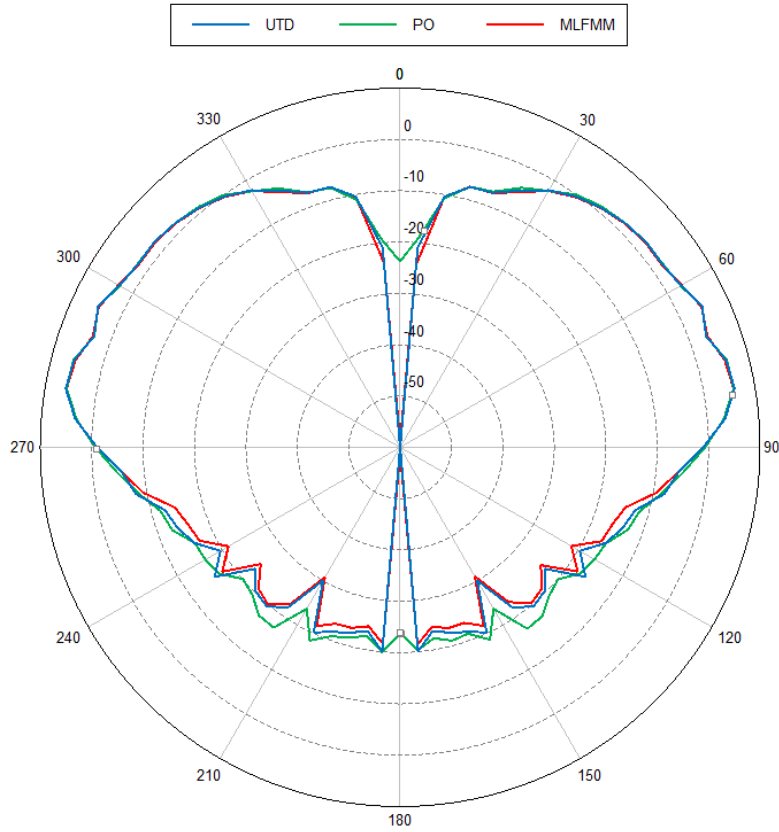


Figure 4.9 Comparison of radiation patterns in the far field at $\phi=0^\circ$ between MLFMM, PO and UTD for a monopole on a square plate $30\lambda \times 30\lambda$ at 800 MHz; dB scale

Finally, from Figures 4.7 to 4.9 it can be seen that all simulations result in an identical radiation pattern shape. UTD and MLFMM do not differ more than 0.9 dB. The maximum gain difference between PO and MLFMM is found at the angles $\theta=210^\circ$ and $\theta=150^\circ$. The difference is about 7 dB. The rest of the gain overlaps between all three methods.

Table 4.2 summarizes the performance of each simulation method in terms of Peak Memory, CPU Time and number of meshed segments.

Table 4.2 Performance Comparison between MLFMM, PO and UTD methods for different square plate sizes

Model	Solution Method	Peak Memory	CPU Time [s/hours]	Number of metallic edges	Number of Mesh (Antenna/ Plate)
Square Plate $10\lambda \times 10\lambda$	MLFMM+MLFMM	630.6 MByte	97.6 / 0.027	49 440	4 / 33 120
	MoM+PO	15.9 MByte	5.6 / 0.002	22 192	4 / 14 688
	MoM+UTD	177. 14 kByte	0.6 / 0.000	N.A.	4 / 1 (Polygonal Surface)
Square Plate $20\lambda \times 20\lambda$	MLFMM+MLFMM	2.5 GByte	435.4 / 0.121	198 630	4 / 132 740
	MoM+PO	34.7 MByte	36.1 / 0.010	88 724	4 / 58 936
	MoM+UTD	177.2 kByte	0.532 / 0.000	N.A.	4 / 1 (Polygonal Surface)

Square Plate 30λx30λ	MLFMM+ MLFMM	2.733 GByte	1399.2 / 0.389	447 567	4 / 298 858
	MoM+PO	85.1 MByte	113.5/ 0.032	199 578	4 / 132 732
	MoM+UTD	174.7 kByte	0.532 / 0.000	N.A.	4 / 1 (Polygonal Surface)

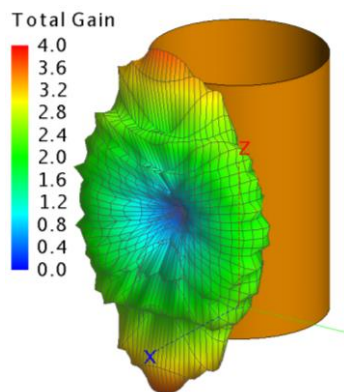
4.2 Cylinder

After simulating the far field radiation for a square plate, a more complex object is considered. The cylinder is constructed using three methods but the dimensions remain the same: a cylinder with a smooth surface, a cylinder approximated with 20 sided polygonal plates, a cylinder approximated with 30 sided polygonal plates. Table 4.3 summarizes all the parameters of the simulations.

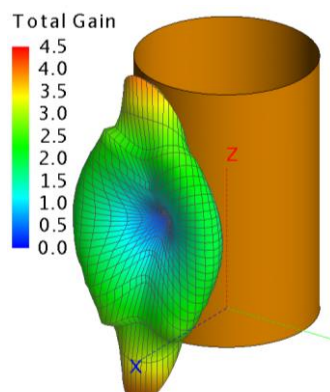
Table 4.3 Constant Parameters for all simulations for the cylinder geometries

Frequency	800 MHZ
Antenna Mesh Size	$\lambda/1000$
Radius	
Antenna Mesh Size: Length	Standard Mesh Size: $\lambda/12$
Antenna Type	Monopole
Antenna Length	$\lambda/4$
Cylinder Radius	2m = 5.3λ
Cylinder Length	6m = 16λ
Antenna Orientation	+X-axis

Figure 4.10 illustrates 3D radiation patterns computed with MLFMM, PO and UTD for a smooth curved surface. Figures 4.11 and 4.12 show 2D radiation patterns corresponding to plots found in Figure 4.10 at the cut $\phi=0$ in linear and decibel scales respectively.



MLFMM



PO

Error 17702: [Cylinder1.Face1](#) - Face is not allowed to be solved with UTD since it is not flat.
Error 17702: [Cylinder1.Face2](#) - Face is not allowed to be solved with UTD since all its edges are not straight.

UTD

Figure 4.10 3D Radiation Pattern of a monopole on a cylinder with a smooth circular surface; linear scale

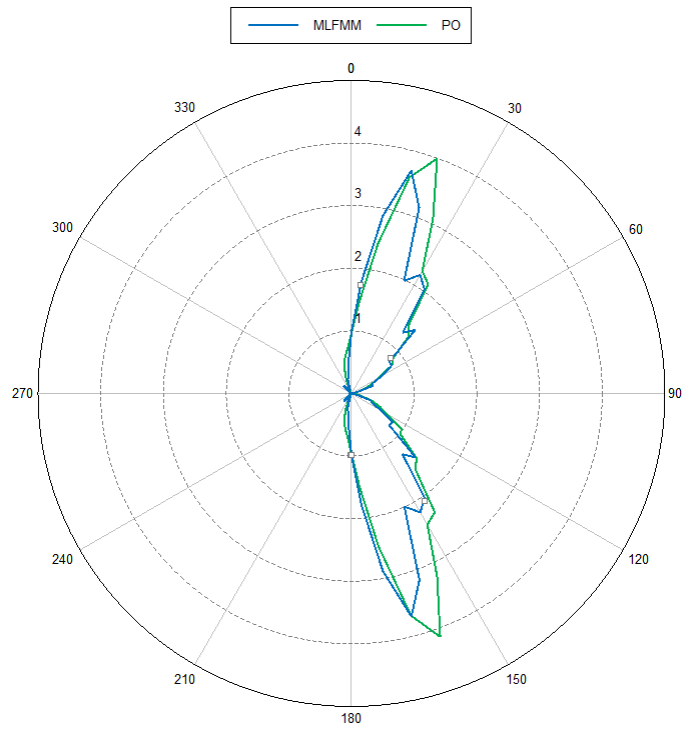


Figure 4.11 Comparison of radiation patterns in the far field at $\phi=0^\circ$ between MLFMM and PO for a monopole on a smooth cylinder at 800 MHz; linear scale

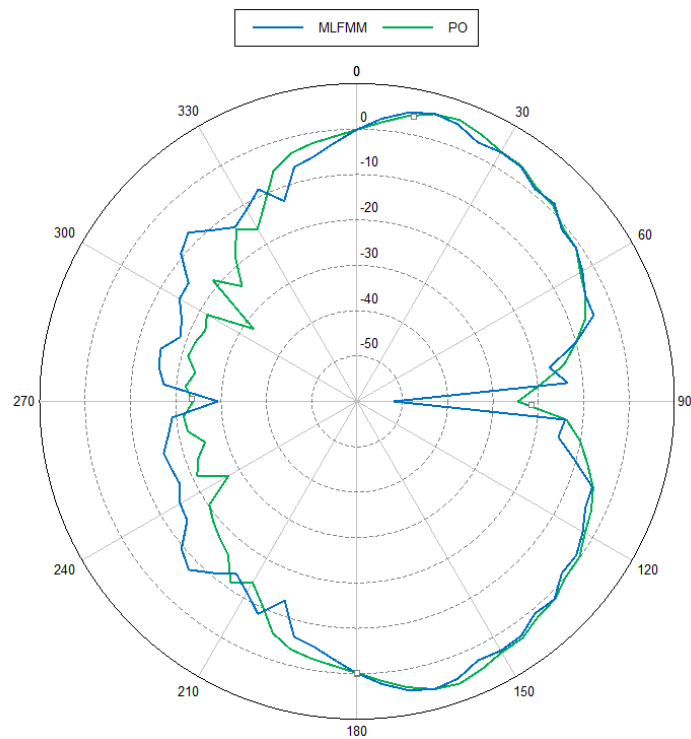


Figure 4.12 Comparison of radiation patterns in the far field at $\phi=0^\circ$ between MLFMM and PO for a monopole on a smooth cylinder at 800 MHz; dB scale

First of all, the radiation pattern in the far field cannot be simulated using UTD method, because CADFEKO gives an error 17702. The face of the smooth cylinder cannot be solved because the edges are not straight. This is one of the main limitations of the UTD method. All the surfaces must be approximated with flat polygonal plates with the edge dimension not larger than a wavelength. Secondly, the remaining methods MLFMM and PO give a similar shape of the radiation pattern. The maximum power is re-radiated at the edges of the cylinder creating maximum peaks of about 4dB gain in positive and negative z-directions. Finally, the PO methods gives a smoother radiation pattern, whereas the MLFMM method includes more lobes. In Figure 4.12, it can be seen that the two methods overlap from $\theta=0^\circ$ to 180° . However the discrepancies increase from $\theta=180^\circ$ to 360° with an average value of 3dB.

Figure 4.13 illustrates 3D radiation patterns computed with MLFMM, PO and UTD for a cylinder approximated with 20 polygonal plates. Figures 4.14 and 4.15 show 2D radiation patterns corresponding to plots found in Figure 4.13 at the cut $\phi=0$ in linear and decibels scales respectively.

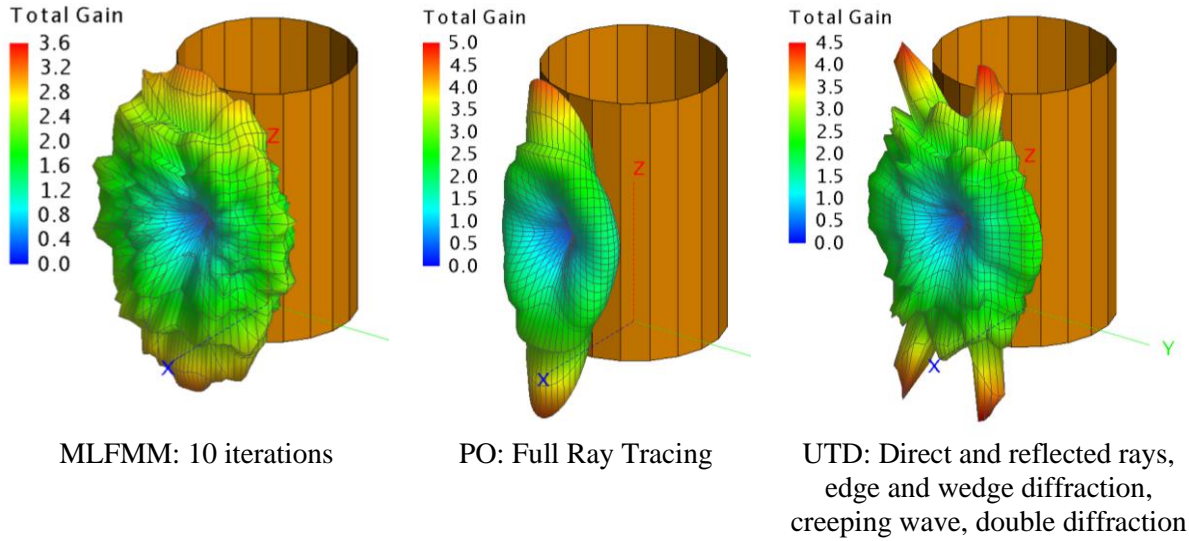


Figure 4.13 3D Radiation Pattern of a monopole on a cylinder with 20 polygons; linear scale

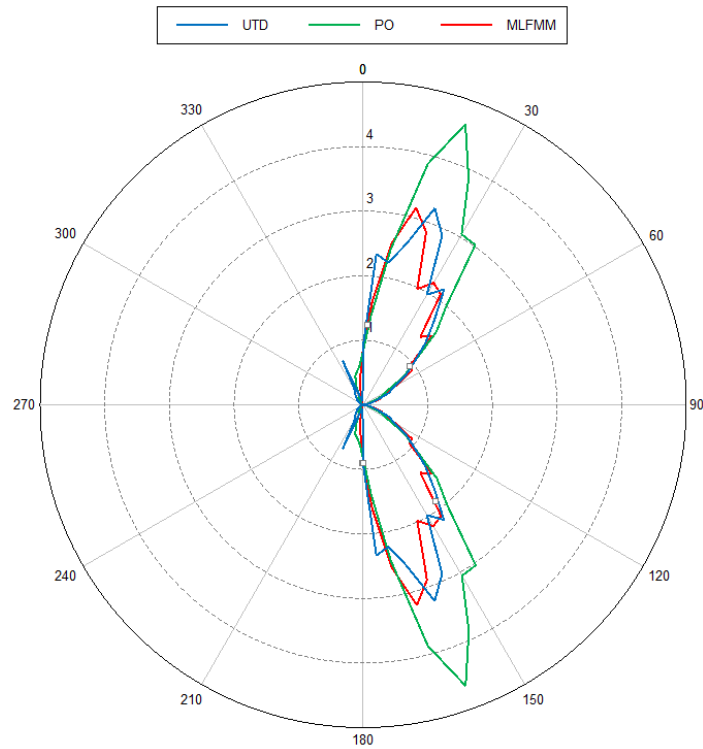


Figure 4.14 Comparison of radiation patterns in the far field at $\phi=0^\circ$ between MLFMM, PO and UTD for a monopole on a cylinder made of 20 plates at 800 MHz; linear scale

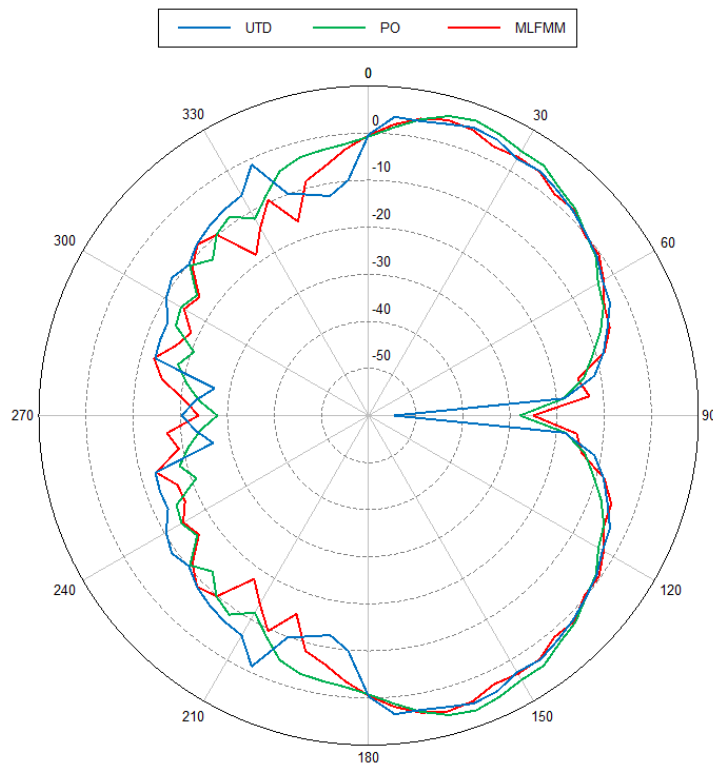


Figure 4.15 Comparison of radiation patterns in the far field at $\phi=0^\circ$ between MLFMM, PO and UTD for a monopole on a cylinder made of 20 plates at 800 MHz; dB scale

The radiation pattern simulated with UTD method mostly overlaps with the radiation pattern simulated using MLFMM method. However, the UTD method has 4 main spikes at the top and the bottom of the cylinder compared to 2 main spikes that are simulated with MLFMM and PO methods. The radiation pattern calculated using PO gives the largest gain value at the peaks with 5dB, versus MLFMM's 3.6 dB and UTD's 4.5dB. The side lobes match well between UTD and MLFMM, and the PO shows smooth, evenly distributed pattern as can be seen in Figure 4.13. In Figure 4.12, it can be seen that all three methods overlap from $\theta=0^\circ$ to 180° . However the discrepancies increase from $\theta=180^\circ$ to 360° with an average value of 2dB.

Figure 4.16 illustrates 3D radiation patterns computed with MLFMM, PO and UTD for a cylinder with 30 polygonal plates. Figures 4.17 and 4.18 show 2D radiation patterns corresponding to plots found in Figure 4.16 at the cut $\phi=0$ in linear and decibels scales respectively.

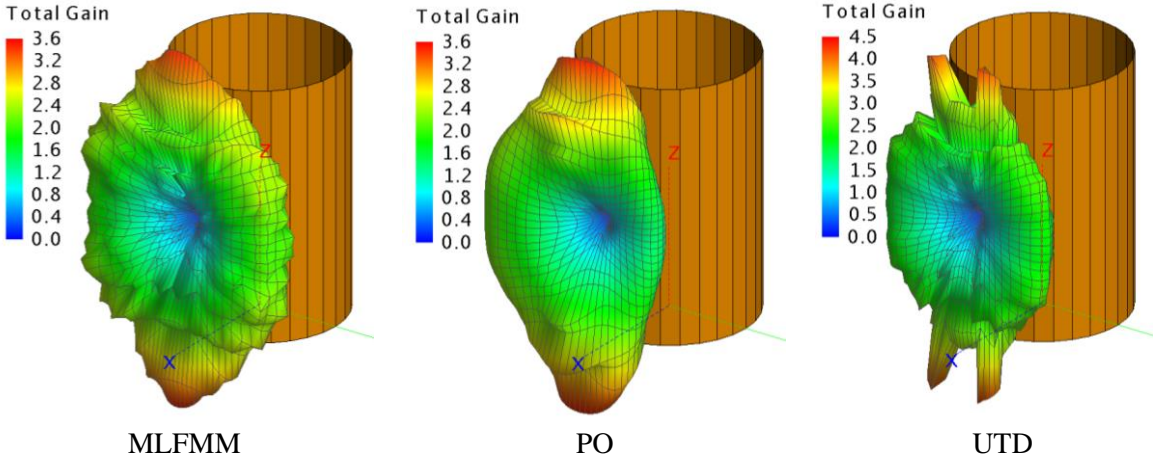


Figure 4.16 3D Radiation Pattern of a monopole on a cylinder with 30 polygons; linear scale

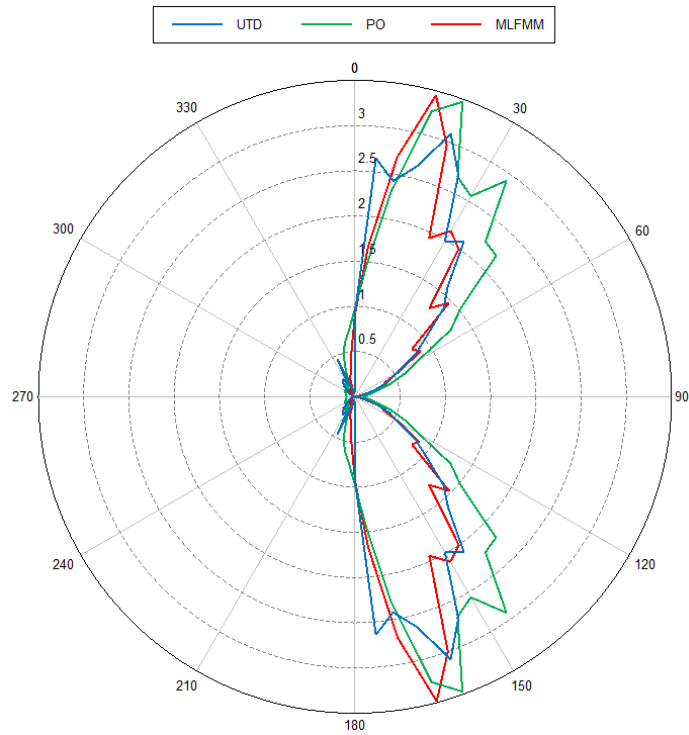


Figure 4.17 Comparison of radiation patterns in the far field at $\phi=0^\circ$ between MLFMM, PO and UTD for a monopole on a cylinder made of 20 plates at 800 MHz; a linear scale

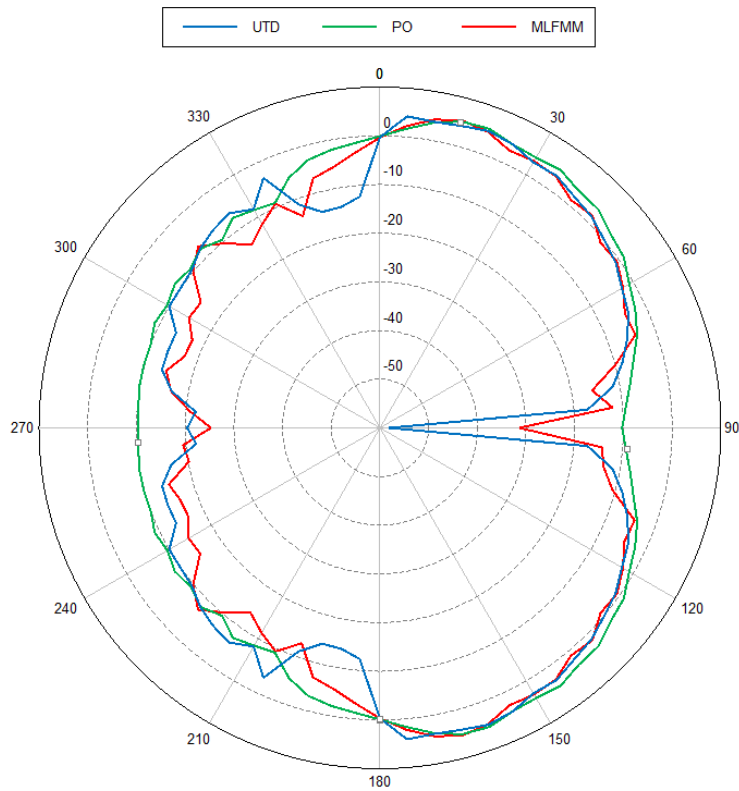


Figure 4.18 Comparison of radiation patterns in the far field at $\phi=0^\circ$ between MLFMM, PO and UTD for a monopole on a cylinder made of 20 plates at 800 MHz; dB scale

The results of the simulations for cylinder approximated with 30 polygonal plates are similar to the results derived for a cylinder that is approximated with 20 polygonal plates. Again, the radiation pattern simulated with UTD method mostly overlaps with the radiation pattern simulated using MLFMM method. However, the UTD method has 4 main spikes at the top and the bottom of the cylinder compared to 2 main spikes that are simulated with MLFMM and PO methods. The radiation pattern calculated using PO gives the same gain value at the peaks as MLFMM method with 3.6dB, and the peak gain value using UTD method is 4.5dB. Similarly, the side lobes match well between UTD and MLFMM, and the PO shows smooth pattern without significant side lobes as can be seen in Figure 4.16. However, the radiation pattern using PO is not symmetric which is not expected, since the geometry of the cylinder and the placement of the antenna suggest that the results should have more symmetrical far field shape. In Figure 4.18, it can be seen that the total gain estimated with MLFMM and UTD methods overlap from $\theta=0^\circ$ to 180° . However the discrepancies increase from $\theta=180^\circ$ to 360° with an average value of about 2dB. The maximum difference between PO and MLFMM is found at $\theta=270^\circ$ where the gain difference is 14.5 dB.

Table 4.4 summarizes the performance of each simulation method in terms of Peak Memory, CPU Time and number of meshed segments.

Table 4.4 Performance Comparison between MLFMM, PO and UTD methods for different Cylinder geometries

Model	Solution Method	Peak Memory	CPU Time [s/hours]	Number of metallic edges	Number of Mesh (Antenna/Plate)
Smooth Cylinder	MLFMM+MLFMM	1.94 GByte	963.1 / 0.268	267 563	4 / 178 644
	MoM+PO	55.0 MByte	17.7 / 0.005	119 056	4 / 79 192
	MoM+UTD	N.A.	N.A.	N.A.	Error 17702: Cylinder Surface is not allowed to be Solved since it is not flat
Cylinder approximated with 20 polygons	MLFMM+MLFMM	1.89 GByte	935.4 / 0.260	264 020	4 / 176 280
	MoM+PO	65.72 MByte	21.2 / 0.006	121 880	4 / 81 080
	MoM+UTD	484.36 kByte	257.2 / 0.071	N.A.	4 / 20 (Polygonal Surface)
Cylinder approximated with 30 polygons	MLFMM+MLFMM	1.96 GByte	903.0/0.251	274 200	4 / 183 060
	MoM+PO	63.8 MByte	18.1 / 0.005	115 470	4 / 76 800
	MoM+UTD	828.8 kByte	873.8 / 0.243	N.A.	4 / 30 (Polygonal Surface)

From Table 4.4 it can be seen that UTD has the smallest peak memory of 0.8Mbyte, compared to PO's 63.8MByte and MLFMM's 1 960 Mbyte. However in terms of CPU, PO provides fastest results. The number of mesh segments of the cylinder simulated with PO is also smaller than using MLFMM method.

4.3 UTD Settings

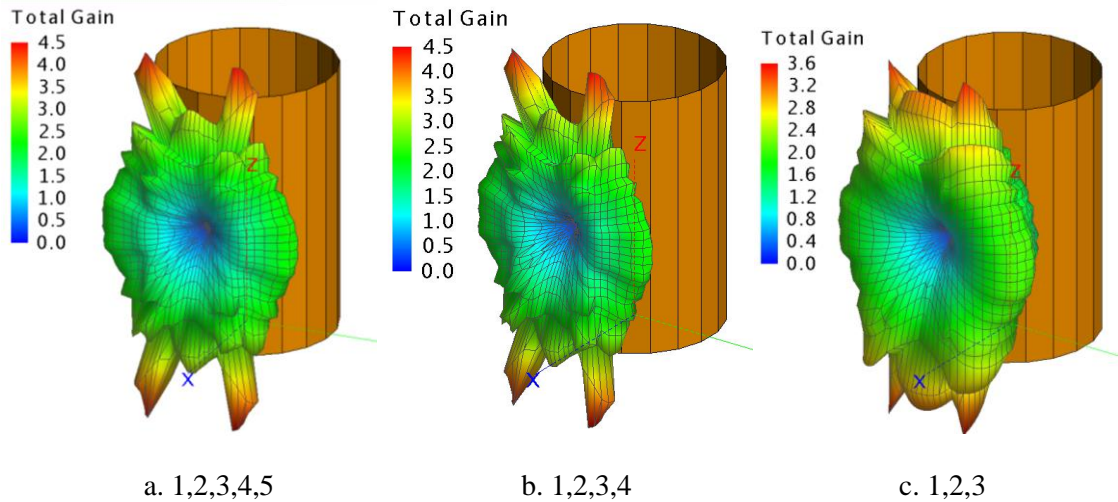
In order to calculate the radiation patterns for a square plate and a cylinder using the UTD method, all possible setting parameters were used in order to account for all the possible physical phenomena. However, this might not necessarily lead to the correct results. Although for the square plate including all the setting parameters resulted in practically perfect match between MLFMM and UTD, for the cylinder the radiation patterns did not have identical peaks at the top and bottom of the cylinder, regardless of the geometry approximations.

Table 4.5 shows all the possible setting parameters which can be included or excluded for calculation of the radiation patterns.

Table 4.5 Parameter settings for UTD solver

1	Direct and Reflected Rays
2	Edge and Wedge Diffraction
3	Corner Diffraction
4	Double Diffraction
5	Creeping Wave

Figure 4.19 shows radiation patterns using UTD method with possible combinations that correspond to parameter settings in Table 4.5.



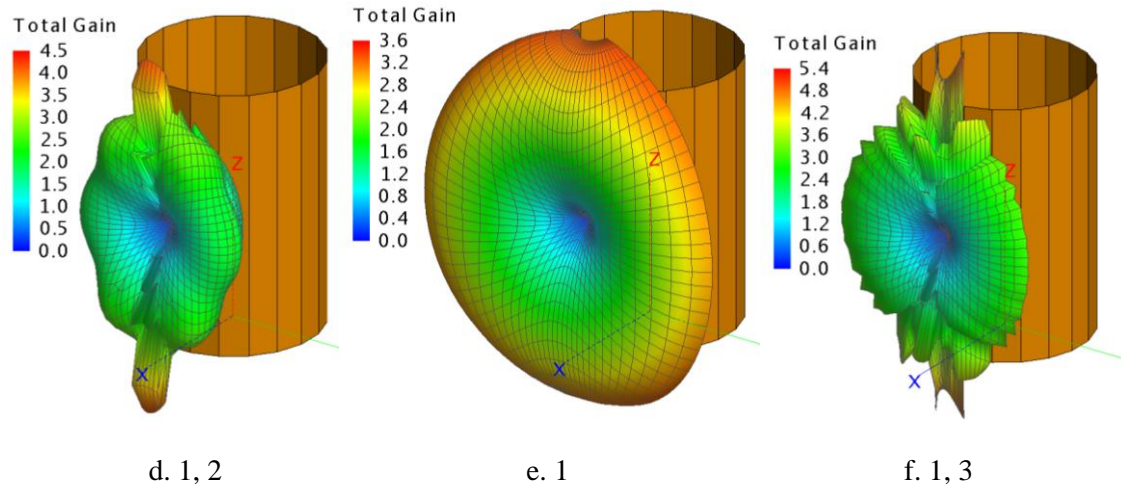


Figure 4.19 Comparing UTD methods with different settings: Direct and reflected rays, edge and wedge diffraction, corner diffraction, Double diffraction, creeping wave; linear scale

From Figure 4.19 it can be seen that the radiation pattern changes significantly depending on the parameter settings. Option d, which includes direct and reflected rays as well as edge and wedge diffraction, gives the radiation pattern that resembles closely the radiation pattern that is estimated using PO method in Figure 4.13 however it does not include the side lobes. From the user's perspective it is not clear where the two peaks originate from and which parameter settings should be included.

It was also important to estimate how the approximation of the geometry using flat plates has affected the radiation pattern for the cylinder. Figure 4.20 shows the radiation pattern simulated with MLFMM method for a cylinder with smooth surface, approximated with 20 polyinal plates and 30 p0olygonal plates. From this Figure 4.20 it can be seen that the only significant difference occurs at $\theta=90^\circ$ where no power is actually radiated because the monopole is oriented along x-axis at $\theta=90^\circ$.

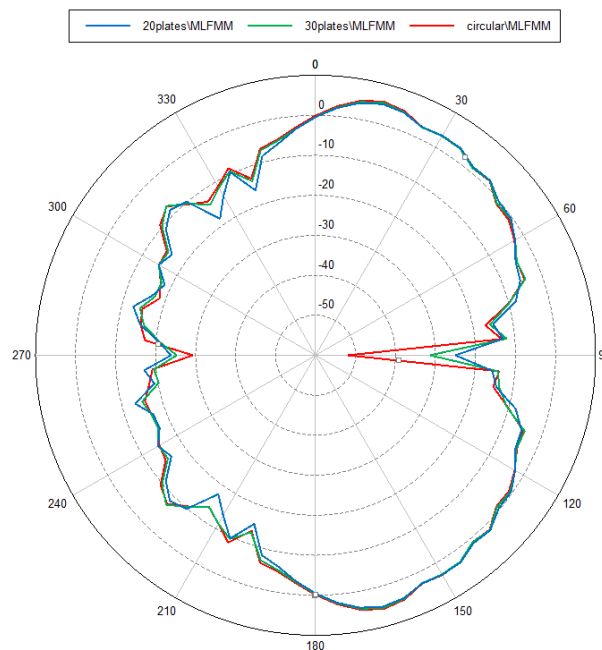


Figure 4.20 Radiation Pattern of a cylinder with smooth surface and surface approximated with $n=20$, $n=30$ sides; dB Scale

Another important comparison is illustrated in Figure 4.21. Here the radiation pattern is compared for a smooth cylinder using PO and MLFMM methods versus UTD method for a cylinder approximated with 30 polygonal plates.

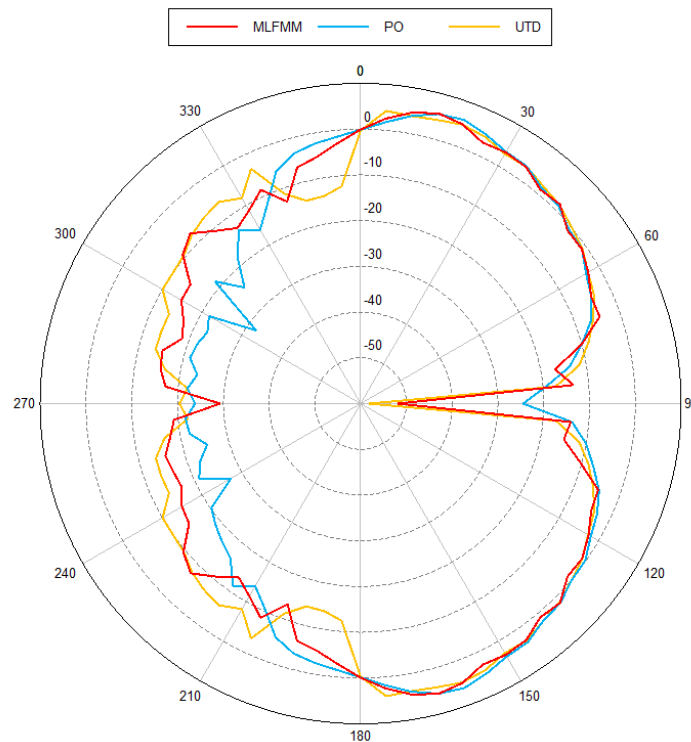


Figure 4.21 Radiation Pattern of a cylinder with smooth surface computed with MLFMM and PO versus radiation pattern of a cylinder simulated with UTD with $n=30$ plates; dB Scale

From Figure 4.21 it can be seen that the total gain estimated with all three methods overlaps from $\theta=0^\circ$ to 180° . The total gain difference between MLFMM and UTD method averages around 1.5 dB in the $\theta=180^\circ$ to 360° range, and 5dB difference between MLFMM and PO.

4.4 Conclusion

Based on the feasibility analysis it can be seen that for simple geometries the radiation patterns simulated with different methods produce similar results. For the square plate the UTD and MLFMM gave almost perfectly matching patterns, whereas the PO deviated by 16.5dB at $\theta=210^\circ$ for a square plate with the edge length 20λ .

For a slightly more complex structure the differences between the methods are more significant. The UTD method included all the possible parameter settings, however it included 4 peaks which were not observed in radiation patterns simulated with MLFMM and PO.

Based on the output file in POSTFEKO, the PO methods requires significantly lower CPU time however it results in rough approximations of the radiation pattern. MLFMM requires the most CPU time and peak memory however the results take into account more side lobes and more consistency between different geometries is observed.

Although UTD method has some drawbacks namely, it requires flat plated geometry input thus the curvilinear surfaces cannot be implemented, it calculates the radiation pattern accurately and requires significantly lower computational resources. Therefore it will be used for the further analysis in Chapter 6 in estimating the optimum position for the antenna system. The MLFMM method will be used for verification purposes to check the results of UTD method.

Chapter 5 Aircraft Geometry Approximation

In this Chapter selection of the aircraft type is made and necessary approximations of the aircraft model are explained. The structural elements of the aircraft are divided into primary, secondary and tertiary scattering bodies.

5.1 Aircraft Selection

The most common commercial aircraft that is purchased by the airlines globally is Boeing 737 [38]. There are a number of sub-categories of that aircraft namely, Boeing 737 -600, -700, -800 and -900 also known as Next Generation Series. These sub-models do not significantly deviate from each other by structural design, so the more common type -800 is selected. Table 5.1 summarizes the most important geometrical dimensions of Boeing 737 -800 aircraft. (Note that due to a lack of available data for certain geometrical parameters, the dimensions were estimated from a technical sketch of the aircraft using a ruler and appropriately scaling the parameters).

Table 5.1 Boeing 737-800 Geometric Parameters

Main Body			Horizontal Stabilizer		
		Units			Units
Aircraft Length	39.5	m	Span	14.35	m
Fuselage Length	38.08	m	Aspect Ratio	6.16	-
Height	4.01	m	Taper Ratio	0.203	-
Width	3.76	m	Dihedral	7	°
Fineness Ratio	10.21	-	¼ Chord Sweep	30	°
Wing			Vertical Stabilizer		
		Units			
Span	34.32	m	Height	7.16	m
Root Chord	5.709	m	Aspect Ratio	1.91	-
Tip Chord	1.25	m	Taper Ratio	0.271	-
¼ Chord Sweep	25	°	¼ Chord Sweep	35	°

Figure 5.1 shows the technical drawing and specification data of Boeing 737-800.

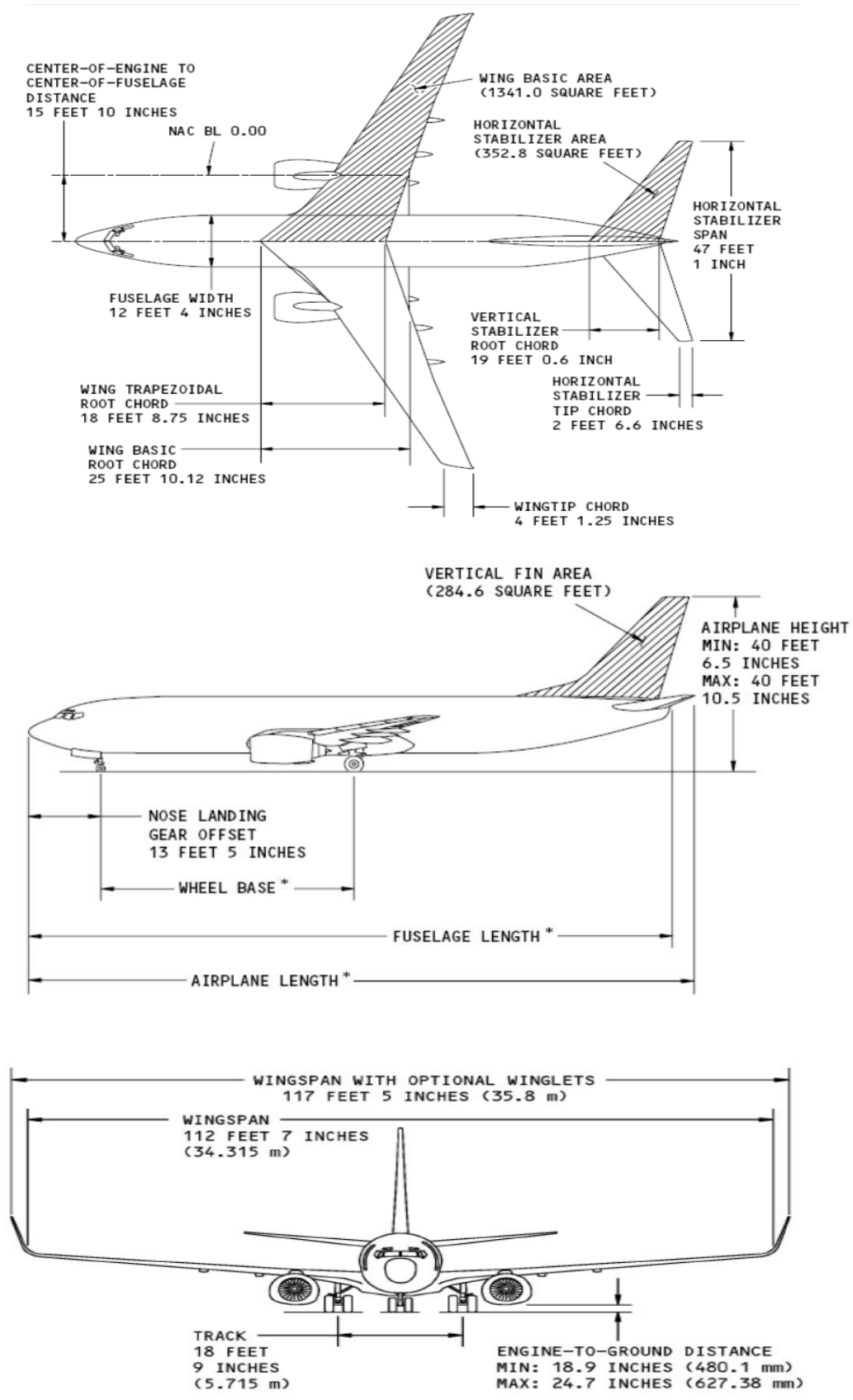


Figure 5.1 Technical Drawing and Specification Data of Boeing 737 (Next Generation) [39]

5.2 Aircraft Model Approximations

The aircraft is made of several structural elements and in order to be able to simulate the antenna's radiation pattern in a simulating platform, the approximations of each element have to be introduced.

Fuselage

In Chapter 4 after performing a feasibility analysis, the UTD method has been selected as the simulating method for estimating the radiation pattern. This implies that the UTD method will further introduce necessary approximations. Namely, the material that can be simulated can only be metallic and all the surfaces are designed as flat plates.

Since the fuselage is the main and primary scattering element in the aircraft, the most significant analysis is presented in this section. There are several ways that the fuselage can be approximated with flat plates. This depends on the number of the plates and the angle with which a circle can be approximated. There is also a limiting case for this approximation because using a UTD method the minimal edge length in a design cannot be larger than 1.2 wavelength. Another important approximation is that the fuselage in the cross section is slightly elliptical rather than circular shaped. The aspect ratio between the major axis and the minor axis is 1.06 and for the further investigation is neglected. So the fuselage is approximated with a circular cross-section.

Figure 5.2 and 5.3 show suggested geometries for the fuselage approximation. 4 geometries are considered with the following parameters:

- 8 plates, constant $\Delta\theta = 45^\circ$
- 12 plates, constant $\Delta\theta = 30^\circ$
- 21 plates, constant $\Delta\theta = 17^\circ$
- 14 plates, varying $\Delta\theta = 17^\circ, 18^\circ, 20^\circ, 22^\circ, 27^\circ, 45^\circ$

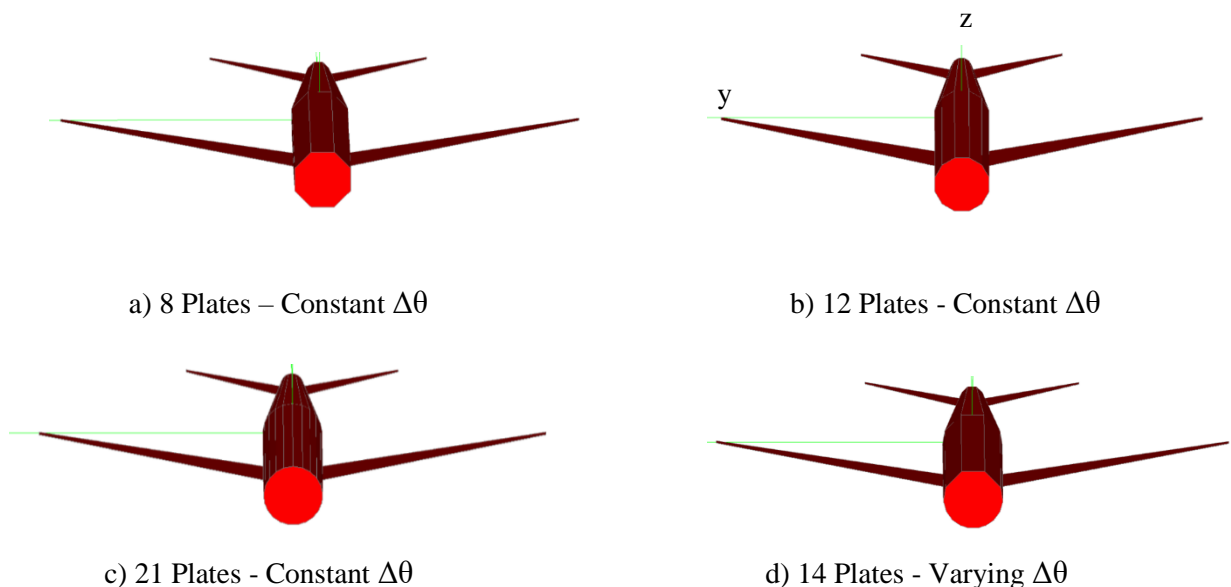


Figure 5.2 Geometrical approximation of the fuselage with different number of plates at $\phi = 90^\circ$

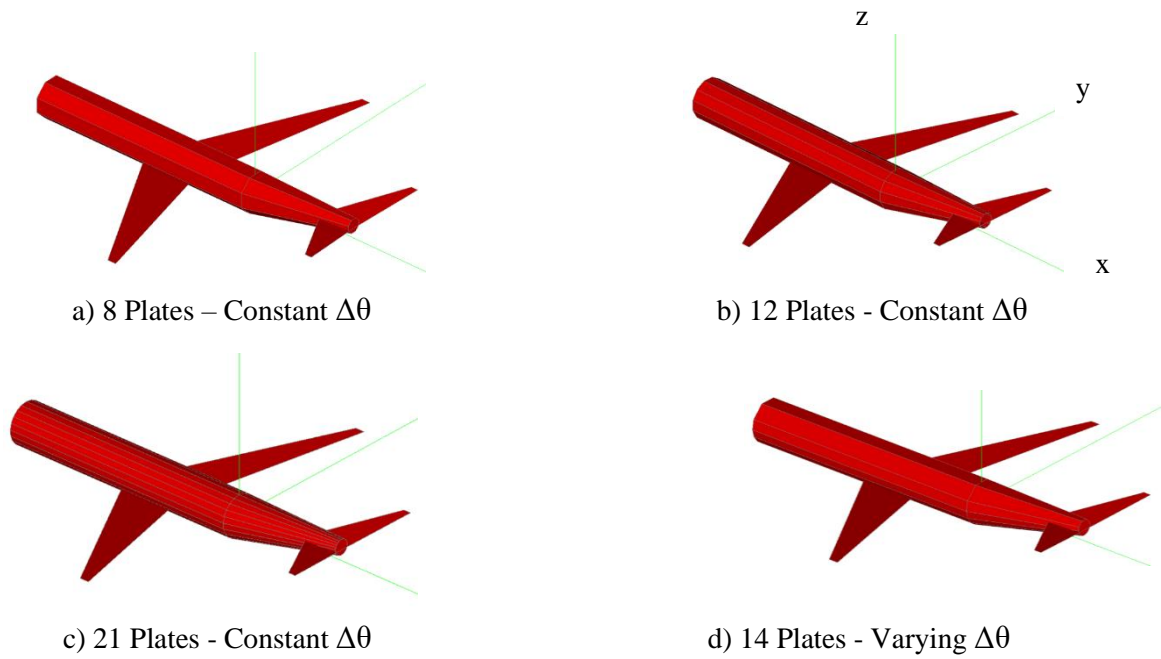


Figure 5.3 Geometrical approximation of the fuselage with different number of plates at $\phi = 45^\circ$

In order to select an appropriate model, the radiation pattern is estimated and presented in Figures 5.4 and 5.5 at different cuts.

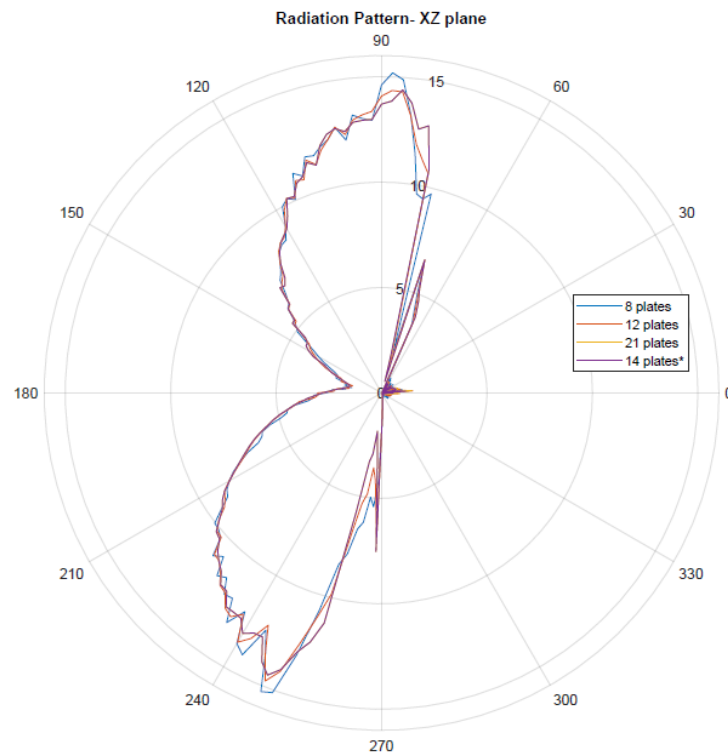


Figure 5.4 Radiation Pattern [Electric Field] in XZ plane of a monopole at 1.5 GHz at the lower side at the tail of the aircraft using different approximation geometries for the fuselage: 8 plates, 12 plates, 21 plates and 14 plates.

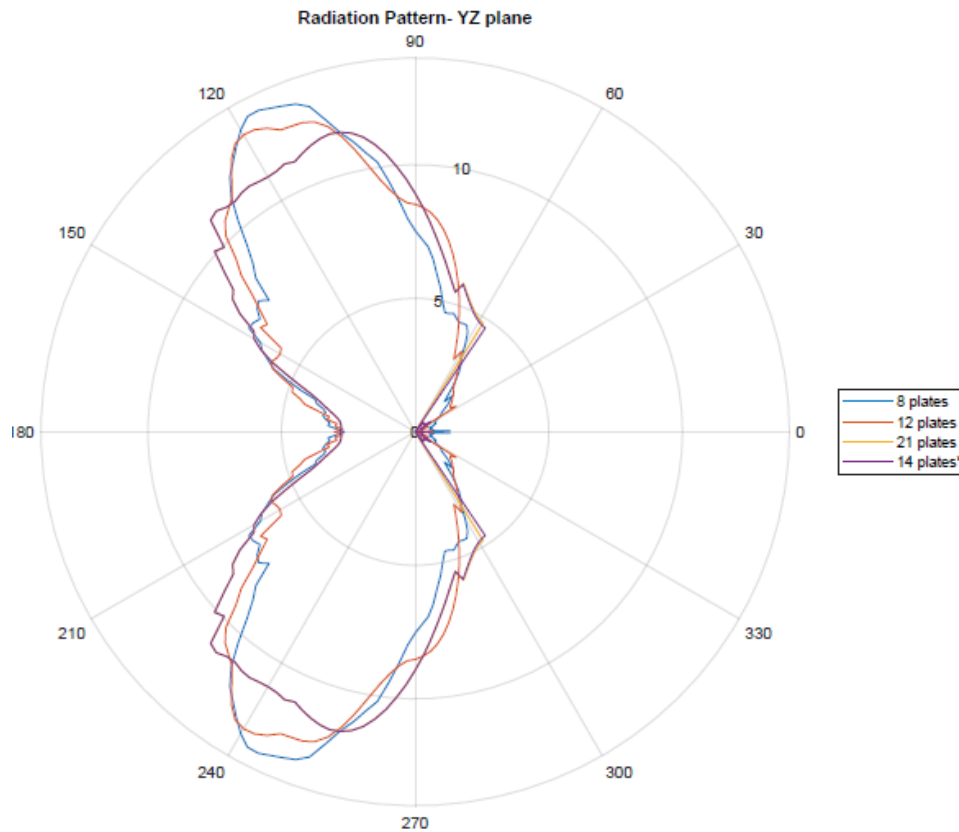


Figure 5.5 Radiation Pattern [Electric Field] in YZ plane of a monopole at 1.5 GHz at the lower side at the tail of the aircraft using different approximation geometries for the fuselage: 8 plates, 12 plates, 21 plates and 14 plates.

In Figure 5.4 it can be seen that all radiation patterns for different number of plates have a strong overall. The largest difference found at $\theta=91^\circ$ between all the geometries is as follows:

- 8 plates, constant θ $\Delta=8.6\%$
- 12 plates, constant θ $\Delta=3\%$
- 14 plates, varying θ $\Delta=0.1\%$

The comparison is made with 21 plates as this geometry provides the limiting case and number of plates approximating the fuselage can not be further increased.

In Figure 5.5 however the difference in values of the electric field is significantly higher. The largest difference found at $\theta=115^\circ$ between all the geometries is as follows:

- 8 plates, constant θ $\Delta=20\%$
- 12 plates, constant θ $\Delta=14\%$
- 14 plates, varying θ $\Delta=1\%$

Similarly, the comparison is made with respect to the fuselage approximated with 21 plates.

Table 5.2 summarizes the computational resources for different fuselage approximations.

Table 5.2 Computational Comparison Between different number of plate approximations for the fuselage

	8 plates	12 plates	21 plates	14 plates (varying $\Delta\theta$)
CPU Time [Sec]	257.2	472.8	1 104.3	634.6
Peak Memory [kBytes]	288.5	510.8	1200	656.9
Total number of Ray Paths	427 571	394 032	450 537	452 172
Unutilized UTD Rays (due to distance between two points being too small)	20	4	38	38

From Table 5.2 it can be seen that fuselage approximated with 8 plates has the lowest CPU Time and requires the the least memory however as seen from Figure 5.5 it deviates from the 21 plated fuselage in terms of the radiation pattern the most. 14 plated fuselage performs the closest to the 21 plated fuselage in terms of the radiation pattern and it has reasonable computational performance. However the problem with this model is that it is not uniform. In case the antenna system is only analyzed in the lower part of the aircraft, this model will suffice, however it will not be considered for the analysis of the research question because different locations of the antenna system will be examined including top surface of the fuselage of the aircraft. Therefore the fuselage with 12 plates will be chosen for the further simulations. It has near to the optimum computational performance and deviates from the 21 plated fuselage by only 3% in terms of the radiation pattern.

Wings, Horizontal Stabilizer and Vertical Fin

The secondary scattering elements of the aircraft are wings, horizontal stabilizer and the vertical fin. Figure 5.6 illustrates the wings with 3D approximation and 2D flat plane approximation.

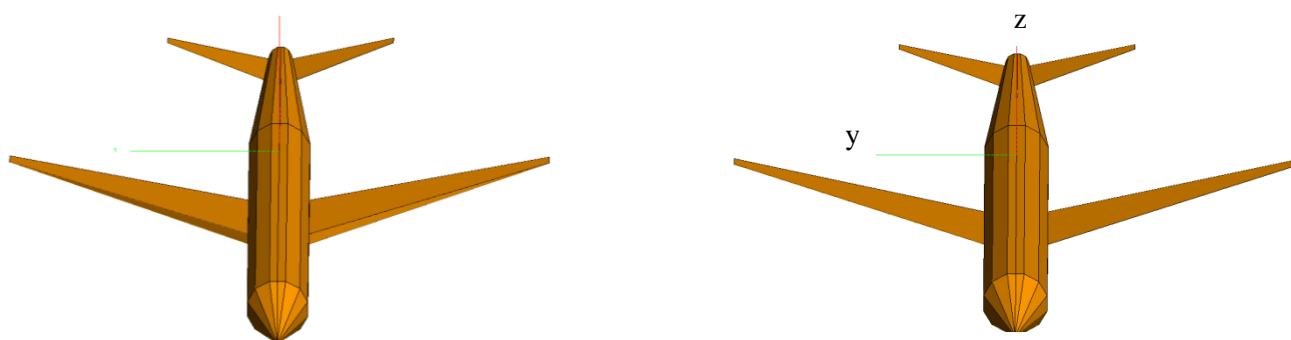


Figure 5.6 Geometrical approximation of the wings with 3D and 2D model on the left and right respectively

Figure 5.7 shows the far field radiation pattern of the 3D and 2D wing model and Figure 5.8 shows the adiation pattern at $\phi=135^\circ$ in polar coordinates.

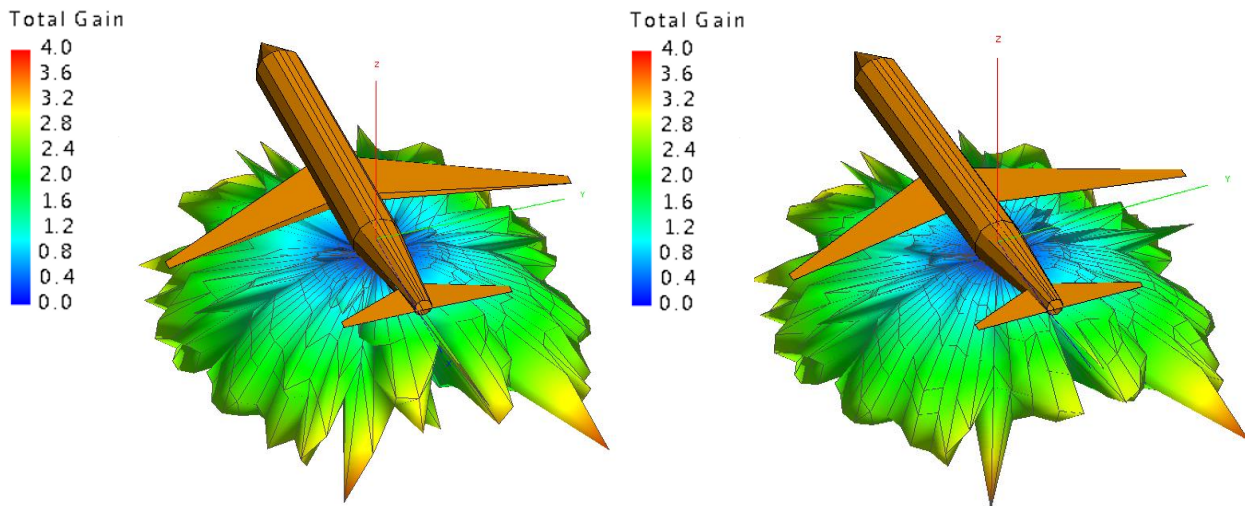


Figure 5.7 Radiation Pattern [Total Gain, linear scale] of a monopole at 1.575 GHz at the lower side at the tail of the aircraft using 3D wing and 2D wing approximations on the left and right respectively

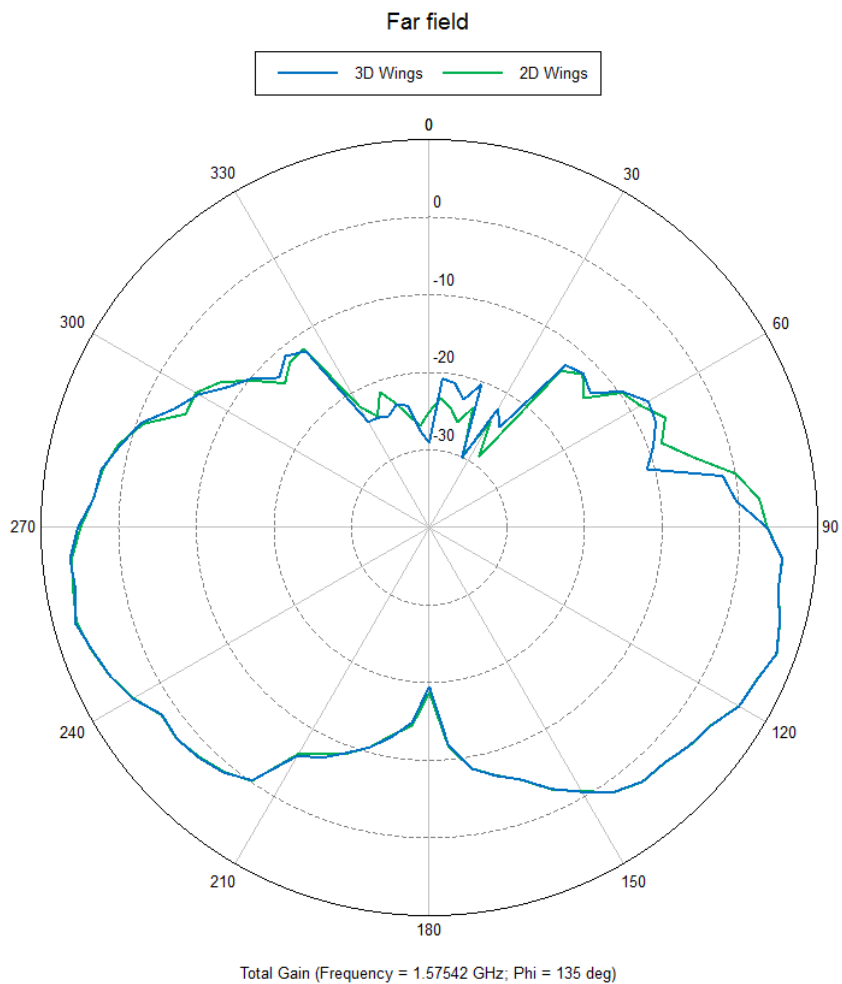


Figure 5.8 Radiation Pattern [Total Gain, dB] at $\phi=135^\circ$ of a monopole at 1.575 GHz at the lower side at the tail of the aircraft using 3D wing and 2D wing approximations respectively

From Figures 5.7 and 5.8 it can be seen that there is a strong overlap of the gain in the far field between the 3D and 2D models. On average the difference between the 2 approximations is not larger than 0.1 dB.

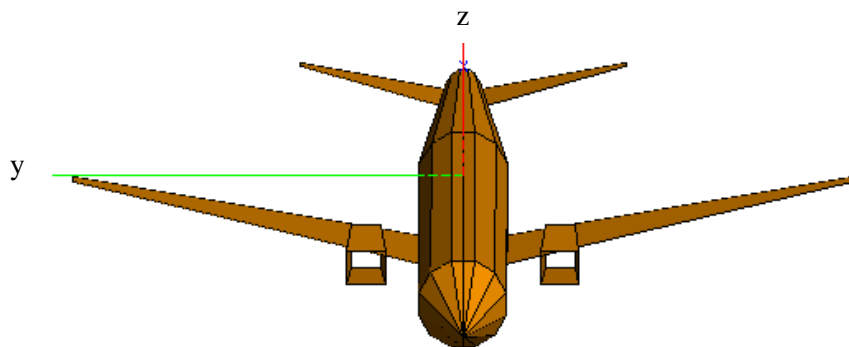
Since the results of the radiation pattern have a strong match, it is sufficient for further analysis to use the 2D model for the wings, the horizontal stabilizer and the vertical fin.

Engines, Nose and the Landing Gears

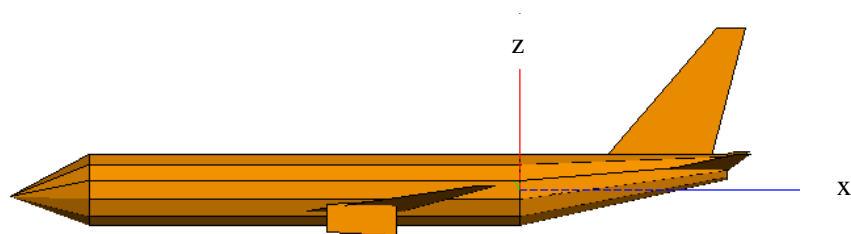
The tertiary scattering elements of the aircraft are the engines, nose and the landing gear. The engines are approximated with a hollow parallelepiped. The nose is approximated with a 12 edged prism. This logically follows from determining the design of the fuselage. And the landing gears are not taken into account since they are retracted during the flight and are only extended during landing and take-off. The antenna system is expected to operate in the cruising phase during the flight.

Final Aircraft Geometry Approximation

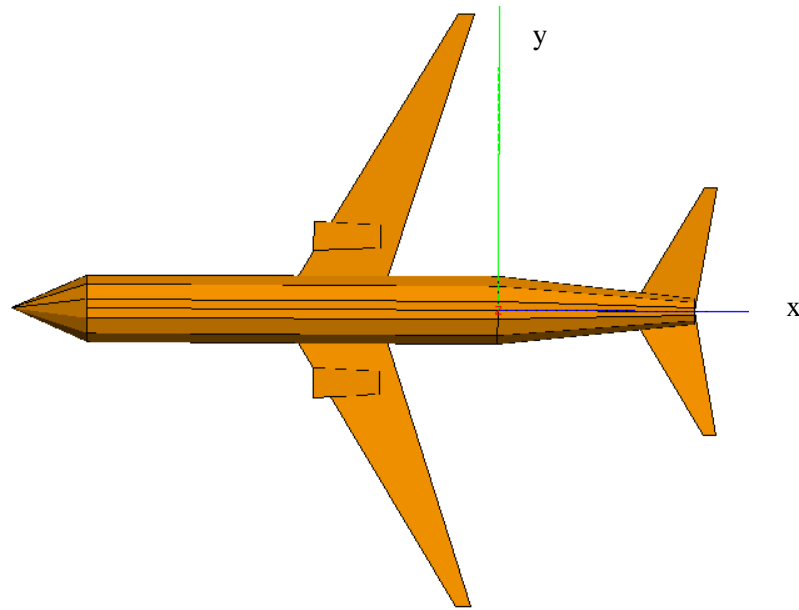
Figure 5.9 shows the final design of the aircraft that will be used to answer the main research question. Since the antenna system will be placed at different positions of the aircraft, the designed model includes all the main structural elements that act as primary, secondary and tertiary scattering bodies.



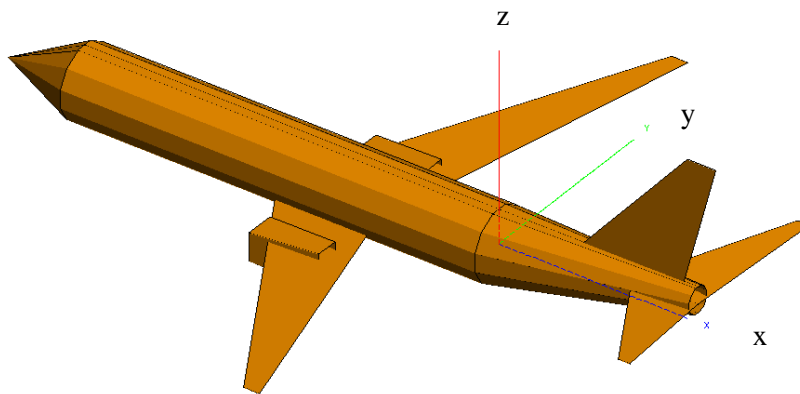
a. Front View of the Aircraft Model



b. Side view of the Aircraft Model



c. Top view of the Aircraft Model



d. Isometric View of the Aircraft Model

Figure 5.9 Final Model of the Boeing 737 Aircraft Geometry Approximation in front,side, top and isometric views respectively

5.3 Conclusion

In order to estimate the radiation patterns properly, there are number of approximations that have to be introduced for converting a real life model of the aircraft to a model that will be analyzed by the FEKO solver.

After performing a feasibility analysis, the UTD method has been selected as the simulating method for estimating the radiation pattern. This implies that the UTD method will further introduce necessary approximations. Namely, the material that can be simulated can only be metallic and all the surfaces are designed as flat plates. This affects the design of all the structural elements of the aircraft.

There is a limiting case for the approximation of a fuselage with flat plates because using a UTD method the minimal edge length in a model cannot be larger than 1.2 wavelength. This resulted in a fuselage constructed with 21 plates with constant edge length. The fuselage with 12 plates is chosen for the further simulations because it has near to the optimum computational performance and deviates from the 21 plated fuselage by only 3% in terms of the radiation pattern.

The wings, horizontal stabilizer and the vertical fin are modeled as 2D flat surface, since the results of the radiation pattern have a strong match between 3D and 2D models and differ on average not more than 0.1 dB.

Chapter 6 Results

The following Chapter describes optimization of the multiband antenna system placement on the approximated aircraft model. It also presents additional results of the independent verification simulation by using full-wave simulation solver.

6.1 Selection of the Antenna System Locations

In order to efficiently estimate the optimum position of the multiband antenna system on the aircraft it is important to identify preliminary locations where the antenna system can and cannot be placed.

In Chapter 1 it was shown that the aircraft already includes many antennas operating at different frequencies. Given the selection of the antennas, the top and sides of the aircraft are not suitable for the analysis because the patch antenna operating at the GSM frequency has to be directed towards the ground. Also, it is strongly recommended to place the antenna system along the $Y=0$ axis to ensure symmetric aerodynamic force distributions on the aircraft during the flight. The bottom middle section of the aircraft is not feasible for antenna placement due to retractable main landing gears. Also the main wings have a strong influence on the GPS link and will limit the radiation pattern towards the satellites for the monopole. Similarly, at the front part of the aircraft near the nose, the antennas cannot be placed due to the smaller nose landing gear. The areas of interest include the space between the nose and the main landing gears as well as the conical tail section of the aircraft. As the radius decreases towards the tip of the tail, the creeping wave has a stronger influence on the radiation pattern allowing more power to radiate upwards towards the satellites.

The Figure 6.1 illustrates the chosen antenna locations that potentially have the largest probability of satisfying the requirements and reaching both ground base stations and satellites with the given antenna set-up. The $x-z$ axis shows from which origin the distances are measured.



Figure 6.1 Investigated Antenna placement locations for the multiband antenna system

One of the locations 7a or 7b will be selected depending on the simulated gain values at positions 4, 5 and 6.

Table 6.1 shows the X-, Y- and Z-coordinates of the selected positions where the monopole and the patch microstrip antennas are going to be examined.

Table 6.1 the X-, Y- and Z-coordinates of the selected positions for multiband antenna system

Antenna	Position	X-Coordinates	Y-coordinates	Z-coordinates
Monopole	1	-19.43	0	-1.93
	2	-17.50	0	-1.93
	3	-15.57	0	-1.93
	4	0	0	-1.93
	5	5.70	0	-0.69
	6	11	0	0.45
	7a	2.85	0	-1.31
	7b	8.55	0	-0.08
Patch	1	-19.43	0	-1.93
	2	-17.50	0	-1.93
	3	-15.57	0	-1.93
	4	0	0	-1.93
	5	5.70	0	-0.69
	6	11	0	0.45
	7a	2.85	0	-1.31
	7b	8.55	0	-0.08

6.2 Radiation Patterns of the antenna for GPS communication

The following section presents the results for all the simulated radiation patterns of the monopole antenna operating at 1.575 GHz resonant frequency for the GPS communication. Figures 6.2 to 6.9 illustrate 3D far field of the monopole antenna for each position and Figures 6.10 and 6.11 illustrate the 2D total gain distribution for all the positions at $\phi=0$ and $\phi=90$ respectively. Discussion of the results is performed at the end of the section.

Position 1

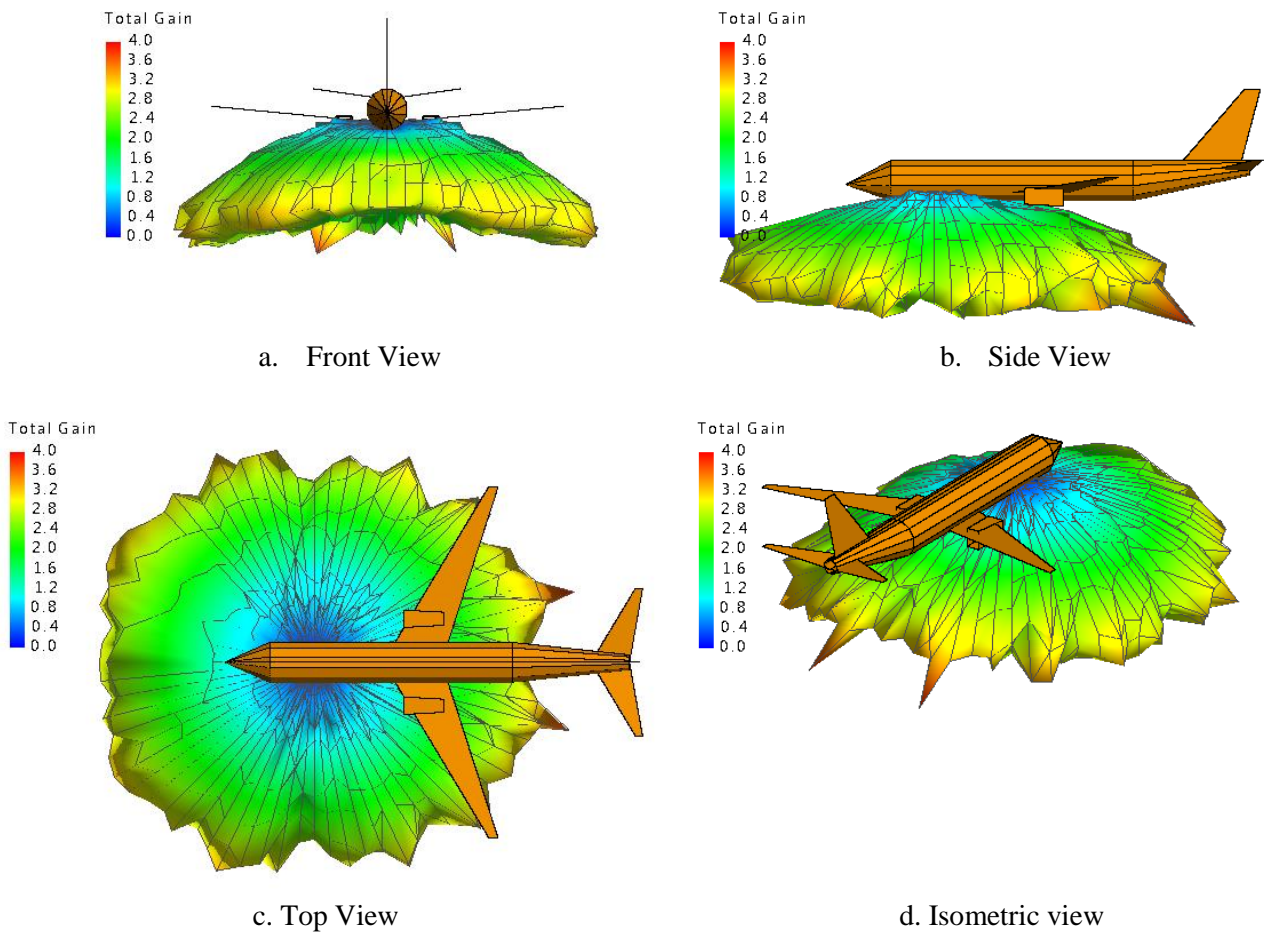


Figure 6.2 3D Radiation pattern of a monopole on the aircraft for GPS communication at 1.575 GHz at position 1; linear scale

Position 2

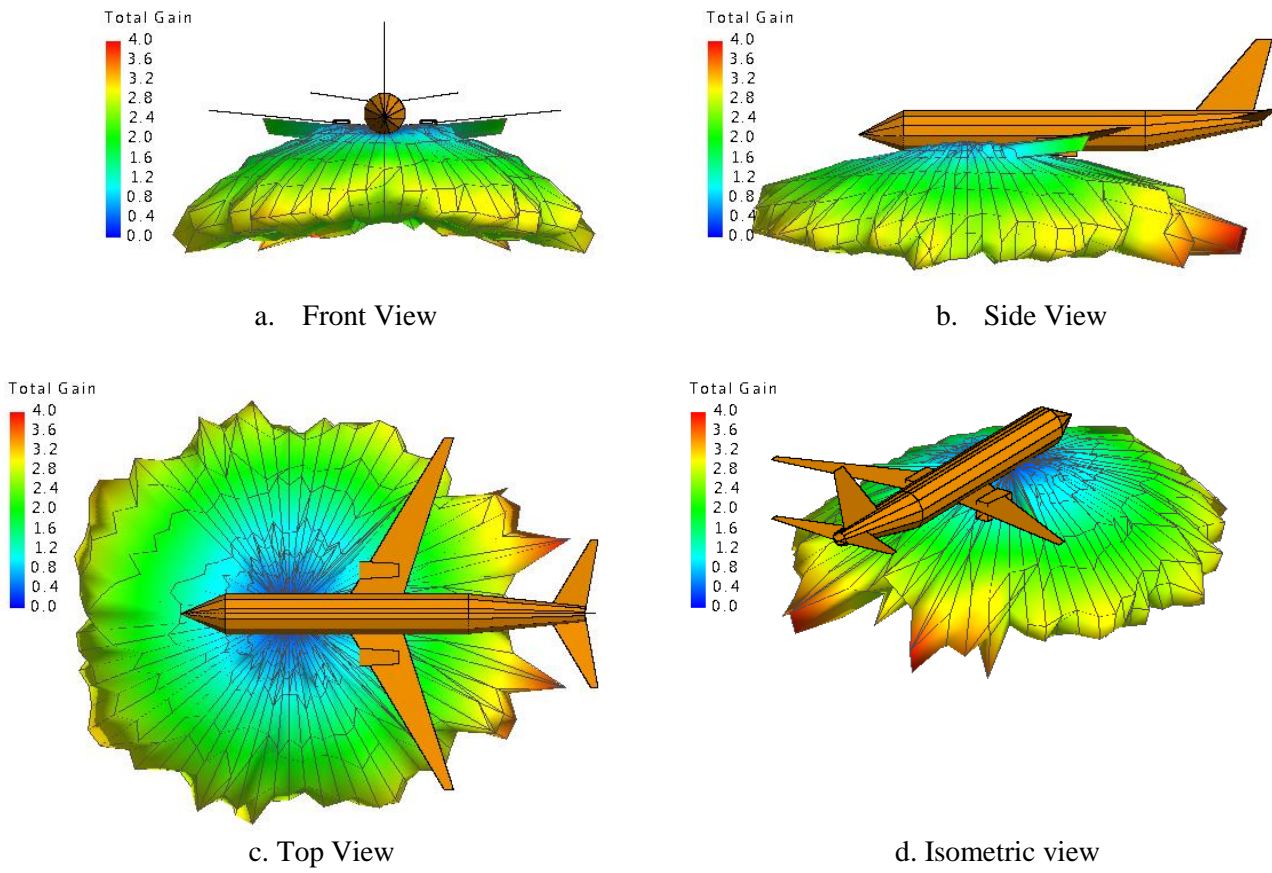


Figure 6.3 3D Radiation pattern of a monopole on the aircraft for GPS communication at 1.575 GHz at position 2; linear scale

Position 3

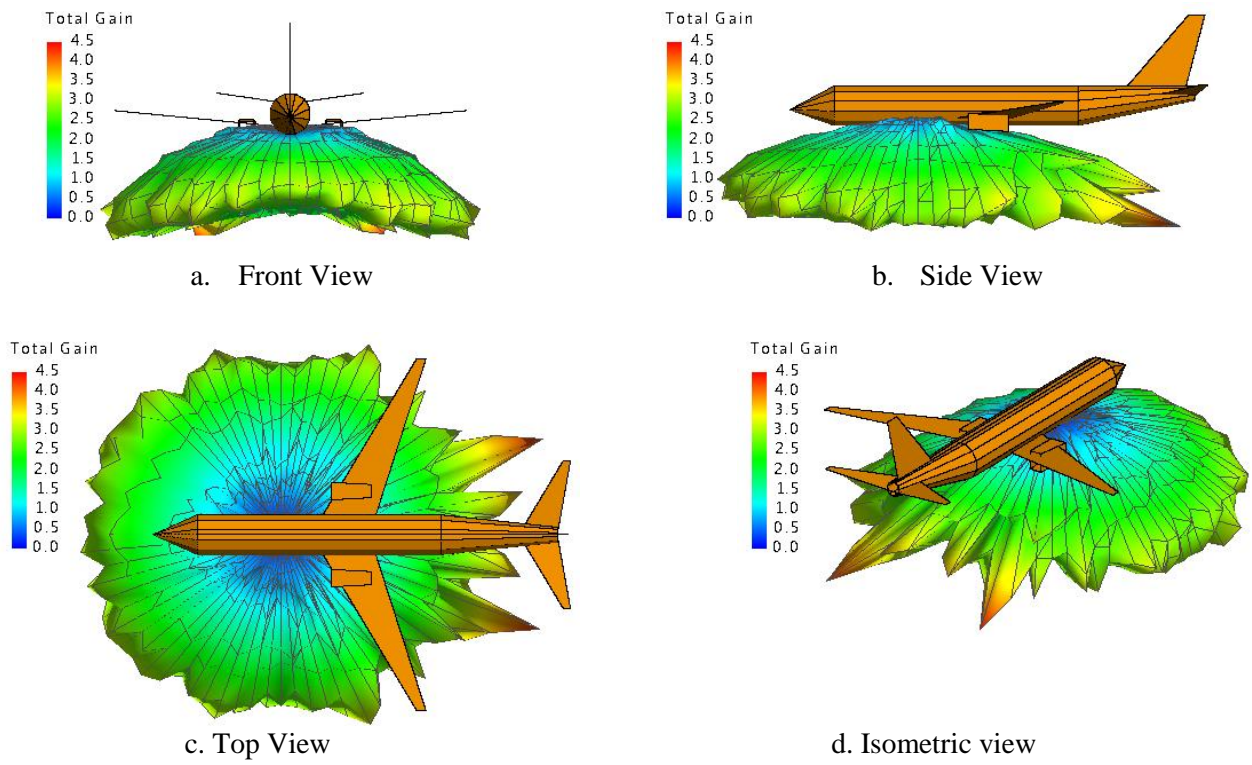


Figure 6.4 3D Radiation pattern of a monopole on the aircraft for GPS communication at 1.575 GHz at position 3; linear scale

Position 4

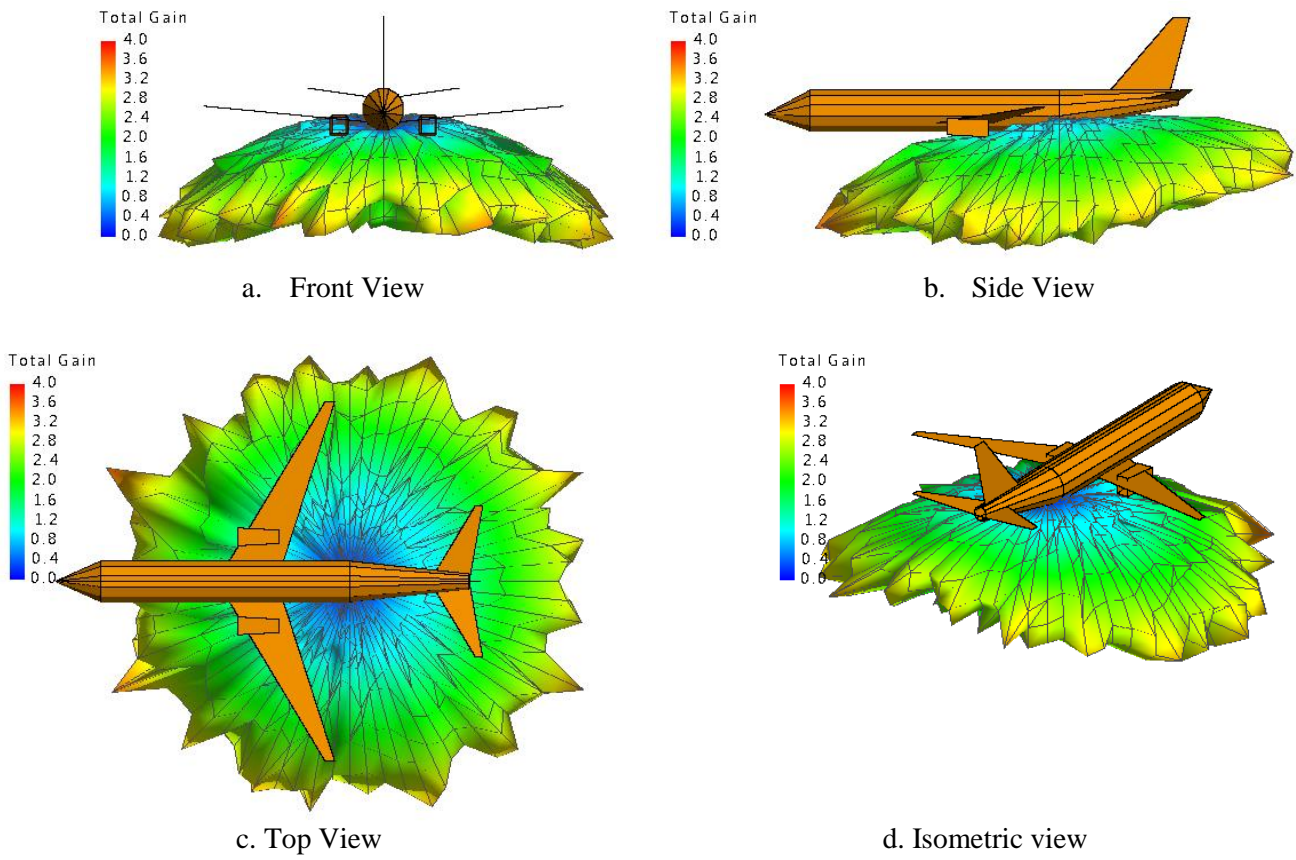
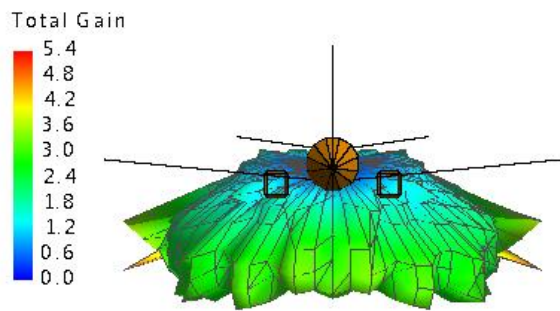
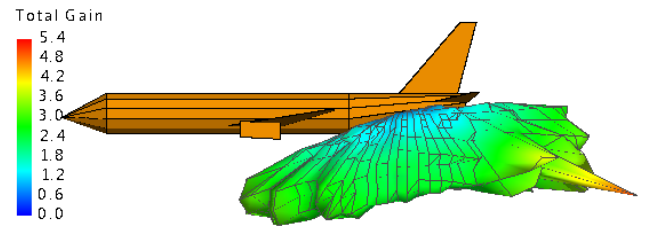


Figure 6.5 3D Radiation pattern of a monopole on the aircraft for GPS communication at 1.575 GHz at position 4; linear scale

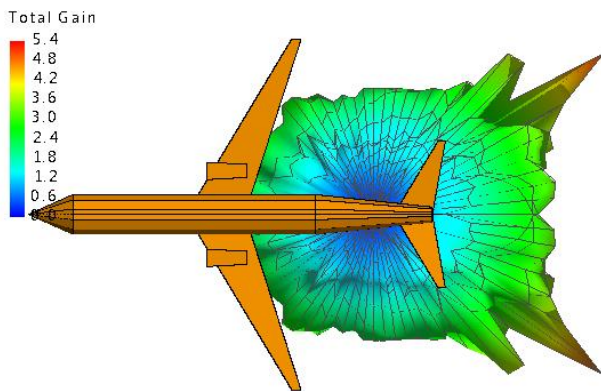
Position 5



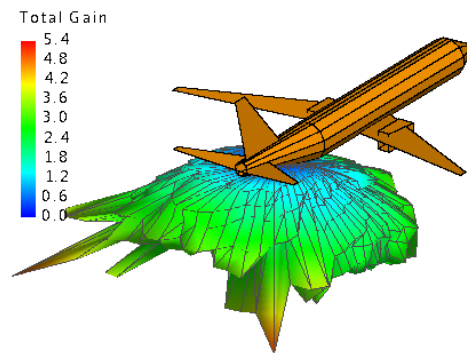
a. Front View



b. Side View



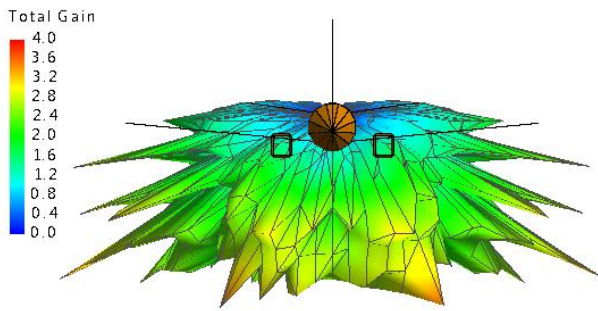
c. Top View



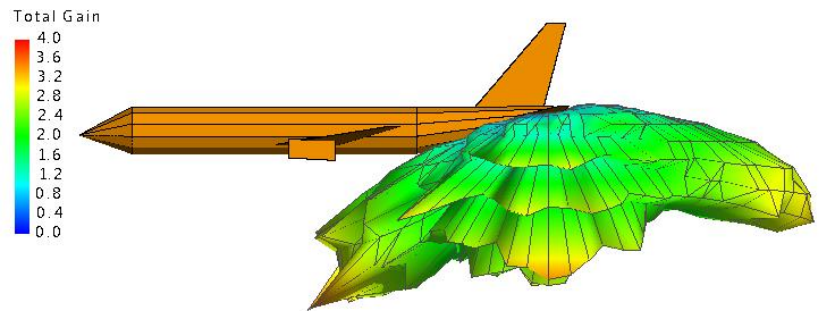
d. Isometric view

Figure 6.6 3D Radiation pattern of a monopole on the aircraft for GPS communication at 1.575 GHz at position 5; linear scale

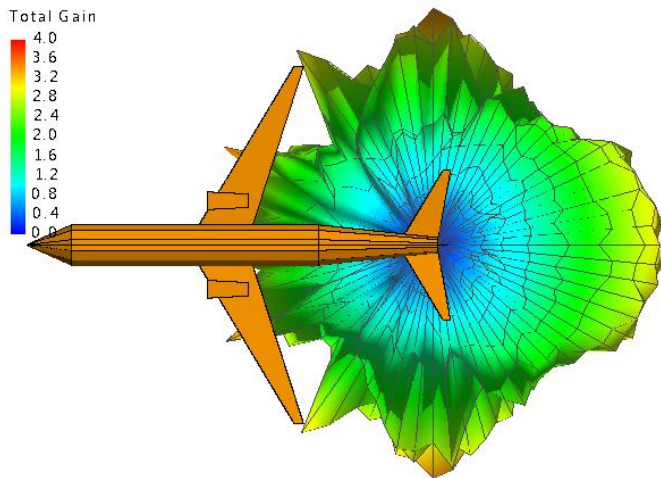
Position 6



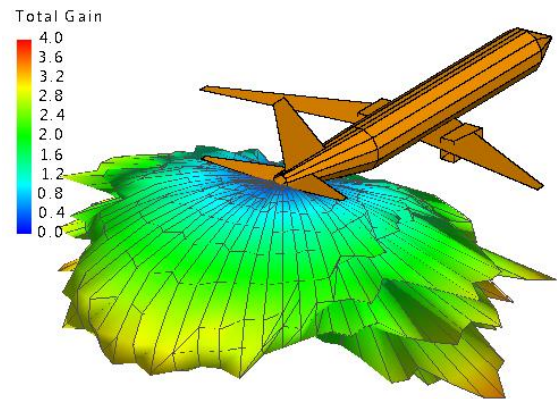
a. Front View



b. Side View



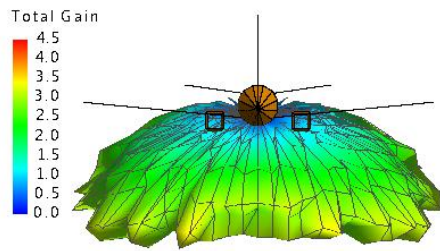
c. Top View



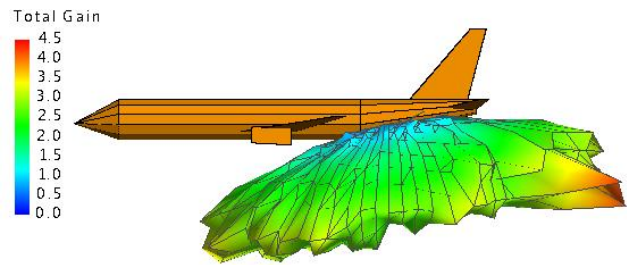
d. Isometric view

Figure 6.7 3D Radiation pattern of a monopole on the aircraft for GPS communication at 1.575 GHz at position 6; linear scale

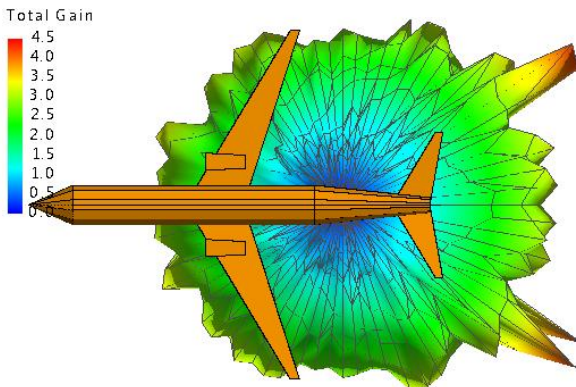
Position 7a



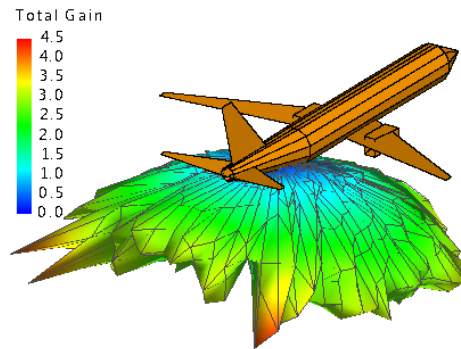
a. Front View



b. Side View



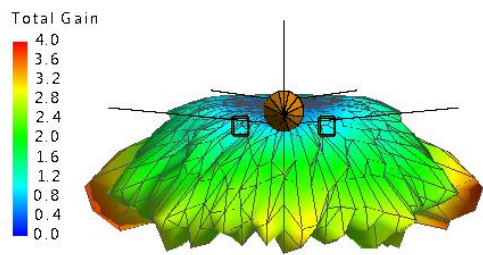
c. Top View



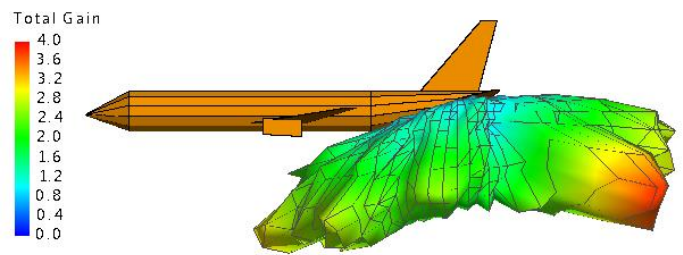
d. Isometric view

Figure 6.8 3D Radiation pattern of a monopole on the aircraft for GPS communication at 1.575 GHz at position 7a; linear scale

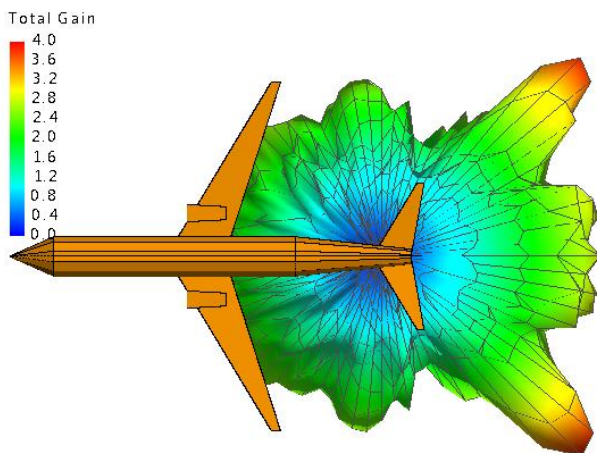
Position 7b



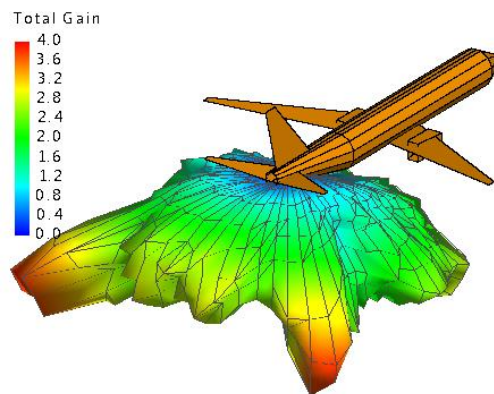
a. Front View



b. Side View



c. Top View



d. Isometric view

Figure 6.9 3D Radiation pattern of a monopole on the aircraft for GPS communication at 1.575 GHz at position 7b; linear scale

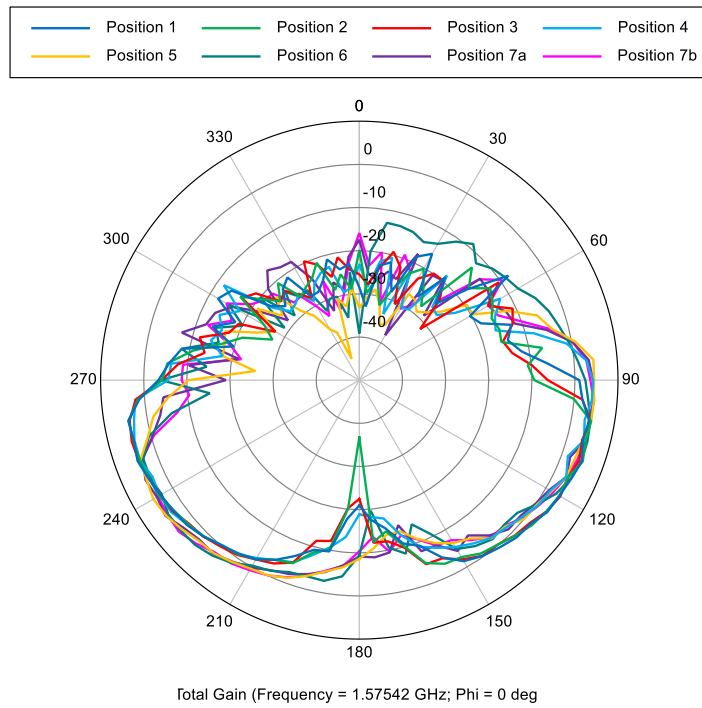


Figure 6.10 2D Radiation patterns of a monopole on the aircraft for GPS communication at 1.575 GHz for all positions at $\phi=0$; dB scale

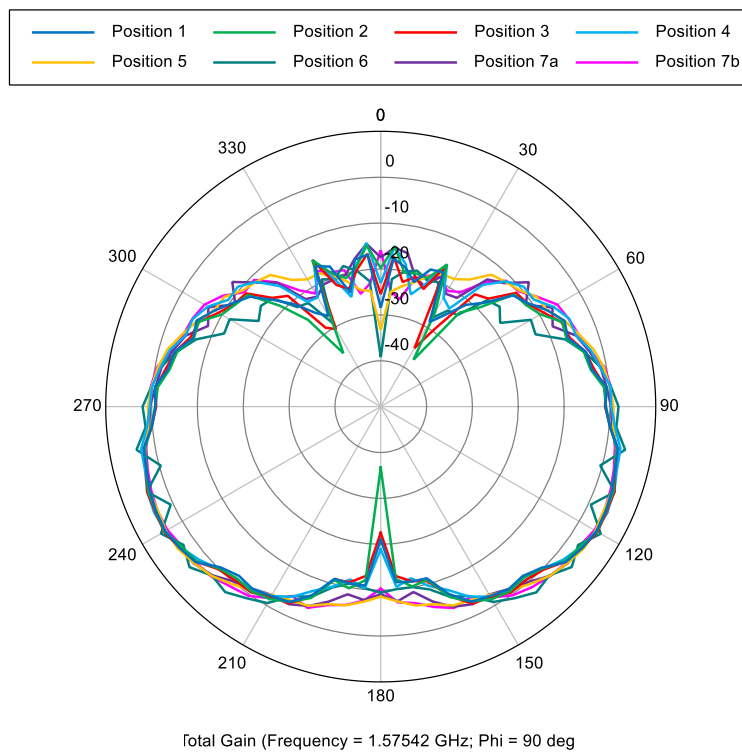


Figure 6.11 2D Radiation patterns of a monopole on the aircraft for GPS communication at 1.575 GHz for all positions at $\phi=90$; dB scale

Discussion of the results for the monopole antenna

The radiation patterns at all positions have a toroidal, donut like shaped gain distribution. Although there are certain side lobes and fluctuations, the overall shape matches well with the radiation pattern that was presented in Chapter 4 in Feasibility Analysis of the flat square plate and the cylinder.

The radiation patterns of the monopole at positions 1, 2 and 3 have a strong link and on average they do not differ more than 0.2 dB. This can be seen in Figures 6.10 and 6.11. This similarity can be explained by the fact that at all the 3 positions, the monopole is located between the nose and the main wings. The radius of the cylinder is constant and there are no other prominent structural elements that could act as a source of scattering bodies.

The radiation pattern of the monopole at positions 4-6, 7a and 7b have a slanted distribution at $\phi=0^\circ$. This is clearly shown in Figure 6.10 and all the side view images in the 3D radiation patterns in Figures 6.2 to 6.9. This is because the radiation pattern follows the shape of the aircraft tail and has the maximum gain directed to higher elevation angles.

The radiation pattern at position 6 shows the strongest peaks and fluctuations. This is clearly visible in Figure 6.7a. Out of all the positions, the monopole at position 6 is located below the horizontal stabilizer and closest to the tip of the tail. These 2 elements have one of the strongest influence because they act as scattering bodies. Also, at position 6 the radius of the cylinder is minimal implying maximal creeping wave effect. And due to the approximation of the aircraft, at position 6 the ribs of the cylinder are closer to the monopole which may also increase the fluctuations in the far field.

Figure 6.11 shows that the radiation pattern is symmetric with respect to the XZ- plane (using the axis system shown in Figure 6.1). This indicates the accuracy of the results because the aircraft is a symmetric structure and the monopole is also a symmetrically radiating element. This symmetry ensures that the wireless link can reach the satellites isotropically in all directions.

Table 6.2 summarizes the Half Power Beam Width (HPBW), maximum gain and the direction of the maximum total gain with respect to the horizon for each antenna position at the YZ-plane.

Table 6.2 HPBW, maximum gain and the direction of the main beam width at $\phi=0$ for the monopole antenna operating at 1.575GHz frequency for GPS communication

Position	HPBW [°]	Maximum Gain [dBi]	Direction of the Main beam Width at $\phi=90^\circ$; θ [°] below the horizon
1	34.8	4.35	25
2	33.8	4.51	25
3	33.8	4.63	25
4	34.9	4.55	25
5	42.4	4.11	26
6	17.25	5.40	35
7a	38.7	4.57	24
7b	49.0	3.86	28

Based on results presented in Table 6.2, all the positions satisfy the main requirement discussed in Chapter 2. The maximum gain does not exceed 6.25 dBi. However, other criteria also influence the optimum position. It is preferable to have a larger Half Power Beam Width. That way more area can be covered and more satellites can be reached. And for the direction of the main beam width it is preferable to have higher elevation angles closer to the horizon. That way the power will not illuminate the Earth but will be directed towards the satellites. Making a trade-off matrix and taking into account all the points, the optimum position for the monopole for a GPS communication link, is located at position 7a. The second best optimum location of the monopole antenna is position 3.

6.3 Radiation Patterns of the antenna for GSM communication

The following section presents the results for all the simulated radiation patterns of the patch antenna operating at 800 MHz resonant frequency for the GSM communication. Figures 6.12 to 6.19 illustrate 3D far field of the patch antenna for each position and Figures 6.20 and 6.21 illustrate the 2D total gain distribution for all the positions at $\phi=0$ and $\phi=90$ respectively. Discussion of the results is presented at the end of the section.

Position 1

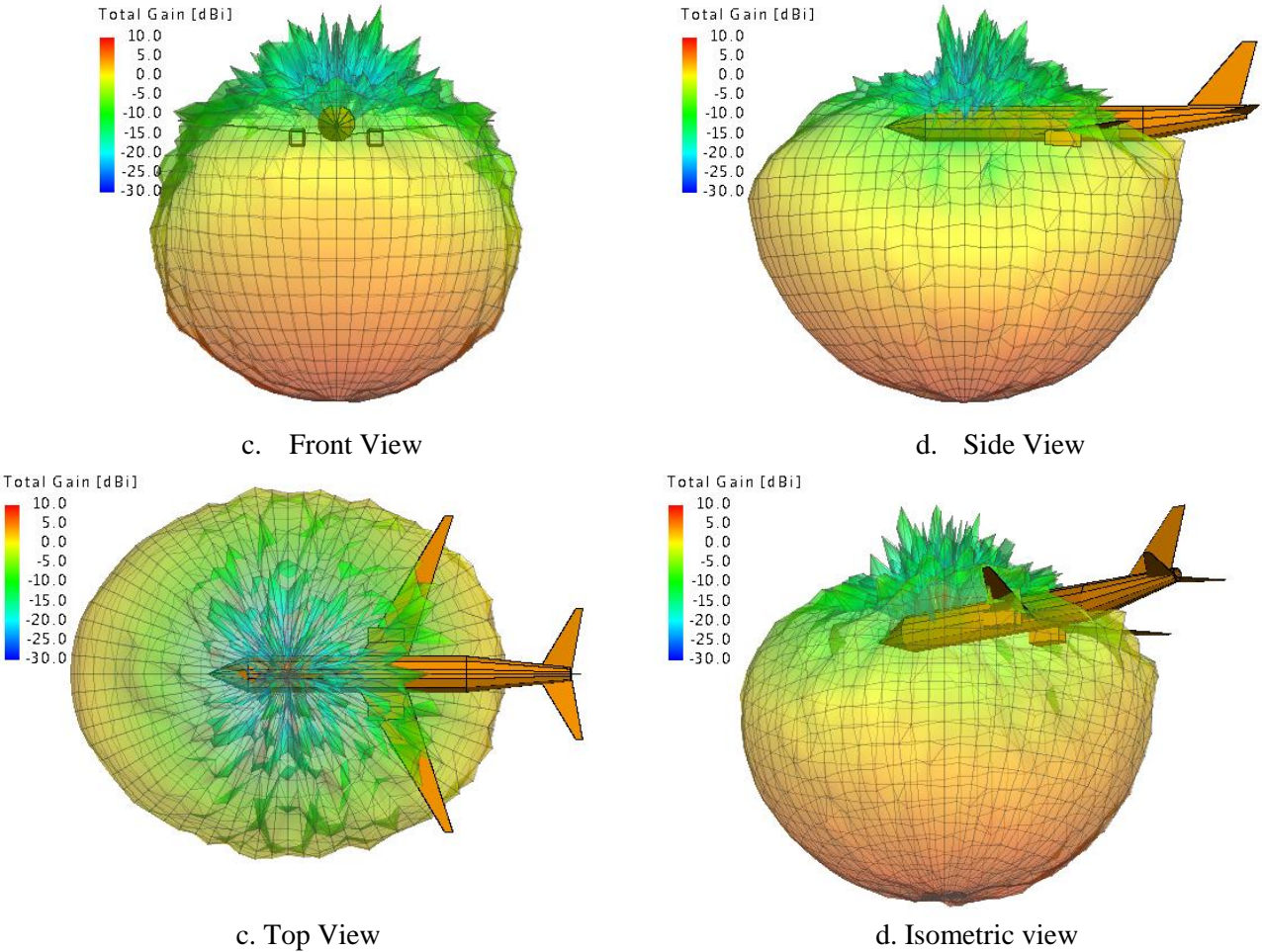
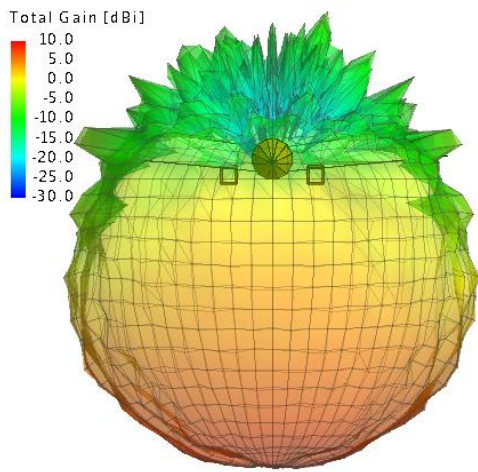
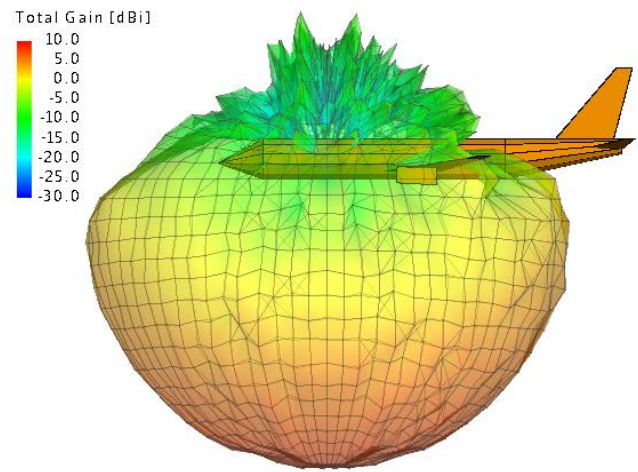


Figure 6.12 3D Radiation pattern of a patch antenna on the aircraft for GSM communication at 800 MHz at position 1; dB scale

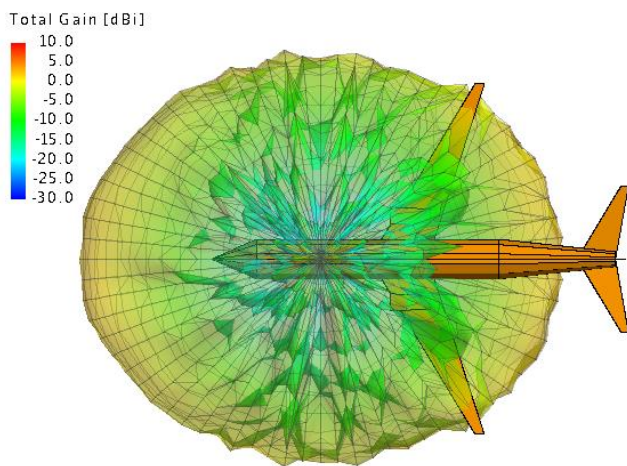
Position 2



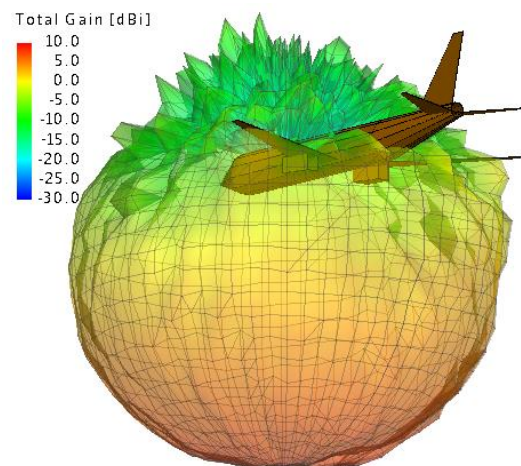
a. Front View



b. Side View



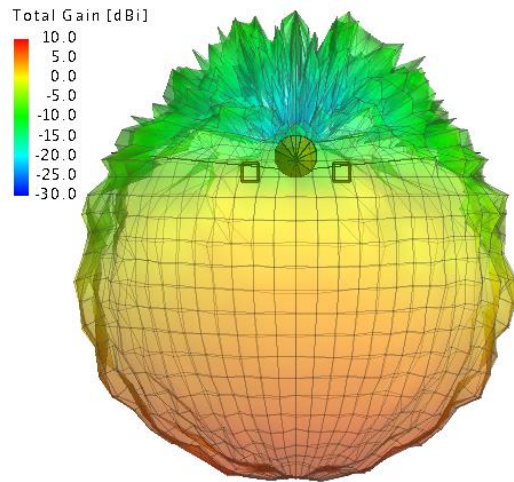
c. Top View



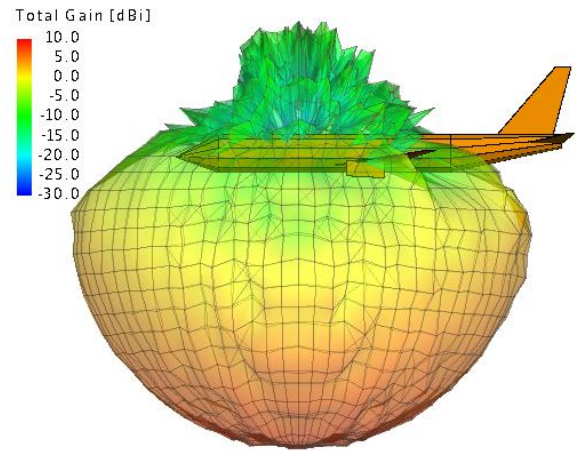
d. Isometric view

Figure 6.13 3D Radiation pattern of a patch antenna on the aircraft for GSM communication at 800 MHz at position 2; dB scale

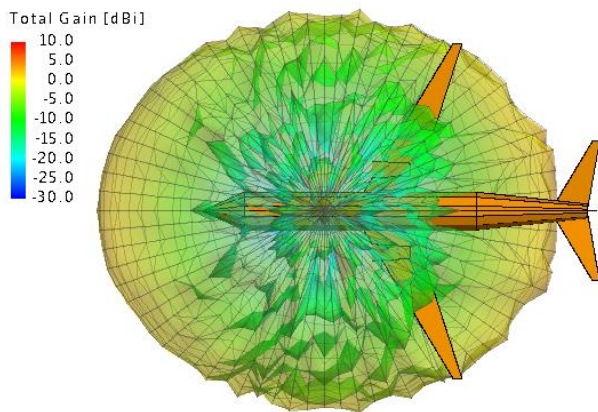
Position 3



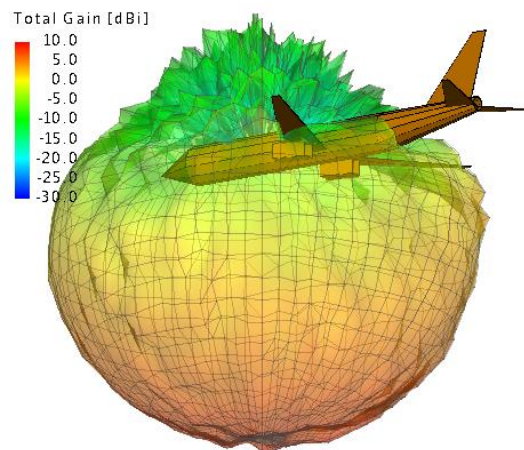
a. Front View



b. Side View



c. Top View



d. Isometric view

Figure 6.14 3D Radiation pattern of a patch antenna on the aircraft for GSM communication at 800 MHz at position 3; dB scale

Position 4

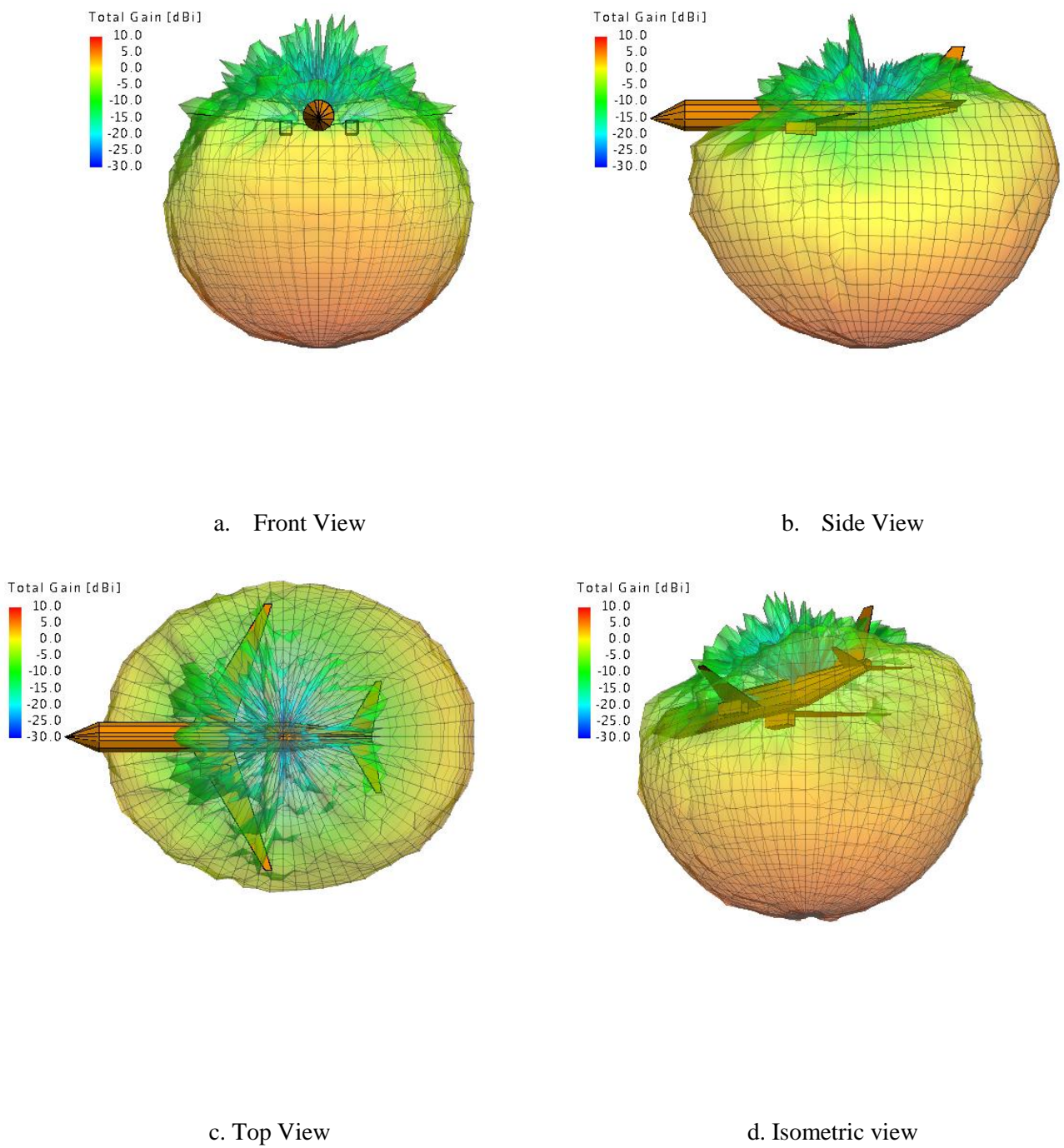
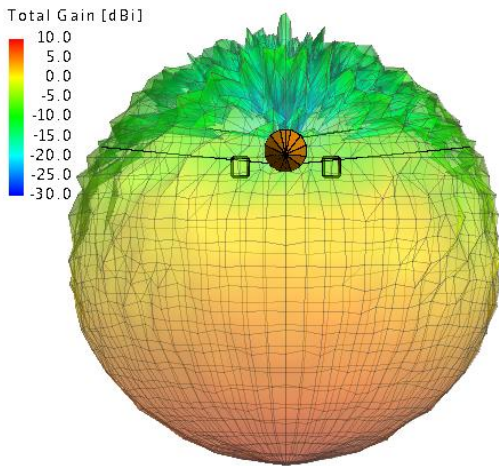
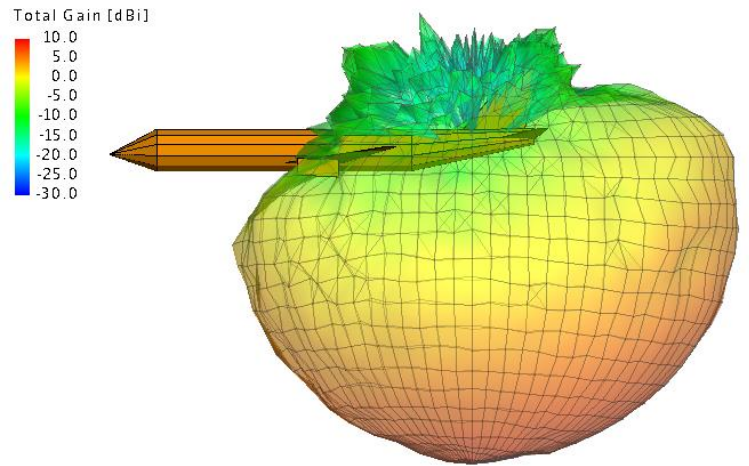


Figure 6.15 3D Radiation pattern of a patch antenna on the aircraft for GSM communication at 800 MHz at position 4; dB scale

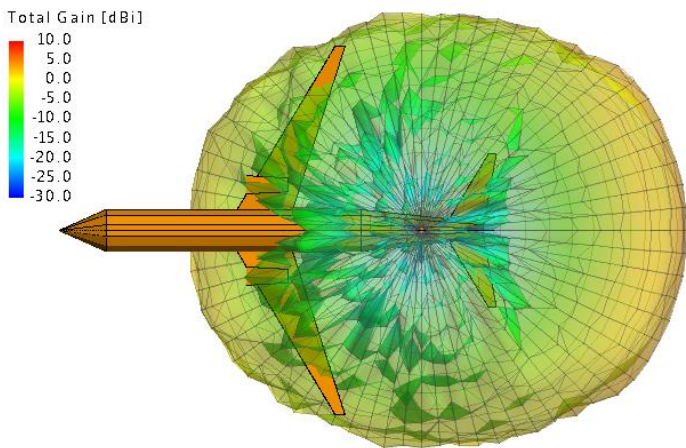
Position 5



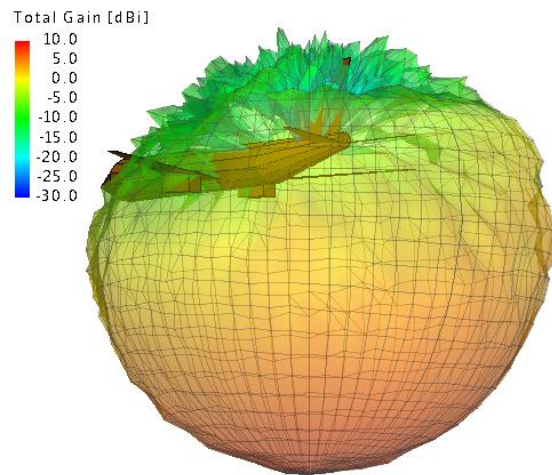
a. Front View



b. Side View



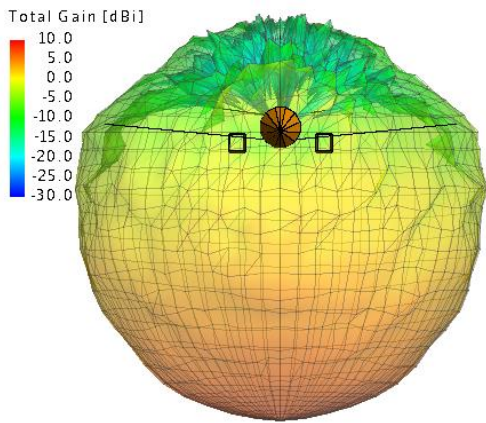
c. Top View



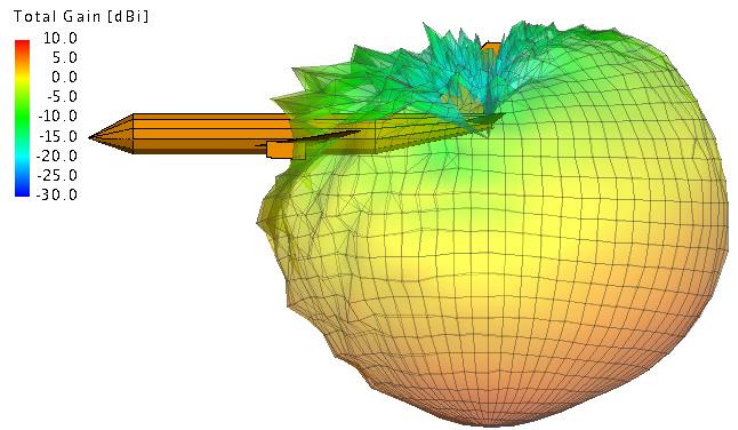
d. Isometric view

Figure 6.16 3D Radiation pattern of a patch antenna on the aircraft for GSM communication at 800 MHz at position 5; dB scale

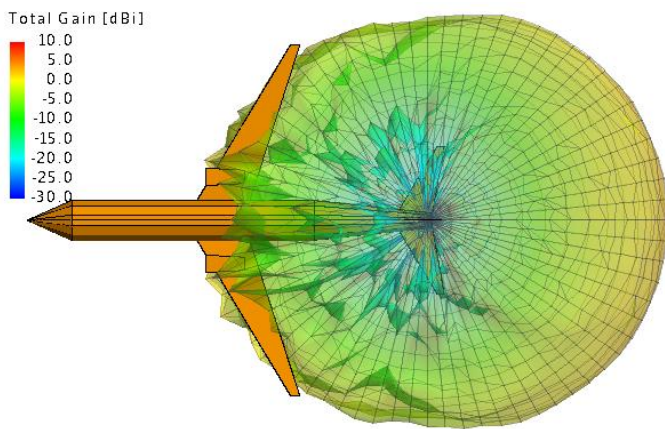
Position 6



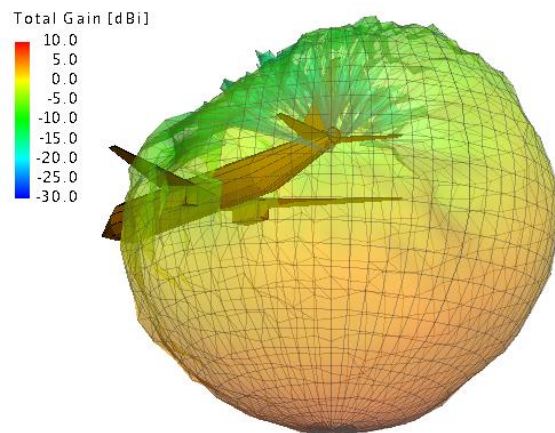
a. Front View



b. Side View



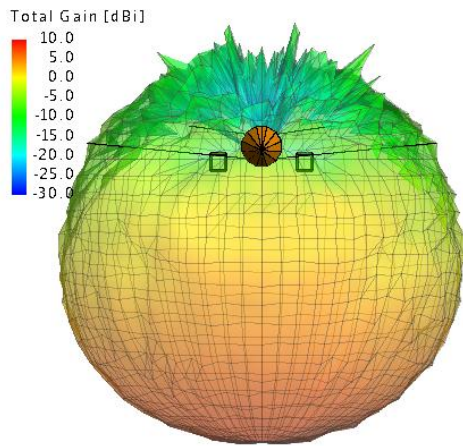
c. Top View



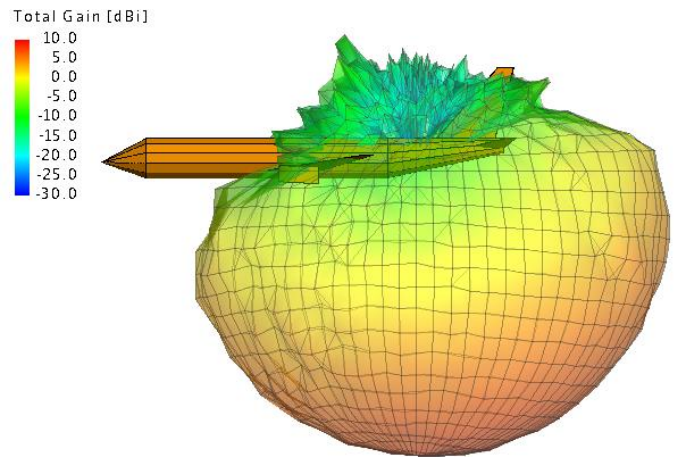
d. Isometric view

Figure 6.17 3D Radiation pattern of a patch antenna on the aircraft for GSM communication at 800 MHz at position 6; dB scale

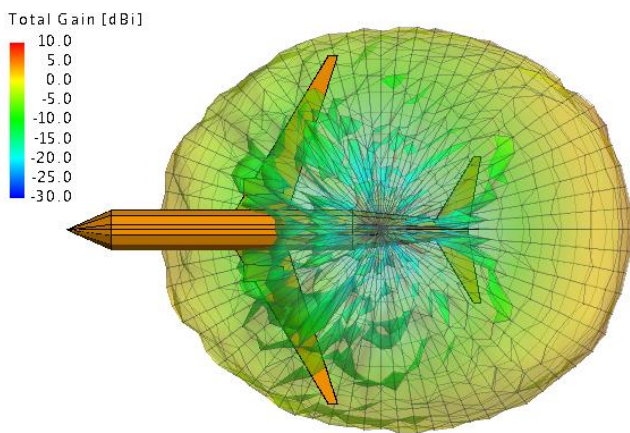
Position 7a



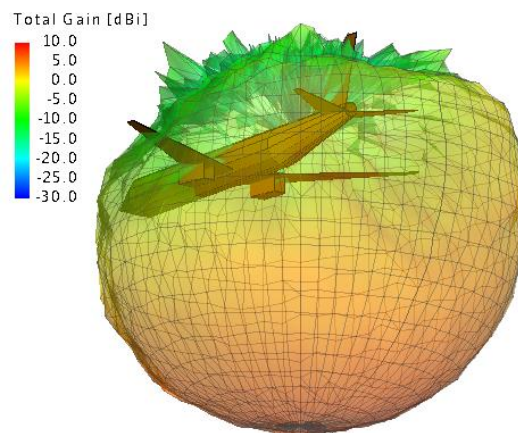
a. Front View



b. Side View



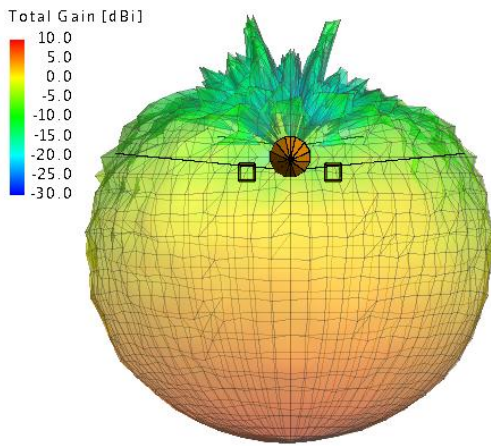
c. Top View



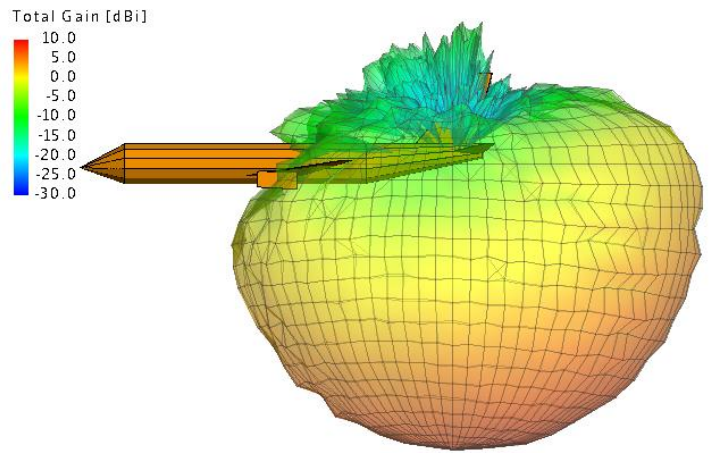
d. Isometric view

Figure 6.18 3D Radiation pattern of a patch antenna on the aircraft for GSM communication at 800 MHz at position 7a; dB scale

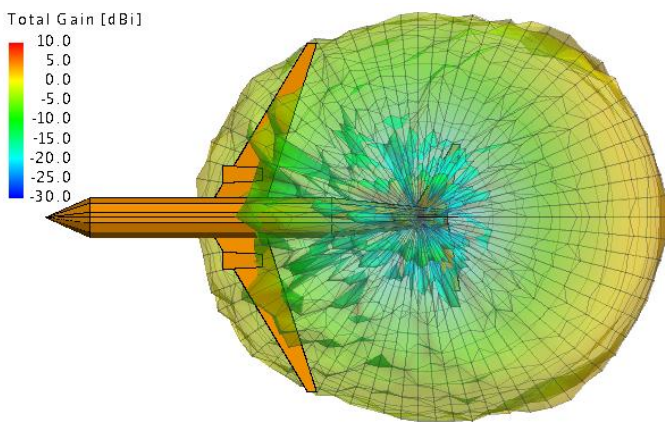
Position 7b



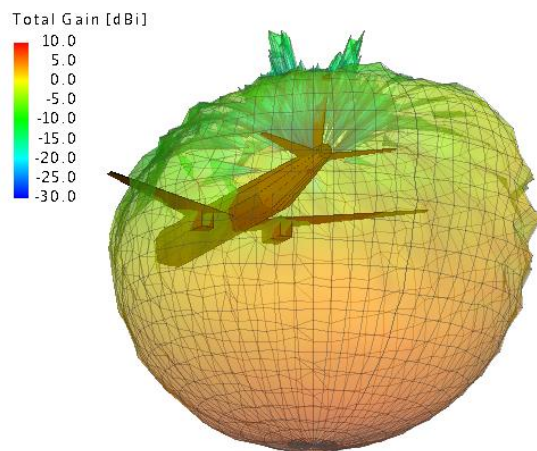
a. Front View



b. Side View



c. Top View



d. Isometric view

Figure 6.19 3D Radiation pattern of a patch antenna on the aircraft for GSM communication at 800 MHz at position 7b; dB scale

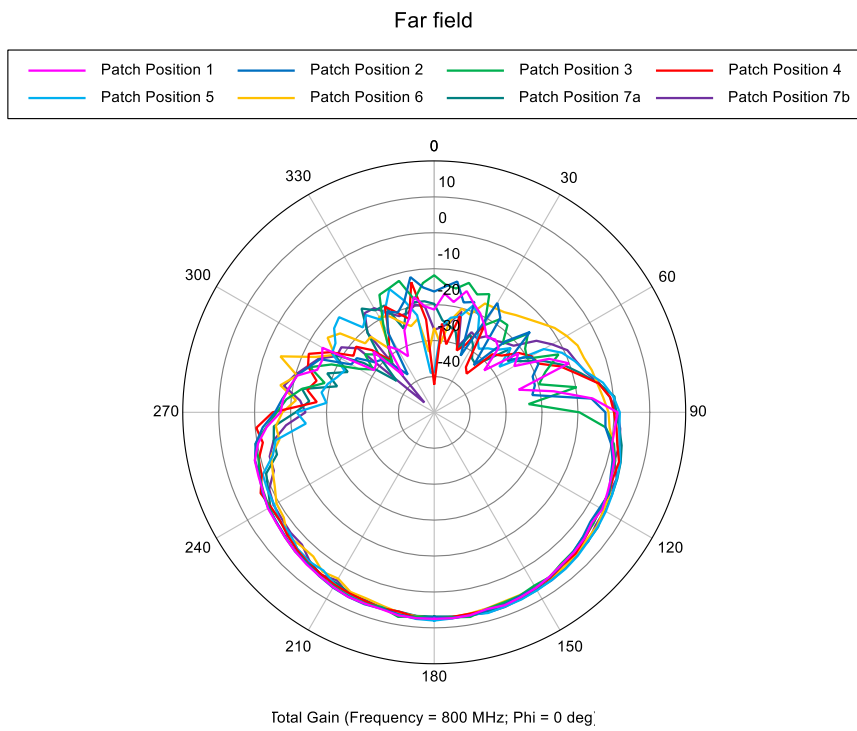


Figure 6.20 2D Radiation patterns of a patch antenna on the aircraft for GSM communication at 800 MHz for all positions at $\phi=0$; dB scale

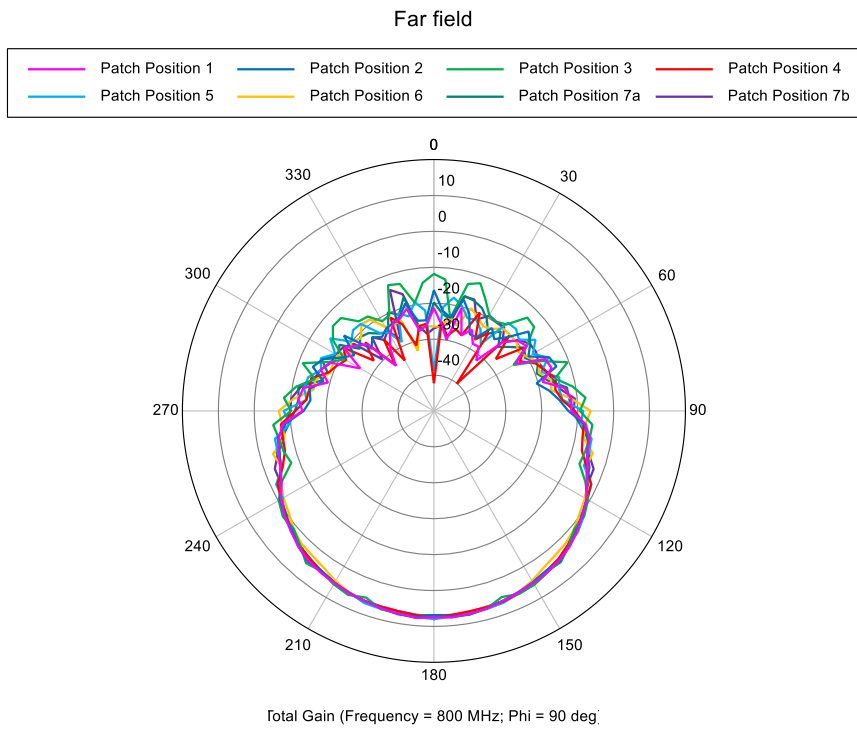


Figure 6.21 2D Radiation patterns of a patch antenna on the aircraft for GSM communication at 800 MHz for all positions at $\phi=90$; dB scale

Discussion of the results for the patch antenna

The radiation patterns at all positions have a hemispherical gain distribution shape. Although there are certain side lobes and fluctuations, the overall shape matches well with the radiation pattern of a typical patch antenna.

The radiation patterns of the patch antenna at positions 1, 2 and 3 have a strong link and on average they do not differ more than 0.05 dB at $\phi=90^\circ$ and 0.1dB at $\phi=0^\circ$. This can be seen in Figures 6.21 and 6.20 respectively. This similarity can be explained by the fact that at all the 3 positions, the patch antenna is located between the nose and the main wings. The radius of the cylinder is constant and there are no other prominent structural elements that could act as a source of scattering bodies.

The radiation pattern of the patch antenna at positions 4-6, 7a and 7b also have a noticeable similarity. They have a slanted distribution at $\phi=0^\circ$. This is because the radiation pattern follows the shape of the aircraft tail and has the maximum gain directed to higher elevation angles.

Figure 6.21 shows that the radiation pattern is symmetric with respect to the XZ- plane (using the axis system shown in Figure 6.1).

Table 6.3 summarizes the Half Power Beam Width (HPBW), maximum gain and the direction of the maximum total gain with respect to the horizon for each antenna position at the YZ-plane.

Table 6.3 HPBW, maximum gain and the direction of the main beam width at $\phi=0$ for the patch antenna operating at 800MHz frequency for GSM communication

Position	HPBW [°]	Maximum Gain [dBi]	Direction of the Main beam Width at $\phi=90^\circ$; θ [°]
1	71.9	7.83	90
2	68.4	7.54	80
3	68.4	7.80	85
4	74.9	7.20	90
5	66.6	7.97	90
6	63.1	7.27	90
7a	80.5	7.20	80
7b	74.5	7.23	90

Based on results presented in Table 6.3, positions 1-3 satisfy the main requirement discussed in Chapter 2. The maximum gain does not exceed 7.40 dBi. Other criteria also influence the optimum position. It is preferable to have a larger Half Power Beam Width. That way more area can be covered and more ground base stations can be reached. And for the direction of the main beam width it is preferable to have 90° angles from the horizon directed towards Earth's surface. Making a trade-off matrix and taking into account all the points, the optimum position for the patch antenna for a GPS communication link, is located at position 7b. The second best optimum location of the patch antenna is equally shared between positions 4 and 7b.

Taking into account findings of the optimum position for the monopole antenna for GPS communication link, the overall placement for both antenna systems is at position 7a.

6.4 Verification

Before proceeding with the further installation and implementation of the SkyfloX project, it is important to check whether the results are reliable. For verification purposes, a monopole and a patch antenna are placed on a COMSOL aircraft model [40]. The COMSOL model is illustrated in Figure 6.22 in two isometric views. The specific model of the aircraft is not mentioned in the source, however the main structural features correspond to the Boeing 737-800, the model is a commercial jet aircraft with engines mounted on the wings and the horizontal stabilizer is low mounted.

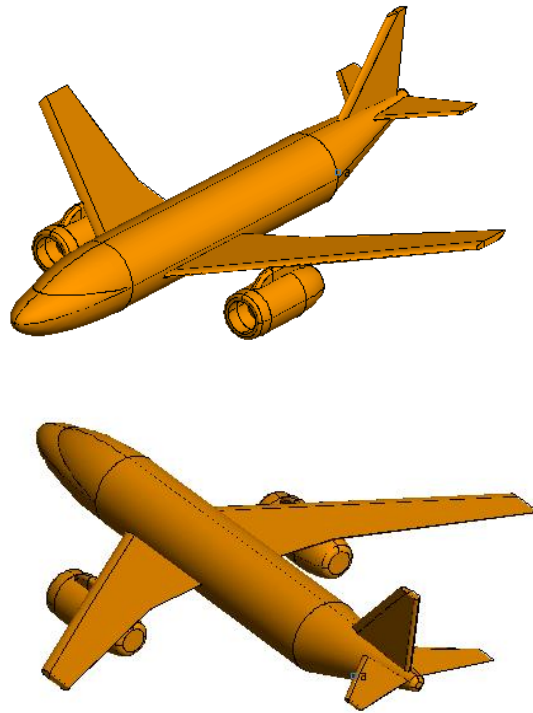
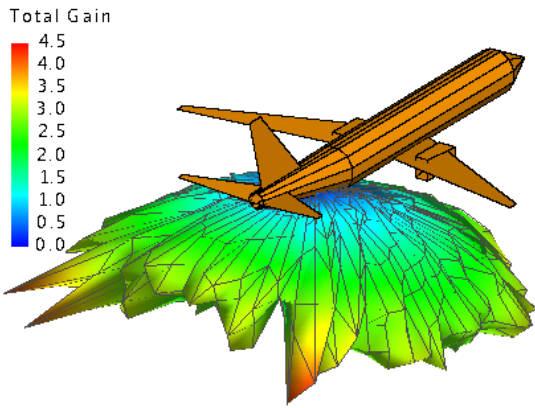


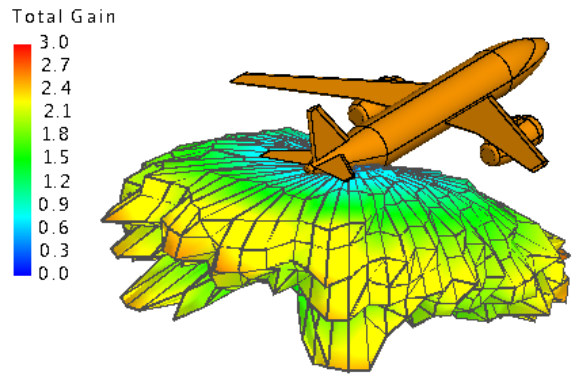
Figure 6.22 COMSOL Aircraft Model in two isometric views [40]

GPS

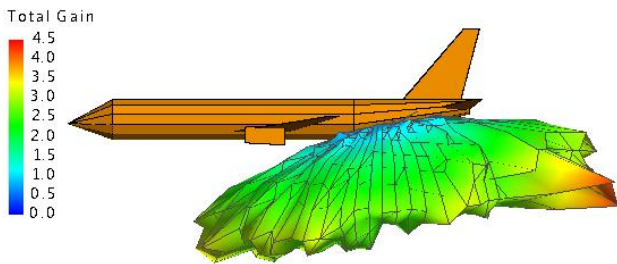
The verification is performed by comparing radiation patterns of a monopole placed at the optimum position 7a. Figure 6.23 compares the 3D radiation patterns between monopole for the COMSOL's model and flat plated model in linear scale. Figures 6.24 and 6.25 illustrate the 2D total gain distribution at $\phi=0^\circ$ and $\phi=90^\circ$ respectively. The solver method is a full wave simulation method which is the MLFMM solver.



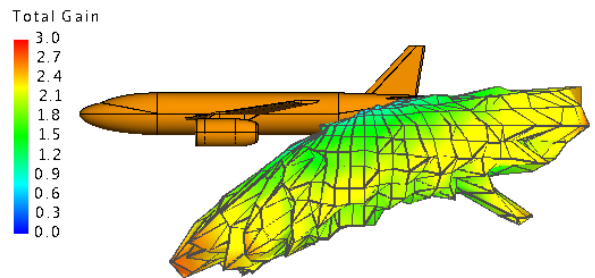
a. Isometric View for a Flat Plated Model



b. Isometric View for COMSOL Model



c. Side View for a Flat Plated Model



d. Side View for COMSOL Model

Figure 6.23 3D Radiation patterns of a monopole on a flat plated model (a,c) and COMSOL model (b,d) for GPS link at 1.575 GHz at position 7a; linear scale

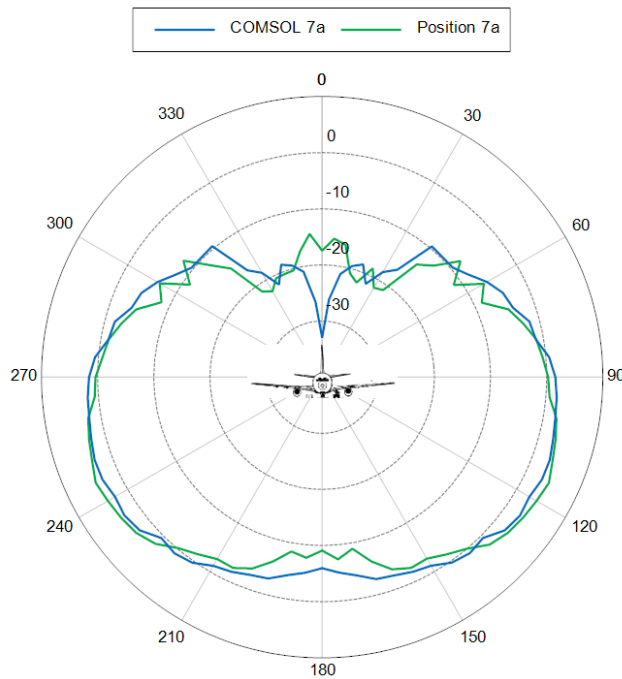


Figure 6.24 2D Radiation pattern of a monopole antenna on the aircraft for GPS communication at 1.575 GHz at position 7a, at $\phi=90^\circ$; dB scale

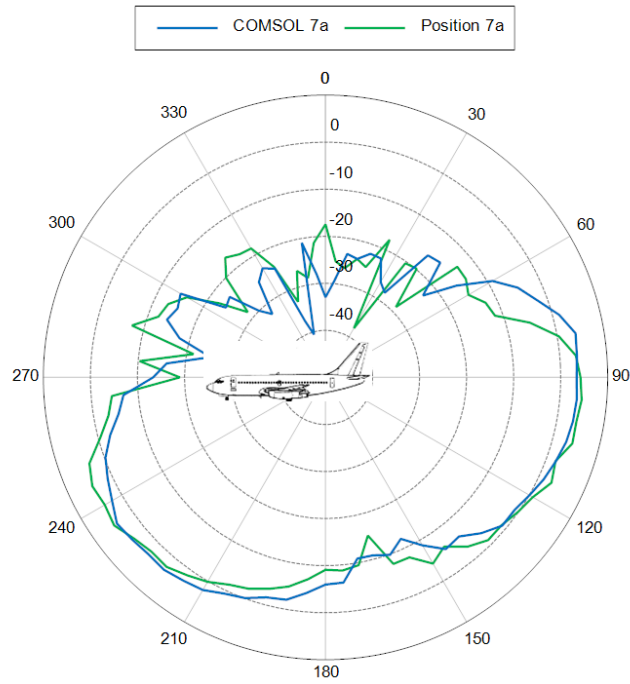


Figure 6.25 Radiation pattern of a monopole antenna on the aircraft for GPS communication at 1.575 GHz at position 7a, at $\phi=0$; dB scale

From the results above, it can be concluded that both the shape of the radiation patterns and the gain values have a strong overall. Moreover, on average the gain does not differ more than 0.8 dB in the direction of the HPBW and maximum gain. The HPBW for the flat plated model at $\phi=0$ is 34.9° and the maximum gain is 4.86 dBi. The HPBW for the COMSOL model is 32.3° and the maximum gain is 4.66 dBi. This results in 8% difference for the HPBW and 4% for the maximum gain difference.

Figure 6.26 shows the radiation pattern of a monopole antenna on the aircraft for GPS communication at 1.575 GHz at position 7a, at $\theta=90$ in dB scale.

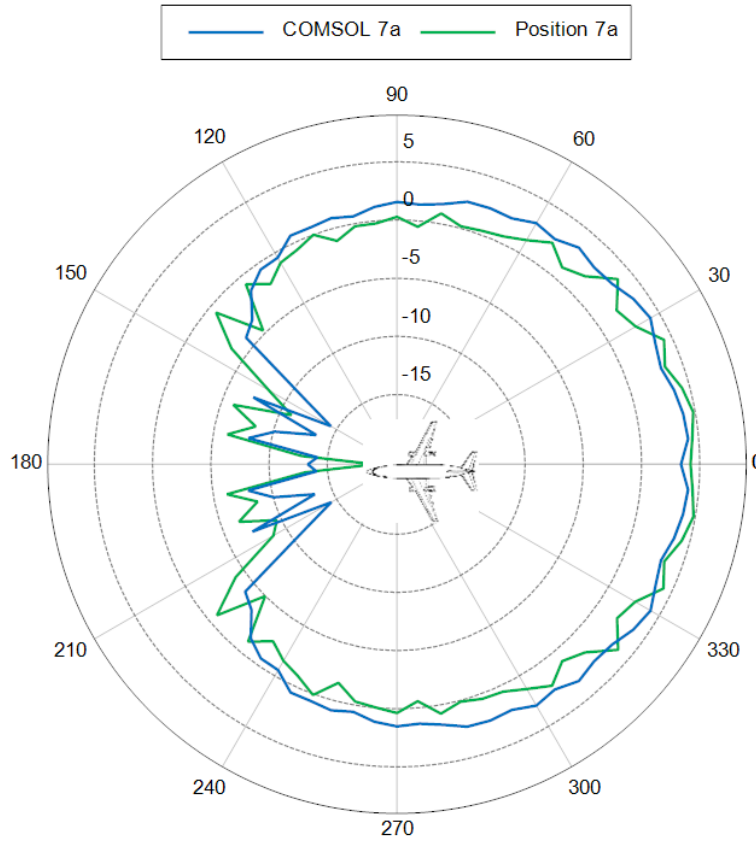


Figure 6.26 Radiation pattern of a monopole antenna on the aircraft for GPS communication at 1.575 GHz at position 7a, at $\theta=90$; dB scale

Finally, the last step is to determine how many satellites can be reached with the verified radiation pattern of the COMSOL model. The same approach as in Chapter 2 is used for determining the area that covers the following section of the sphere where the GPS satellites orbit. The acceptable gain range that is sufficient to provide a reliable signal is between -10.4dB and 7.4dB. From Figure 6.26 it starts from $\varphi=145^\circ$ to $\varphi=215^\circ$; therefore 290° section is covered in phi. The acceptable gain value applies to $\Delta\varphi=290^\circ$ for elevation angles from $\theta_{A2}=30^\circ$ to $\theta_{A1}=-3.4^\circ$ measured from antenna's horizon as can be seen in Figure 6.25. In order to find the coverage area the elevation angles θ_{A1} and θ_{A2} with respect to the aircraft need to be converted to the elevation angle with respect to the Earth's center, θ_{E1} and θ_{E2} . Note that, although at higher elevation angles there are still some section of phi where the gain is larger than minimum gain, they are neglected and will act as redundant. The angle θ_{E1} is calculated in Chapter 2 and equals to 79.5° . The angle θ_{E2} is calculated equating a linear equation and an equation for the circle with radius R, where R is the distance where the GPS satellites are located with respect to the Earth center. Solving the linear equation gives x- and y- coordinates (x_{p2}, y_{p2}) . The angle θ_{E2} becomes:

$$\theta_{E2} = 90^\circ - \arctan\left(\frac{y_{p2}}{x_{p2}}\right) = 90^\circ - \arctan\left(\frac{17\,781\text{ km}}{19\,744\text{ km}}\right) = 48.0^\circ$$

$$\int_0^{290^\circ} \int_{\theta_{E2}}^{\theta_{E1}} R^2 \sin\theta \, d\theta \, d\varphi = (6371 + 20200)^2 * \frac{290^\circ\pi}{180^\circ} * [\cos 48^\circ - \cos 79.5^\circ] = 1.740 \times 10^9 \, \text{km}^2$$

$$\text{Number of visible satellites} = \frac{1.740 \times 10^9}{8.872 \times 10^9} * 31 \text{ satellites} = 6 \text{ satellites}$$

GSM

Figure 6.27 compares the 3D radiation patterns between patch antenna for the COMSOL model and flat plated model in dB scale. Figures 6.28 and 6.29 illustrate the 2D total gain distribution at $\phi=0^\circ$ and $\phi=90^\circ$ respectively. Similarly, the solver method is a full wave simulation method which is the MLFMM solver.

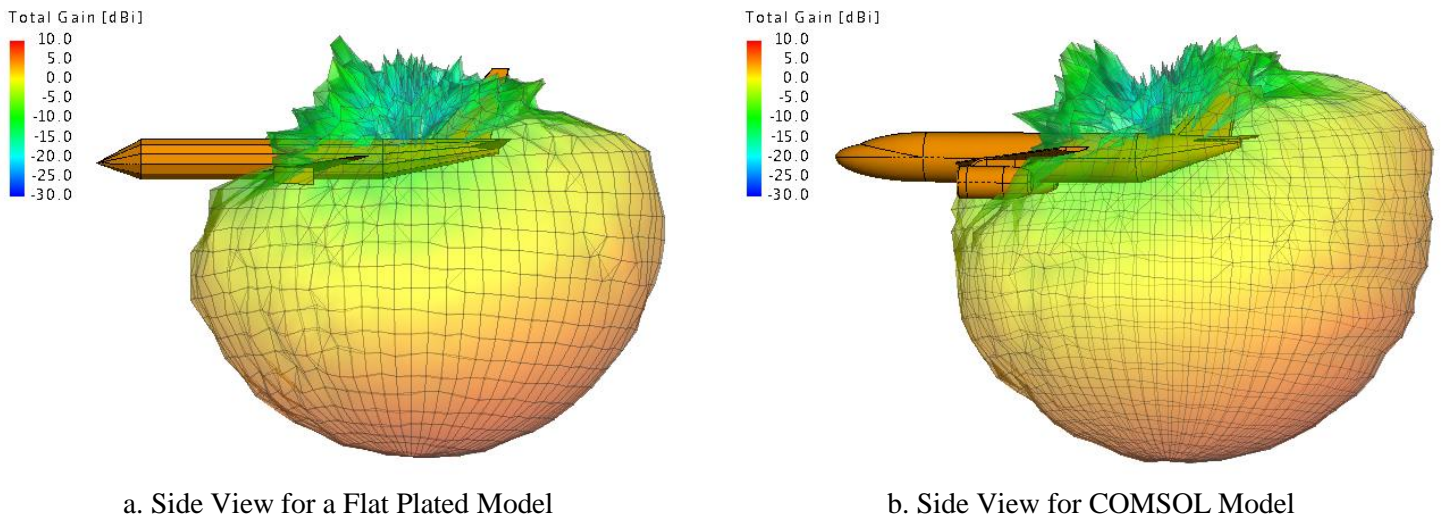


Figure 6.27 3D Radiation patterns of a patch antenna on a flat plated model (a) and COMSOL model (b) for GSM link at 800MHz at position 7a; dB scale

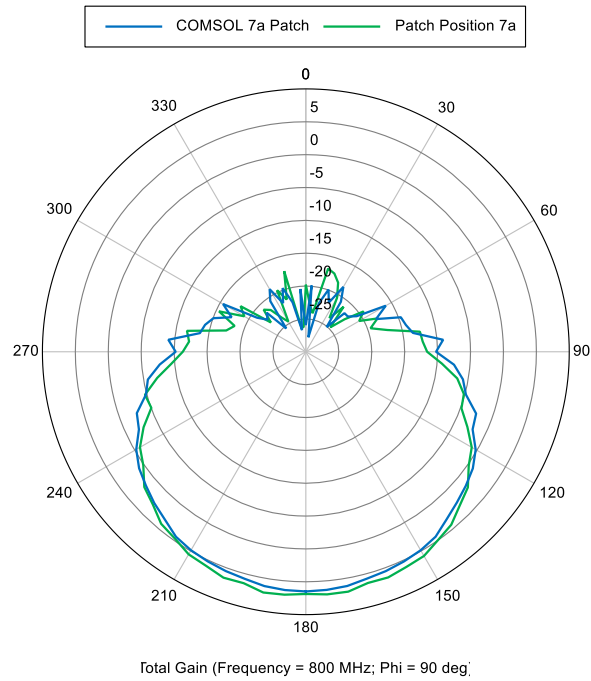


Figure 6.28 2D Radiation pattern of a patch antenna on the aircraft for GSM communication at 800 MHz at position 7a, at phi=90; dB scale

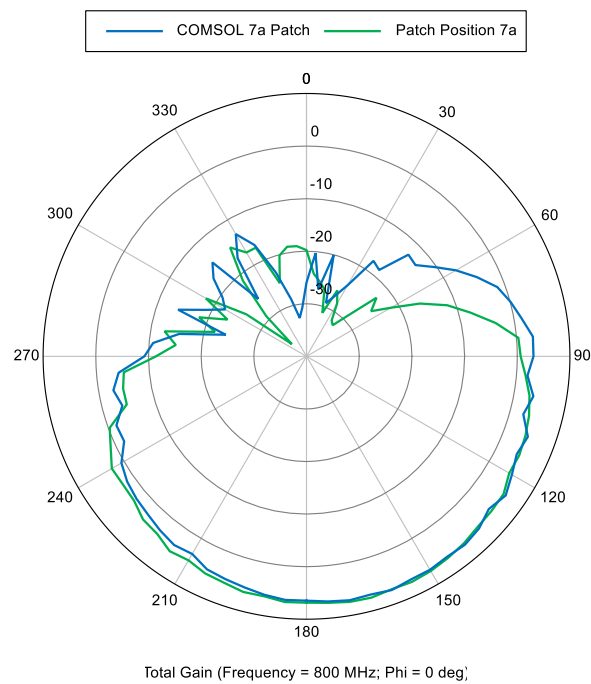


Figure 6.29 2D Radiation pattern of a patch antenna on the aircraft for GSM communication at 800 MHz at position 7a, at phi=0; dB scale

Similarly as to the monopole antenna, from the results above, it can be concluded that both the shape of the radiation patterns and the gain values have a strong overall for the patch antenna as well.

Moreover, on average the gain does not differ more than 0.5 dB in the direction of the HPBW and maximum gain. The HPBW for the flat plated model at $\phi=0$ is 97.9° and the maximum gain is 7.2 dBi. The HPBW for the COMSOL model is 90.2° and the maximum gain is 7.3 dBi. This results in 8.5% difference for the HPBW and 2% for the maximum gain difference.

6.5 Conclusion

The Chapter describes the results of an analysis of the multiband antenna system placement on the approximated aircraft model. Eight possible positions were identified where it is feasible to place the antenna system. For the monopole antenna all positions satisfied the main requirement and resulted in an adequate radiation pattern. For the patch antenna only 4 positions satisfied the requirements. After making a trade-off matrix by taking into account maximum gain, Half Power Beam Width (HPBW) and the direction of the main lobe, the optimum placement of the antenna system is found at position 7a, in the tail at the lower part of the aircraft.

The verification of the results is performed using full wave simulation method MLFMM. Both radiation patterns for a monopole and patch antenna have an evident overlap between flat plated model and the COMSOL model. For the monopole antenna the difference between the maximum gain is 4% and for the HPBW is 8%. For the patch antenna the difference between the maximum gain is 2% and for the HPBW is 8.5%.

Chapter 7 Conclusions

The purpose of this research is to investigate the optimum position for an antenna system on a commercial aircraft such that it can provide a wireless communication link to multiple users at different frequencies. The antenna system consists of 2 individual antennas. The quarter wavelength monopole operating at 1.575 GHz in L1 band for the GPS communication and a patch antenna with dielectric constant of 2.2 for the substrate operating at 800 MHz for the GSM communication. In order to satisfy the coverage and link budget analysis the required operational gain range for the GPS link should be between -10.4 dB to 7.9dB; and for the GSM link the minimum gain of the receive antenna on the aircraft should not be smaller than -8.5dB and should not exceed 7.4dB. The optimum position is located at the bottom of the Boeing 737 in the conical section of the tail 30.95 m away from the tip of the nose in the longitudinal direction.

The optimisation is performed by analysing the radiation patterns of the antennas placed at different locations on the aircraft. FEKO simulation platform is used for estimating the radiation patterns. Several solving methods are applicable in order to answer the research question. In order to choose the appropriate solver, the radiation patterns are compared by placing an antenna on a square plate and a cylinder using 3 methods: Multi-Level Fast Multipole Method (MLFMM), Physical Optics and Uniform Theory of Diffraction method (UTD). Based on the feasibility study it was found that UTD resulted in accurate results for a square plate. The UTD method requires significantly lower computational resources in terms of CPU time and memory and it is most suitable for treating electrically very large bodies therefore it was chosen as the solver to analyse the radiation pattern on the actual aircraft.

The geometry and structural features of Boeing 737 is chosen because it is one of the most commonly purchased and operated commercial aircrafts. Approximation of the aircraft is influenced by the simulation platform and the solver. Since UTD method was chosen, the aircraft is approximated with PEC flat plates and the minimal edge length in a model is set to be not larger than 1.2 wavelength. The cylinder is approximated with 12 plates in the circumference. The wings, horizontal stabilizer and the vertical fin are modeled as 2D flat surface, since the results of the radiation pattern have a strong match between 3D and 2D models and differ on average not more than 0.1 dB.

Eight possible positions were identified where it is feasible to place the antenna system. For the monopole antenna all positions satisfied the main requirement and resulted in adequate radiation patterns. For the patch antenna only 4 positions satisfied the requirement. After making a trade-off matrix by taking into account maximum gain, Half Power Beam Width (HPBW) and the direction of the main lobe, the optimum placement of the antenna system is found at position 7a, in the tail at the lower part of the aircraft.

The verification of the results is performed using full wave simulation method MLFMM. Both radiation patterns for a monopole and patch antenna have an evident overlap between flat plated model and the COMSOL model which models the aircraft with curvilinear surfaces. For the monopole antenna the difference between the maximum gain is 4% and for the HPBW is 8%. For the patch antenna the difference between the maximum gain is 2% and for the HPBW is 8.5%.

Finally, the research shows that it is a feasible solution for installing a multiband antenna system on an aircraft for the SkyfloX project, therefore the initial problem has been solved. Using a UTD method for estimating a radiation pattern provides reasonable first order total gain values. This can further be

used for estimating radiation patterns of antennas on other larger bodies such as marine ships or complex large scale structures as city environment.

Chapter 8 Recommendations

The purpose of this research was to investigate the optimum position for an antenna system on a commercial aircraft such that it can provide a wireless communication link to GPS satellites and GSM ground base stations. Although more than one position was found where the antenna system produces adequate radiation patterns and satisfies the requirements, there are several options that can be undertaken in order to extend and improve the results.

- Boeing 737-800 is chosen as the commercial aircraft model for the investigation, however other aircrafts with different sizes and structural features are also possible for the implementation for the SkyfloX project. For example Fokker 100 which has jet engines mounted on the fuselage at the tail and high mounted horizontal stabilizer. The radiation pattern of the antenna system will likely differ with different aircraft models.
- Smaller structural details were not taken into account such as the windows, extended ailerons, flaps, slats, spoilers, rudder and elevators. So the effects of deployed flight control surfaces can be investigated.
- Another important aspect is the material choice. In the simulations the commonly used aluminium skin of the aircraft is approximated with PEC. For the future scope it would be advisable to change the material properties to metallic and for further analysis to a composite alternative.
- The aircraft model simulated in FEKO does not take into account the effects of vibrations and interference sources, thus the model could be improved and extended to incorporate these effects.
- Other antennas could be analysed to produce similar radiation pattern. For example a helix antenna could be used.

References

- [1] National Centers for Environmental Information. (2018, March). Wildfires - Annual 2018. Retrieved from <https://www.ncdc.noaa.gov/sotc/fire/201713>
- [2] Global Threats to Planer. (2019). Global Land Coverage Change - Wildfires. Retrieved from https://stateoftheworldsplants.org/2017/report/SOTWP_2017_8_global_land_cover_change_wildfires.pdf
- [3] Pioneer. (2019). *Flooding Impact on Crops*. Retrieved from <https://www.pioneer.com/home/site/us/agronomy/crop-management/adverse-weather-disease/flood-impact>
- [4] Feng, J., Tang, H., Bai, L., Zhou, Q., & Chen, Z. (2007, August). New Fast Detection Method of Forest Fire Monitoring and Application Based on FY-1D/MVISR Data. In *International Conference on Computer and Computing Technologies in Agriculture* (pp. 613-628). Springer, Boston, MA.
- [5] SkyfloX. (2016). Optical and RF Constellation on Aircraft. Retrieved from <https://skyflox.eu/>
- [6] Flightradar24. (n.d.). *Live Flight Tracker - Real-Time Flight Tracker Map*. Retrieved from <https://www.flightradar24.com/data/statistics>
- [7] MRO. (2018). *Understanding Today's Antenna Complexities*. Retrieved from <https://www.mro-network.com/engineering-design/understanding-today-s-antenna-complexities>
- [8] Rao, B. R., Rosario, E. N., & Davis, R. J. (2006, April). Radiation pattern analysis of aircraft mounted GPS antennas and verification through scale model testing. In *2006 IEEE/ION Position, Location, And Navigation Symposium* (pp. 306-318). IEEE.
- [9] Vishnevsky, A. V., & Ivanov, V. A. (2018, May). 3D co-site interference modelling between aircraft antennas for the purpose of their best placement. In *2018 22nd International Microwave and Radar Conference (MIKON)* (pp. 151-154). IEEE.
- [10] Gao, S.P. (n.d.). *Surrogate Models for Antenna Placement on Large Platforms*. Retrieved from http://blog.altair.co.kr/wp-content/uploads/2017/10/Altair_SS_iHPC-A4-Web.pdf
- [11] Heckler, M. V. T., & Dreher, A. (2005, July). Analysis of monopoles installed on airframes. In *2005 IEEE Antennas and Propagation Society International Symposium* (Vol. 2, pp. 280-283). IEEE.
- [12] Macnamara, T. (2010). *Introduction to antenna placement and installation*. John Wiley & Sons.
- [13] Altair Hyperworks FEKO Overview. (n.d.). *FEKO Overview*. Retrieved from <https://altairhyperworks.com/product/FEKO#>
- [14] Coote, D., (n.d.). Computational Electromagnetics.[Power Point Slides]. Retrieved from <https://slideplayer.com/slide/4137702/>
- [15] Tzoulis, A., & Eibert, T. F. (2005). A hybrid FEBI-MLFMM-UTD method for numerical solutions of electromagnetic problems including arbitrarily shaped and electrically large objects. *Transactions on Antennas and Propagation*, 53(10), 3358-3366. IEEE.

- [16] Yan, Y., Zhang, Y., Liang, C. H., Garcia-Donoro, D., & Zhao, H. (2012). EMC analysis of antenna system on the electrically large platform using parallel MoM with higher-order basis functions. *Progress In Electromagnetics Research*, 22, 271-287.
- [17] Pathak, P. H., Carluccio, G., & Albani, M. (2013). The uniform geometrical theory of diffraction and some of its applications. *IEEE Antennas and Propagation magazine*, 55(4), 41-69.
- [18] Burnside, W. D. (1972). *Analysis of on-aircraft antenna patterns* (Doctoral dissertation, The Ohio State University).
- [19] Parkinson, B. W., Enge, P., Axelrad, P., & Spilker Jr, J. J. (Eds.). (1996). *Global positioning system: Theory and applications, Volume II*. American Institute of Aeronautics and Astronautics.
- [20] U.S. Defense Department. (n.d.). *Space Segment*. Retrieved from <https://www.gps.gov/systems/gps/space/>
- [21] Masterclock. (2019, January 14). *GPS vs. GNSS: Understanding PNT Satellite Systems*. Retrieved from <https://www.masterclock.com/company/masterclock-inc-blog/gps-vs-gnss>
- [21] ESA. (2011). *GNSS Signal*. Retrieved from https://gssc.esa.int/navipedia/index.php/GNSS_signal
- [22] ANTCOM. (2008). *GPS Constellations for Avionics, Ground and Marine Applications*. Retrieved from https://www.geobchod.cz/resources/products_documents/1449181503_1112gpsantennas.pdf
- [23] Global System for Mobile Communications. (n.d.). Retrieved from <https://www.gsma.com/futurenetworks/faq/gsm/>
- [24] RF Wireless World. (n.d.). Retrieved from <http://www.rfwireless-world.com/Terminology/Cellular-network-vs-Ad-Hoc-network.html>
- [25] European Telecommunications Standards Institute. (n.d.). *Digital cellular telecommunications system; Specification of the Subscriber Identity Module - Mobile Equipment interface (GSM 11.11)*. Retrieved from https://www.etsi.org/deliver/etsi_gts/11/1111/05.03.00_60/gsmts_1111v050300p.pdf
- [26] From, G. P. S. (2010). Impact of next generation GNSS on Australasian geodetic infrastructure.
- [27] European Telecommunications Standards Institute. (n.d.). *Digital cellular telecommunications system; Radio transmission and reception*. Retrieved from https://www.etsi.org/deliver/etsi_gts/05/0505/05.00.00_60/gsmts_0505v050000p.pdf
- [28] Balanis, C. A. (2016). *Antenna theory: analysis and design*. John Wiley & Sons.
- [29] Shaw, J. A. (2013). Radiometry and the Friis transmission equation. *American journal of physics*, 81(1), 33-37.
- [30] XSENS. (2019, January 11). *MTi User Manual*. Retrieved from https://xsens.com/download/usermanual/ISM/MTi_User_Manual.pdf
- [31] U.S. Standard Atmosphere. (n.d.). Retrieved from https://www.engineeringtoolbox.com/standard-atmosphere-d_604.html
- [32] Dongre, V., & Mishra, A. (2016). Design of single band and dual band microstrip antennas for GSM, GPS and Bluetooth applications.

- [33] Jasim, S. E., Jusoh, M. A., Mazwir, M. H., & Mahmud, S. N. S. (2015). Finding the best feeding point location of patch antenna using HFSS. *ARPN Journal of Engineering and Applied Sciences*, 10(23), 17444-17449.
- [34] Altair Engineering. (2014, May). *FEKO Comprehensive Electromagnetic Solutions. User's Manual*. Retrieved from <http://altairuniversity.com/wp-content/uploads/2015/03/UserManual.pdf>
- [35] E-field Solutions. (2016, November 04). *Computational Electromagnetics Simulation*. Retrieved from <http://www.efieldsolutions.com/mompo.php>
- [36] Chang, C. W. (2003). Radiowave Propagation Modelling using the Uniform Theory of Diffraction. *School Eng., Univ. Auckland, Auckland, New Zealand, Tech. Rep.*
- [37] Pathak, P. H., Carluccio, G., & Albani, M. (2013). The uniform geometrical theory of diffraction and some of its applications. *IEEE Antennas and Propagation magazine*, 55(4), 41-69.
- [38] Arif, A. (2017, September 24). *Most Popular Commercial Airplanes That Airlines Buy*. Retrieved from <https://wonderfulengineering.com/top-10-commercial-airliners/>
- [39] The Boeing 737 Technical Site. (1999). Technical Specifications. Retrieved from <http://www.b737.org.uk/techspecsngs.htm>
- [40] COMSOL (n.d.). *Antenna Crosstalk on an Airplane's Fuselage*. Retrieved from <https://www.comsol.nl/model/antenna-crosstalk-on-an-airplane-s-fuselage-18087>